Integrating ultrafast all-optical switching with magnetic tunnel junctions

Integrating ultrafast all-optical switching with magnetic tunnel junctions

PROEFSCHRIFT

ter verkrijging van de graad van doctor aan de Technische Universiteit Eindhoven, op gezag van de rector magnificus prof.dr.ir. F.P.T. Baaijens, voor een commissie aangewezen door het College voor Promoties, in het openbaar te verdedigen op donderdag 07 april 2022 om 14.30 uur.

door

Luding WANG

geboren te Baotou, China

Dit proefschrift is goedgekeurd door de promotoren en de samenstelling van de promotiecommissie is als volgt:

voorzitter:	prof.dr.ir. G.M.W. Kroesen
1e promotor:	prof.dr. B. Koopmans
2e promotor:	prof.dr. W. Zhao (Beihang University)
copromotor:	dr.ir. R. Lavrijsen
leden:	prof.dr. A. Fiore
	prof.dr. C. Wang (Beihang University)
	prof.dr. E. Fullerton (UC San Diego)
	prof.dr. T. Nie (Beihang University)
adviseur:	dr. D. Ravelosona (Université Paris-Saclay)

Het onderzoek dat in dit proefschrift wordt beschreven is uitgevoerd in overeenstemming met de TU/e Gedragscode Wetenschapsbeoefening.

Integrating ultrafast all-optical switching with magnetic tunnel junctions

Luding WANG

A catalogue record is available from the Eindhoven University of Technology Library
ISBN: 978-90-386-5481-2

This work is part of the Gravitation program “Research Centre for Integrated Nanophotonics,” which is financed by the Netherlands Organisation for Scientific Research (NWO).

Contents

1

Introduction

In this introductory chapter, a brief motivation and technological relevance of this thesis is presented. The chapter starts with a general introduction to the context of this thesis, whereafter the mainstream memory technologies and the involved physics at the basic level are introduced. Next, an overview of spintronics and magnetic random-access memory (MRAM) is given, with the emphasis on the opportunities and challenges towards the next-generation universal memory. As the building block and the bit cell of the MRAM, magnetic tunnel junctions (MTJs), as well as the tunneling magnetoresistance (TMR) effect for MTJ reading, are introduced. Subsequently, several well-established mechanisms for MRAM writing are discussed, their fundamental limitations in terms of speed and efficiency are pointed out. To address such bottlenecks, this thesis explores a novel magnetization switching mechanism by using femtosecond laser pulses. Finally, the outline of the thesis is presented at the end of the chapter.

1.1 General introduction

In the era of Big Data and Internet of Things, memory technologies have laid the foundation of the electronic information industries. Over the last few decades, they have been developed rapidly as forecasted by Moore's law, i.e., the number of transistors in an integrated circuit (IC) chip doubles in every two years. The semiconductor industry was dedicating to make higher-performance (faster) and higher density (smaller) memory chips.

However, as the continuous downscaling of the technology node, the semiconductor devices meet an intrinsic performance bottleneck, which is due to the static leakage current. Consequently, their further development can't be sustained simply by shrinking the transistors' size, in other words, Moore's law is coming to an end.

To address such a "power wall" issue , spintronics, also known as spin-electronics[1,2], is a novel interdisciplinary field that received a lot of scientific interests involving condense matter physics, magnetics, and microelectronics. Compared to conventional semiconductor-based electronics only employ electron charge flow, spintronics manipulate both the electron charge and the electron spin degree of freedom to enable information processing, memory, and sensing.

As a specific example in this post-Moore era, spintronic *Magnetic Random-Access Memory (MRAM)* technology offers substantial potentials to revolutionize the mainstream computing architecture[3–6]. As a non-volatile memory (i.e., the information is retained after the power is turned off), it has been considered as the next-generation "universal" memory due to unique performances such as non-volatility, fast data access, indefinite endurance, and high scalability.

Over the past 25 years, two major generations of MRAMs have been proposed, classified by different operation schemes to write its bit cell. Specifically, the prototype MRAMs typically relied on external magnetic field, whereas state-of-the-art MRAMs are exploiting fully electrical switching schemes, which are based on injection of currents with a net alignment (polarization) of the electron spins. However, the physical processes underlying such a current-induced scheme set a

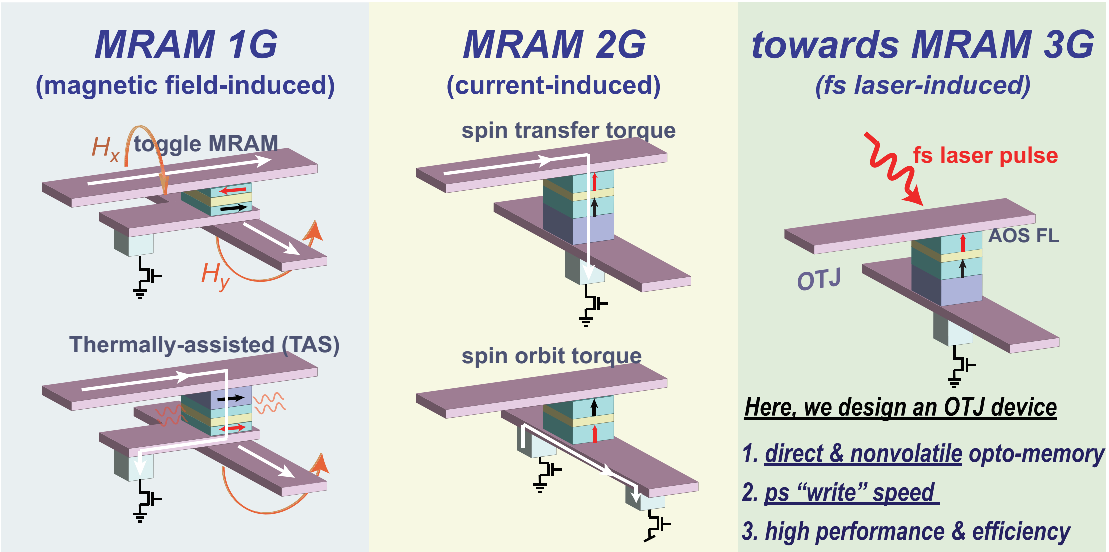

Figure 1.1: The development roadmap of the Magnetic Random-access Memory (MRAM) technology. "G" abbreviates for "Generation". Left: "MRAM 1G" based on magnetic field-induced switching. Center: "MRAM 2G" based on spin polarized current (Inspired by Dieny *et al.*[6]). Right: "MRAM 3G" proposed in this thesis. By using a spintronic-photonic combination, the device enables a picosecond all-optical operation with a high energy efficiency.

limit on the writing speed, typically not faster than a nanosecond.

As a result, the speed of MRAM is limited to a nanosecond time constraint, with high writing energy consumption. These issues have remained a long-existing vital challenge for the modern spintronic community. How to surpass the speed and energy bottleneck fundamentally?

Seemingly irrelevant, with the rapid development in the field of *Ultrafast Photonics*, the femtosecond (fs) laser has become the fastest stimuli commercially available. As a prominent bridging point with spintronics, in 1996, it was noticed that the interaction of a fs laser pulse with a spintronic material can cause a modification of the magnetic state at the sub-picosecond timescale[7], which is orders of magnitude faster than the spin-orbit interaction and the electron-phonon interaction.

An emerging concept has been recognized since 2007[8], i.e., employing a fs laser to operate a spintronic memory. At that year, it was demonstrated that, upon fs laser pulse excitation, the magnetization of certain ferrimagnetic materials (where the magnetic moment of the two sublattices alligns antiparallel) could be fully reversed at an unprecedented speed (tens of ps) with the least energy consumption[7]. This observation marked the birth of the field of *All-Optical Switching* (AOS) of magnetization, which is of significant technological relevance and fundamental interest.

Inspired by the ultrafast and least-dissipative AOS scheme, a world-record fastest and energy-efficient "hybrid" memory device, i.e., an "opto-MRAM" that is solely operated by a fs laser pulse, is conceptually envisioned as an alternative memory technology by the spintronic community. It is considered as a competitive route towards a new-generation spintronic memory design[7]. It has been predicted that such an "opto-MRAM" can be operated at a picosecond speed, which is $1-2$ orders of magnitude beyond state-of-the-art MRAMs, with an enhanced energy efficiency ($\approx$ 100 fJ to switch a 50×50 nm^2 sized memory bit[7]) as well.

The work presented in this thesis demonstrates the *design, fabrication, and characterization* of the basic building blocks of such an "opto-MRAM" *from a device-orientated perspective*, i.e., a fully functional "opto-MTJ". Key scientific objectives, regarding process compatibility, material exploration, and novel physical mechanisms, are addressed, as well as appealing technological performances as to speed and energy efficiency. They constitute the integral parts of this thesis. In the following, a more detailed introduction on the related technologies and background is given, followed by the outline of this thesis.

1.2 Memory technologies

Memory chips based on complementary metal–oxide–semiconductor (CMOS) technology have laid the foundation of the modern electronic information industries[9,10]. As a critical component of any electronic computers, memories are used to buffer the intermediate data during computing, as well as to store the mass amount of information. It dominates the performance of a computer architectural design regarding operation speed, areal density, and energy efficiency[11–13].

The memory market today is composed of a hierarchical structure using different technologies, where a trade-off among their speed, capacity, cost, and density is always required[14,15]. Specifically, Volatile Memory technologies, including Static and Dynamic Random-Access Memory (SRAM and DRAM), are employed as Cache and Main Memory. They enable high-speed data access to frequently-used data that is being executed in the CPU. SRAM and DRAM feature low areal densities at the trade off to high costs.

On the other hand, Non-Volatile Memories (NVMs)[16–18], such as Hard-Disk Drives (HDDs)[19] and Flash memory[20,21], have a higher density with low cost[22]. They are widely used as Auxiliary Memories to store massive and unfrequently-used data with a relatively slow (usually in µs) data access speed. Based on such a trade-off in a computer system, both high-speed and high-capacity data memory is achieved[14].

To introduce the readers with a general context of this thesis among the contemporary memory technologies, in the following, a brief discussion of the established memories is presented. It will become evident that the nonvolatile spintronic memory offers the best comprehensive performance, thus highly promising towards the next-generation "universal" memory paradigm.

1.2.1 Volatile memory technologies

Static random-access memory

SRAM is commonly used as the processor cache memory and internal registers of a CPU in computer systems, where the access speed is a top priority[23]. As a typical Volatile Memory, SRAM uses latching circuitry to store each bit. A typical SRAM cell is composed of 6 MOSFET transistors that form a flip-flop circuit. SRAM is a widely adopted solid-state memory due to its high access speed and energy efficiency, although the high cost and the large footprint remains relatively disadvantageous[17].

The SRAM technology meets a serious bottleneck as the CMOS technology node is scaling down[24,25]. Specifically, the static leakage current through the MOSFET would become highly problematic for smaller critical dimensions, resulting in a major source of power consumption for CMOS-based chips, as predicted by the International Technology of Roadmap for Semiconductors (ITRS)[26,27].

Dynamic random-access memory

DRAM is another main type of Volatile Memory, which has a simpler design compared with SRAM. The bit cell of DRAM is composed of single transistor and capacitor, where its writing/reading is achieved by charging/discharging the capacitor[23]. DRAM is widely used as the Main Memory in a computer, storing frequently-used data that is being executed in the CPU.

To prevent the slow leakage of the electric charges in the capacitors, DRAM relies on a refresh circuit to periodically recharge the capacitors every few milliseconds. This refreshing operation leads to detrimental additional energy consumption[17,28]. In addition, as a consequence of the continuous CMOS down-scaling[24], DRAM also meets a serious bottleneck on static power consumption[26], with a higher read-error rate due to the decreased capacitance as the capacitor in the DRAM scaling down.

Apart from the energy bottleneck, another significant bottleneck for both SRAM and DRAM is the growing interconnection latency between the processor and the off-chip memories. Such a speed gap is referred to as the “Von Neumann memory wall bottleneck”[29,30].

Non-volatile memory technologies

To address such bottlenecks, an effective solution is to adopt non-volatile memories as Caches and Main Memories. Such a “Universal Memory” holds a significant promise towards the non-Von Neumann paradigm[17,28,31]. Firstly, due to its non-volatility, a normally-off/instant-on computing operation is enabled. As a result, the static power consumption for data retention is completely eliminated. In the following, a short overview on the NVMs is presented.

Flash memory

Among various NVMs, Flash memory is a commercialised and matured technology that is widely used for massive data storage[17,20,21]. It features a high areal density and a low cost. A basic Flash memory cell is composed of floating-gate MOSFETs. The floating gate is insulated from the transistor by a tunnel oxide layer. A NOR Flash addresses individual bit cells in parallel, whereas a NAND Flash strings together the floating gate transistor to enable addressing in series[23].

During data writing, electrons are charged to the floating gate, which would degrade the oxide layer surrounding the floating gate. As a result, the endurance of a Flash Memory is highly limited ($\sim 10^5$ read/write cycles). Furthermore, the access speed of Flash memory (typically in ms) is several orders of magnitude slower than that in DRAM and SRAM. Constrained by these drawbacks, the Flash memory fails to meet the performance requirement as the cache or the main memory[4].

Emerging NVMs

With a "Universal Memory" in prospect, emerging NVM technologies have become a topical field of Research and Development ($R\&D$)[17,28]. These technologies include Resistive Random-Access Memory (RRAM)[32,33], Phase Change Memory (PCM)[34], and Magnetic Random-Access Memory (MRAM)[3–5,35]. A comparison of key performance metrics in these NVMs is summarized in Table 1.1[5].

Table 1.1: A comparison of key metrics in various Non-volatile Memories including NOR Flash, NAND Flash, RRAM, PCM, and MRAM. "End." abbreviates for "Endurance", i.e., write cycles before the device breakdown. "R/W" denotes "read/write" access time. Ref. from Kent and Worledge[5]

Metrics	End. (cycles)	R/W (ns)	Density	Other
NOR Flash	10^5	100 / 10^3	medium	High write energy
NAND Flash	10^5	100 / 10^6	high	High write energy
RRAM	10^9	1 – 100	high	complex mechanisms
PCM	10^9	10/100	high	Operating $T < 125°$C
MRAM	∞	2 – 30	medium	Low read signal

Among these emerging NVMs, the MRAM technology offers a best trade-off performance, including a fast data "read/write" speed, a low power consumption, and a high scalability. More importantly, the endurance of MRAM is considered as indefinite in the industry ($> 10^{15}$ cycles) since no degradation mechanisms (as such in the Flash Memory) or mechanical moving parts (as such in the HDDs) are used.

As a result, the MRAM is highlighted toward the forementioned "universal memory" paradigm, promising for a nonvolatile memory architectures at all hierarchy levels[36,37]. In the following, a brief overview on Spintronics and the MRAM technology is provided.

1.3 Spintronics and magnetic random-access memory

As discussed in Section 1.1, spintronics manipulate both the charge and the spin degree of freedom of electron to enable information processing, memory. As a complementary technology, spintronics-based MRAMs offer unique advantages including nonvolatility, scalability, high speed, and low power consumption. These features make it highly competitive in the post-Moore era.

1.3.1 Spintronics

Spintronics is originated from the discovery of the giant magnetoresistance effect (GMR)[38,39] in 1988 by Albert Fert and Peter Grünberg, who both received the Nobel Prize in Physics in 2007[40]. GMR exists in a sandwiched nanostructure where two ferromagnetic (FM) layers are separated by a thin metal spacer, which is referred to as a spin valve (SV)[38,39]. A significant bi-stable resistance state is observed, depending on the relative magnetization orientation of the two FM layers. Such a effect is originated form spin-dependent electron scattering[38].

As to practical applications, the SVs were first used as magnetic-field sensors (read heads) in HDD drives[41]. This invention led to a significant enhancement of the HDD's storage density by several orders of magnitude, which gained successful commercialization soon after its invention by IBM[42], boosting the information industry. Spintronic devices are also heavily used as a magnetic field sensor in automobile industries and biomedical devices[43,44].

Since 1995, spintronic-based MRAM devices have received significant research effort in academia and industry due to its prosperous application scenarios. Leading integrated circuit companies have launched ambitious MRAM development programs, aiming at the key enabling technology for the next-generation memory paradigm[6]. In the following, we will stress this aspect in detail.

1.3.2 Magnetic random-access memory

As discussed before, the key advantages of MRAM include nonvolatility, high access speed, low power consumption, high scalability, indefinite endurance, as well as easy integration with CMOS technology[3–5].

The state-of-the-art MRAM is promising to replace the embedded SRAM (L3/L-4) cache or the embedded FLASH (eFLASH), making it an ideal candidate for the next-generation NVMs[6,45]. Compared to SRAM/DRAM, no static power is required to retain the data. In addition, down-scaling of MRAM below 20 nm has been demonstrated. Compared to FLASH, it shows high "read/write" speed and indefinite endurance.

MRAM is also promising for solving the "Von Neumann memory wall" issue. Since the MRAM is compatible with the CMOS Back-of-End-Line (BOEL) process[27,46], a hybrid MRAM/CMOS IC design would reduce the distance between memory and processor, thus contracting the interconnection latency effectively.

Significant progress in MRAM *R&D* has been achieved by leading semiconductor companies. For example, Intel has realized 300-mm wafer-scale embedded MRAM integration with the 22 nm CMOS technology, whereas Samsung and Everspin have released a 1 GB embedded MRAM on the 22 nm technology node[6,45]. In the following, we will discuss the MRAM bit cell, with an emphasis on its structure and three basic memory functionalities, i.e., data reading, retention, and writing.

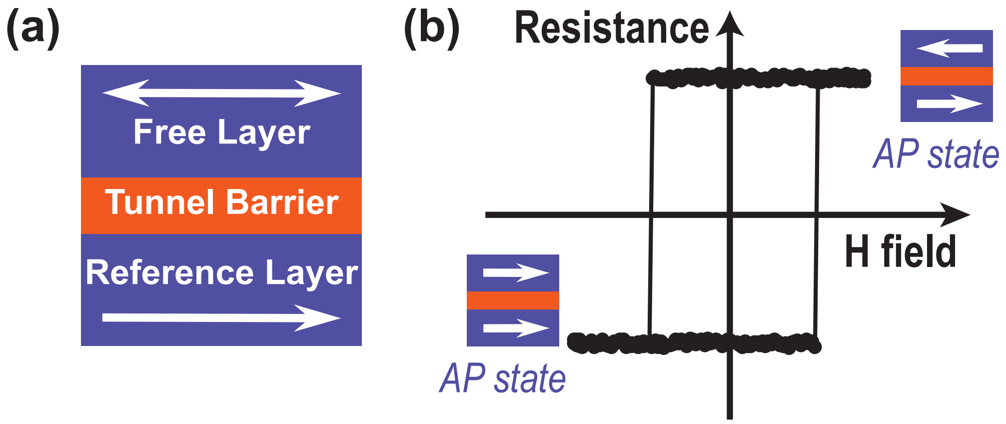

Figure 1.2: A schematic illustration of the magnetic tunnel junction (MTJ). (a) Typical structure of an MTJ. It is composed of two FM layers that are separated by an insulating tunnel barrier. The magnetization direction of the bottom FM layer is fixed, whereas the magnetization of the top FM layer is bi-directional. (b) Typical tunnel magnetoresistance effect of an MTJ. A bi-stable resistance state is dependent on the relative magnetization configuration of the two FM layers.

1.4 MRAM building blocks

As the basic bit cell of an MRAM, the magnetic tunnel junction (MTJ)[47] is also composed of two FM layers that is similar to a SV. Nevertheless, it is separated by an insulating tunnel barrier (typically MgO[48] or Al_2O_3[49]) with a thickness typically $1-2$ nanometers.

1.4.1 Magnetic tunnel junctions

As shown in Fig. 1.2, the magnetoresistance of the MTJ depends on the relative magnetization orientation (R_P: parallel; R_{AP}: antiparallel) of the two FM layers[47,50]. Specifically, the magnetization direction in one of the FM layers ("pinned layer") is fixed along its easy axis using a special design, whereas the other ("free layer (FL)") is bi-directional, leading to a bi-stable magnetoresistance state. This effect is termed as the tunneling magnetoresistance (TMR) effect[51], with the TMR ratio defined as:

$$\mathrm{TMR} = \Delta R/R = (R_{AP} - R_P)/R_P \tag{1.1}$$

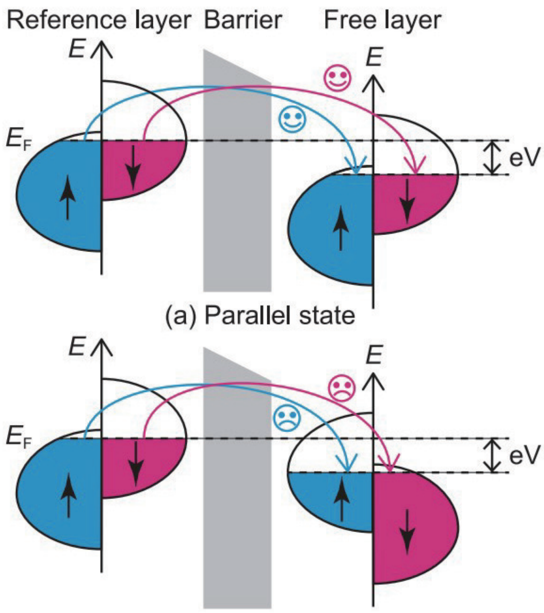

Figure 1.3: TMR effect explained by spin-dependent electron tunneling rates. Illustration of DOS in the FL and the RL in (a) parallel and (b) antiparallel configuration. The vertical axis shows the energy level. The horizontal axis shows the number of electron states. DOS of the FM layers is separated into a majority and a minority energy band around the Fermi level, leading to a spin polarization (P). Electron tunneling probability is determined by the relative magnetization direction of the FL and the RL[52].

Such bi-stable states can be used to represent the binary data "0"/"1" respectively[42,47], which can be read-out by measuring the MTJ's resistance electrically. The TMR effect was first observed by Julliere[51] at low temperature, since then, research activities have focused on enhancing TMR ratio by material exploration.

TMR effect is a result of the different spin-dependent electron tunneling rates[53,54], which can be explained by the spin-dependent tunneling theory. Fig. 1.3 shows a simplified illustration of the density of states (DOS) with FL and RL in parallel (a) and antiparallel (b) configuration. In this diagram, the vertical axis indicates the energy level, and the horizontal axis indicates the number of electron states.

As in a ferromagnet, the DOS is divided into a spin-up and a spin-down energy band due to the exchange interaction (since it favours a parallel alignment).

As a result, electrons are occupied in a majority state and a minority state around the Fermi level, leading to a spin polarization (P) defined as,

$$P = \frac{|n_{\uparrow} - n_{\downarrow}|}{n_{\uparrow} + n_{\downarrow}} \tag{1.2}$$

where $n_{\uparrow}$ and $n_{\downarrow}$ denote the number of electrons at the Fermi level for each band, respectively.

As represented by the blue and red arrows, the probability of electron tunneling is determined by the n of a same spin-dependent energy band[3,50]. In other words, the tunneling current conductivity is dependent on the relative magnetization direction of the FL and the RL. Thus, TMR is highly relevant to spin polarization, which can be theoretically calculated by using Julliere's model[51],

$$\mathrm{TMR} = \frac{2P_1P2}{(1 - P_1P_2)} \tag{1.3}$$

where P_1 and P_2 denote the spin polarization of the FL and the RL, respectively.

With the development of the nanofabrication technique (specifically, thin-film deposition) around 2002, engineered MTJs employing CoFe electrodes and amorphous Al_2O_3 barriers achieved a TMR ratio up to $\approx 70\%$ at room temperature[54,55]. Theoretical considerations showed that a significantly higher TMR could be expected by using a single-crystalline MgO tunnel barrier, which was attributed to the high tunnel current polarization due to the lattice symmetry of the MgO crystal[56,57]. Such a prediction was confirmed experimentally in 2004, leading to a TMR up to 300% and an effective P of $\approx$85%[48,58]. The CoFeB/MgO-based MTJ thus became the mainstream design for MRAM applications[42,47], which is used in this thesis to ensure a relatively high TMR.

As to data retention, the energy barrier (E_b) of the bi-stable states is established by the magnetic anisotropy, resulting in a preferential easy axis of the magnetization direction. For early types of MTJs, an in-plane magnetic anisotropy (IMA)[5,59,60] is established by using an elliptical bit shape, where the preferential magnetization direction is set along the long axis of the bit. The stability of the memory bit is evaluated by the ratio between the E_b and the thermal energy[61], which is termed as the thermal stability factor (Δ),

$$\Delta = E_{\mathrm{b}}/k_{\mathrm{B}}T = KV/k_{\mathrm{B}}T \tag{1.4}$$

where K is the anisotropy energy density, V is the volume of the FL, k_{B} is the Boltzmann's constant and T is the ambient temperature. As to a practical MRAM bit for a 10-year retention, a $\Delta > 60$ is always required[35,62]. However, as inferred from Eq. (1.4), upon MTJ scaling down (i.e., decreasing V), an enhanced magnetic anisotropy K is required to maintain the Δ. Since in the IMA-MTJ bits, K is determined by the shape anisotropy, which is directly related to and limited by M_s, it thus can be estimated that the shape anisotropy of the in-plane MTJ is insufficient to stabilize the bit smaller than 40 nm, thus limiting the scalability of the MRAM chips.

To address these issues, interfacial perpendicular magnetic anisotropy (PMA) was introduced at the ferromagnet/oxide interface[63,64], where the out-of-plane easy axis originates from the 3d/2p electronic hybridization at the interface[65]. Soon, the interfacial PMA at the CoFeB/MgO system was utilized to build perpendicularly magnetized MTJs[66]. Since PMA originates from the interface, and thus immune to the bit shape/size, a better Δ at the nanoscale is expected[67], with a full scalability below 20 nm as well[68]. On the one hand, it keeps a high "write" efficiency, on the other hand, it keeps a high TMR ratio. As a result, PMA-based CoFeB/MgO system has become a paradigm in the state-of-the-art MRAM design[47,66]. In the following, we will discuss how to write information to an MRAM, in other words, the FL's magnetization switching schemes.

1.4.2 MRAM writing dynamics

As discussed before, the TMR of an MRAM bit cell is determined by the resistance change when reversing the relative orientation of the two ferromagnetic layers. Thus, the writing operation consists of switching the FL's magnetization. Over

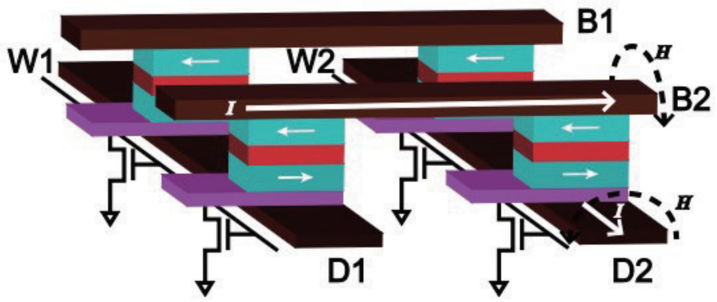

Figure 1.4: First generation of MRAM: magnetic field-induced switching. Two addressing lines are cross-arranged, which are used to generate the magnetic field pulses by electrical currents. The magnetic field pulses jointly switch the MTJ bit at the intersection of the addressing lines[52].

the last 25 years, two major generation MRAM writing mechanisms have been proposed and implemented.

Specifically, the first generation of MRAMs relied on applied magnetic field. As in the Stoner-Wolfarth type of MRAM[69,70] shown in Fig. 1.4, the MTJ bit cell was positioned at the cross point of two addressing lines. The magnetic field pulses were generated by electrical currents through the lines, jointly switching the MTJ bit at the crossing point of two wires. To address the accidental write-errors caused by the "Half-selectivity disturbance", the "toggle MRAM" was developed by applying a 4-step sequence of magnetic field[71,72], which was commercialized by Everspin in 2006.

To reduce the extensive current density, thermally assisted switching of MRAM (TAS-MRAM) was proposed[73,74], which exploited Joule heating to temporarily heat the storage layer, and reduce its coercivity. Apart from the Joule dissipation to the ambient, the intrinsic scalability issue remained unsolved[75]. Since the switching field is inversely proportional to the MTJ size, down-scaling below 90 nm technology node was not possible[47].

To further alleviate these drawbacks, the second generation of MRAM employed spin polarized current, where the spin orientation of the electrons are highly polarized. This can be generated easily by injecting an electrical current through a magnetic layer. In 1996, Slonczewski[76] and Berger[77] predicted that such a spin

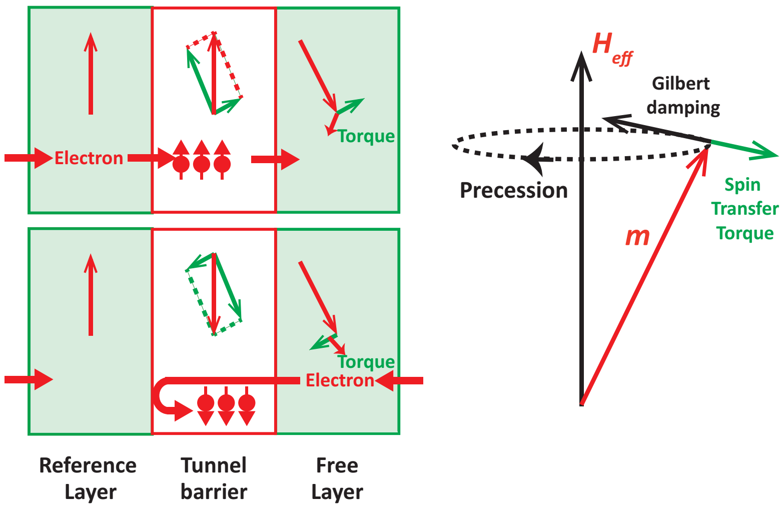

Figure 1.5: Spin transfer torque (STT) induced MTJ switching (second generation of MRAM)[52]. (a) Spin polarized current and STT induced MTJ switching. The injected current transmits through the RL and gets spin-polarized, whereafter it switches the magnetization of the FL. (b) Schematic illustration of the magnetization dynamics induced by STT.

polarized current would transfer the angular moment it carries to a ferromagnetic film the current is injected into, and exert a torque on the magnetization, which is termed as the "spin-transfer torque (STT)".

In 2004, the STT effect was demonstrated to switch an MTJ[78]. This soon led to an entirely new kind of MRAM, namely, STT-MRAM. Research activities on STT-MRAMs have been launched worldwide as a topical research field, due to the all-electrical approach[6,35,79] and the full scalability. Now, STT has become a mainstream "write" scheme of MRAM. A commercialized 64 Mbit STT-MRAM has been released to market by Everspin[80] in 2013.

In the demonstrated process as shown in Fig. 1.5 (a), upon an electrical current injected into the reference layer, it will get spin polarized along its direction. After it tunnels through the barrier, the spin transfer torque is exerted on the free layer's magnetization[81,82].

According to the macrospin approximation, the magnetization dynamics of the FL induced by electrical current is described by the Landau-Lifshitz-Gilbert (LLG) equation:

$$\frac{\partial \boldsymbol{m}}{\partial t} = -\gamma\mu_0 \boldsymbol{m} \times \boldsymbol{H}_{\mathbf{eff}} + \alpha \boldsymbol{m} \times \frac{\partial \boldsymbol{m}}{\partial t} - \frac{\gamma\hbar J P}{2 e t_F M_s} \boldsymbol{m} \times (\boldsymbol{m} \times \boldsymbol{m}_{ref}) \tag{1.5}$$

where $\boldsymbol{m} = \boldsymbol{M}/M_s$ is the normalized FL magnetization, $\boldsymbol{H}_{\mathbf{eff}}$ is the effective field, γ is the gyromagnetic ratio, μ_0 is the vacuum permeability, α is the Gilbert damping coefficient, $\hbar$ is the reduced Planck constant. J is the writing current density, P is the spin polarization ratio, e is the charge of the electron, t_F is the thickness of the FL, and M_s is the saturation magnetization of the FL.

On the right side of Eq. (1.5), the three terms represent the following processes, as described in Fig. 1.5 (b). The first term represents the torque caused by the effective magnetic field, resulting in precession around $\boldsymbol{H}_{\mathbf{eff}}$. The second term is the torque by Gilbert damping, i.e., a phenomenological term that describes the energy dissipation from the system, leading to $\boldsymbol{m}$ aligning to $\boldsymbol{H}_{\mathbf{eff}}$ gradually. The third term represents the spin transfer torque (τ_{STT}).

Notably, the initialization of STT requires a random thermal fluctuation to spur such a colinear alignment, since τ_{STT} is zero during the start-up of the STT event ($\boldsymbol{m}$ is colinear with $\boldsymbol{m}_{ref}$ in a bi-stable state). This incubation delay process typically takes several nanoseconds[83,84]to finish data access.

Moreover, another major source of the speed constraint is due to the spin precession process. As shown in Fig. 1.5, the $\boldsymbol{m}$ of the FL precesses about an effective field $\boldsymbol{H}_{\mathbf{eff}}$, with a precession frequency (termed as Lamour frequency)

$$f = \frac{\gamma}{2\pi} B \tag{1.6}$$

For ferromagnetic metals such as cobalt, a typical value of γ is 10 MHz/T, resulting in a 100 ps spin precession time. To enable magnetization switching, the duration of the stimuli must be applied longer than one-quarter of the precession period, since it is required to overcome the potential barrier. All these fundamental limitations constrain the speed and efficiency of MRAM technologies, addressing of

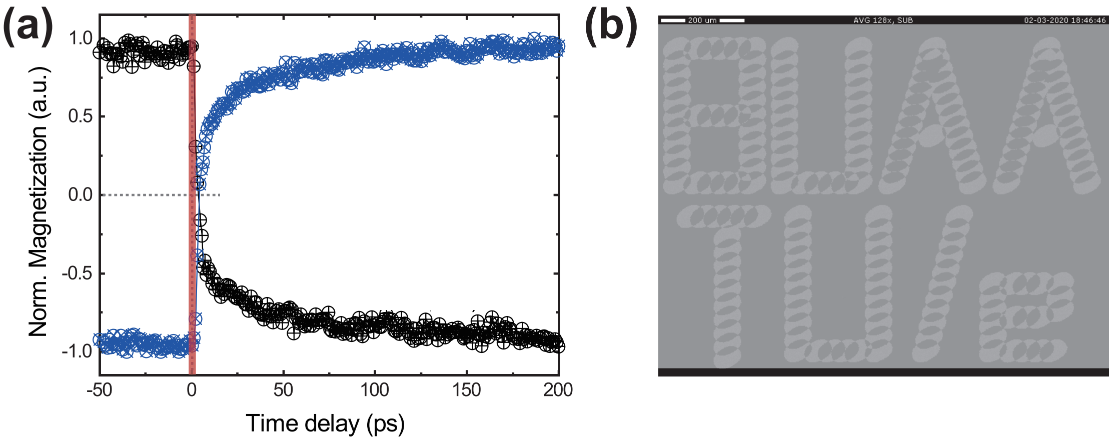

Figure 1.6: (a) A typical result of femtosecond-resolved AOS dynamics performed on the "opto-MTJ" full-sheet stack, which is used as a general preview. The horizontal axis is the time delay after the fs laser excitation (indicated by the red line), and the vertical axis is the normalized magnetization dynamics measured in real time. It convincingly shows that the magnetization switching takes place within a 20 ps time scale. (b) A logo of Beihang University (BUAA) and Eindhoven University of Technology (TU/e). This PhD project is jointly coordinated by the BUAA and the TU/e. The image is measured by Kerr microscopy on the proposed device upon subsequent fs laser pulse.

which has remained a long-existing challenge for the spintronic industry.

1.5 Challenges and innovation

To tackle the challenge formulated in the previous section, a conceptually new approach to manipulate the magnetic state at an unprecedent time scale is needed. Investigating the magnetization dynamics on a non-equilibrium thermodynamic regime seems to become the key to find the answer.

A promising technological route is termed as the fs laser-induced single-pulse All-Optical Switching (AOS) of magnetization[7,8], which was experimentally demonstrated in 2007. In AOS, a fs laser pulse brings the material system into a strongly non-equilibrium state, and switches its magnetization at an unprecedented speed and low dissipation, which will be discussed in Chapter 2 in detail. Here, as a preview, a typical result of fs time-resolved magnetization dynamics is shown in Fig. 1.6 (a), clearly revealing the switching indeed takes place within a 20 ps time scale (The details of the measurement technique as well as the results will be explained in Chapter 6).

Inspired by the material-orientated progress in the field of AOS, the emerging potential of integrating AOS with spintronic MRAMs *at a device level* has been recognized. By developing such a novel "hybrid" memory that operates beyond the equilibrium thermodynamics, a fast (< 20 ps) and low-dissipative (< 1 pJ/bit) "opto-MRAM" is conceptually envisioned as a competitive route towards the new-generation MRAM design.

This thesis thus formulates the research question, if one can realize a fully-functional picosecond spintronic MRAM solely operated by a fs laser pulse. This thesis will give an answer to this question *from a device-orientated perspective*, where the scientific field of spintronics and ultrafast photonics (more specifically, fs lasers) synergize. The key highlight of this thesis is to demonstrate a picosecond opto-spintronic memory device with an all-photonic operation, non-volatility, and high energy efficiency.

As a symbolic representation of this work, a logo with the abbreviation of Beihang University (BUAA) and Eindhoven University of Technology (TU/e) is shown in Fig. 1.6 (b), which jointly coordinate this PhD project. The image, aiming to show AOS in it simplest form, is measured by a technique called Kerr microscopy, where the light/dark contrast indicates the "up"/"down" magnetization direction, respectively. It depicts the magnetization of a magnetic thin film after AOS of targeted areas, which is done by exposing the sample to consecutive fs laser pulses in the desired pattern (all relevant concepts and methodologies will be discussed throughout this thesis). A more detailed background and literature review of the related field is presented in the next chapter.

1.6 This thesis

In this thesis, we demonstrate the design, fabrication, and characterization of a fully-functional picosecond "opto-MTJ" *at a device level*, as a first step of spintronic-photonic integration. The research background of this thesis is presented in Chapter 2, with a literature review on the related fields. Next, the experimental methodology on thin-film deposition, MTJ fabrication, as well as various characterization techniques, is described in Chapter 3.

In Chapter 4, post-annealing process compatibility of single-pulse AOS in synthetic ferrimagnetic Pt/Co/Gd stacks are experimentally explored. Remarkably, we found that the efficiency of AOS is enhanced upon post-annealing up to 300°C, which is required for MTJ fabrication. Meanwhile, the velocity of domain wall motion, i.e., magnetic domains driven trough the material by applying a magnetic field, is also increased. These results reveal that such a material system is highly ideal for further spintronic device integration.

In Chapter 5, fs laser-induced heat-assisted magnetic recording (HAMR) in a high-performance p-MTJ storage device is experimentally investigated. Although the HAMR technique has been widely used in ultra-high-density HDDs, data "read" operation is achieved by a mechanical "read head", limiting its robustness and speed. To address this issue, a high-performance HAMR-p-MTJ storage device is demonstrated, with a direct electrical readout. These results also represent a first step towards an all-optically switchable MTJ device.

In Chapter 6, which is the major output and a climax of thesis, a fully-functional "opto-MTJ" is developed and explored. The first part of Chapter 6 describes the exploration on a suitable FL material system, aiming at a single-pulse AOS and a considerable TMR ratio simultaneously. By detailed measurements, a composite structure that incorporates a Co/Gd bilayer coupled to a CoFeB/MgO system, well meets the design requirement.

In the second part of Chapter 6, such an integrated memory device is fabricated and characterized. The results show a deterministic and efficient all-optical "write" operation, as well as an electrical TMR read-out. The speed of the device is systematically characterized by fs time-resolved measurements, representing an important milestone towards a new category of picosecond spintronic memory by using photonic integration.

Chapter 7 provides a summary of the thesis, as well as a general outlook of the integrated spintronic-photonic memory technology at a higher circuit level.

2

Background

The scientific objective of this thesis is to develop and explore a picosecond AOS-MTJ memory device, by integrating ultrafast photonics with spintronics. In this chapter, the research background and possible routes towards this ultimate goal are discussed. The chapter starts with a material-orientated literature review on the emerging field of AOS, including the basic concepts and terminology, the host material systems, and the underlying physics of AOS at a basic level. Afterwards, first demonstrations on the integrated device concepts are introduced. Further optimization routes aiming for a fully functional, high performance device are discussed, with an emphasis on the novel synthetic ferrimagnetic multilayer system.

2.1 All-optical switching

All-optical switching (AOS) describes the magnetization switching induced by laser-pulse excitation only, i.e., without magnetic field assistance or other stimuli. In this section, a literature overview of AOS from a material-orientated perspective is presented, which is started from a general review. The AOS effect was discovered rather unexpectedly in ferrimagnetic GdFeCo alloys in 2007[8], and was later shown to be an all-optical helicity-independent switching (AO-HIS) process. The AO-HIS in such alloys was induced by a single fs laser pulse, where the helicity dependence was shown to originate from the magnetic circular dichroism (MCD) effect. Latter, all-optical helicity-dependent switching (AO-HDS) was observed in engineered ferrimagnetic systems, as well as in ferromagnetic systems that are heavily used in spintronic memory technologies. However, the AO-HDS was demonstrated to be induced by multiple (≈100) laser pulse, limiting its technological potential for spintronic integration.

Although the underlying physics is still under debate, AO-HIS has been demonstrated to offer picosecond speed, which is 1 – 2 orders of magnitude faster than conventional switching schemes. Moreover, it shows high energy efficiency as well. AO-HIS consumes only 100 fJ for writing a 50×50 nm^2 sized memory bit, making it competitive with STT-MRAM (450 pJ—100 fJ)[85]. Consequently, the emerging potential towards employing AOS for ultrafast and energy-efficient memory applications was soon recognized. Stimulated by the high application potential, as well as the intriguing fundamental physics, the emerging field of AOS has been developed rapidly in the last 15 years.

2.1.1 Single-pulse AO-HIS in ferrimagnetic alloys

As mentioned above, ultrafast AOS was first observed in amorphous ferrimagnetic GdFeCo alloys in 2007[8]. As a rare earth–transition metal (RE–TM) material, the Gd sublattice and the Fe sublattice are antiferromagnetically coupled, leading to a net magnetization at room temperature. It was first demonstrated by Stanciu *et al.*[8] from the Radboud University in Nijmegen. They observed that, by using a circularly polarized single-40-fs laser pulse, the magnetization of a 20-nm-thick

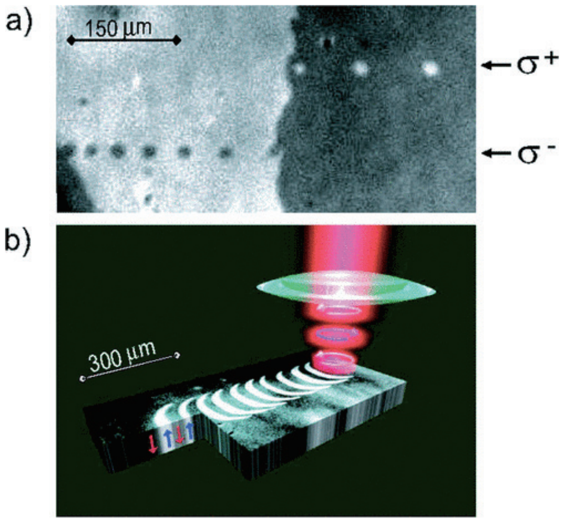

Figure 2.1: (a) Single-pulse helicity-dependent AOS in the GdFeCo alloys by circularly polarized fs laser pulses. The laser beam was swept across the sample surface, so that each pulse landed at a different position. The responses of AOS were measured by the Kerr microscopy. (b) Illustration of an ultrafast all-optical recording of magnetic bits. The optically written bits were overlapped at a small distance due to the laser beam sweeping at a relatively high speed. Meanwhile, the polarization of the beam was modulated between (σ^+) and (σ^-)simultaneously. Adapted from Stanciu *et al.*[8]

GdFeCo thin film could be switched in a reproducible manner.

Fig. 2.1 (a) shows the all-optically written domains as measured by Kerr microscopy, where the light/dark grey areas correspond to the domains with "down"-/"up" magnetization, respectively. A laser beam with left (σ^+) or right (σ^-) helicity was swept across the sample surface at a relatively low speed, so that each pulse exposed a different spot. The experiments unambiguously showed that the σ^+ pulse switched the magnetization in the magnetization "up" state, but it didn't affect the magnetization of the magnetization "down" state. In other words, single-pulse AOS can be achieved in GdFeCo alloys without the aid of an external magnetic field, and displays a helicity dependence. The small size variation of the written domains was caused by the pulse-to-pulse fluctuation of the laser intensity.

This purely laser-induced magnetization reversal was previously believed impossible. As a first explanation, this phenomenon was conjectured by a combined effect. Firstly, the fs laser heats the electron bath in the magnetic system just below the Curie point (T_C). Secondly, the circularly polarized laser simultaneously acts as an effective magnetic field due to the inverse Faraday effect[86,87], resulting in helicity dependence of the AOS process[8].

This finding revealed an ultrafast and efficient pathway for magnetic recording at a record-breaking speed. A simple illustration is illustrated in Fig. 2.1 (b). The figure was achieved by sweeping the laser beam across the sample surface, where optically written bits are overlapped at a small distance. Meanwhile, by simultaneously modulating the beam polarization, an ultrafast all-optical data writing is thus achieved.

The underlying physics of the AOS phenomenon was under significant debate, with concerns arising on such a two-fold explanation[88–91]. Indeed, by macrospin and atomistic models[88,89,91], the AOS process was reproduced. However, the required amplitude of the effective opto-magnetic field was extremely large (> 20 T), whereas its duration had to be chosen to be much longer than the 40-fs laser pulse used in the experiments. Moreover, in the first attempts of modelling AOS in a ferrimagnet, the individual switching dynamics of the Gd and the Fe sublattices wasn't taken into consideration[92,93], which were assumed to be the same due to the strong exchange interaction.

To address this issue, time-resolved element-specific X-ray magnetic circular dichroism (XMCD) measurements were performed[94], using a GdFeCo thin film upon fs laser excitation, as shown in Fig. 2.2. The XMCD signal provided insight into the time-resolved dynamics of the Fe and Gd sublattice magnetization separately (denoted as M_{Fe} and M_{Gd}, respectively). The result showed a typical three-phase characteristics. Firstly, rapid demagnetization of the two sublattices was observed, where Fe demagnetizes much faster. While M_{Fe} reached zero within 300 fs, the Gd was still demagnetizing up to 1500 fs. Note that, despite the strong exchange interaction between the two sublattices, the two sublattices demagnetize at distinctly different speeds.

Secondly, the M_{Fe} switched across the zero point, and rebuilt up along the reversed direction (i.e., along the M_{Gd}). This was assigned to the transfer of angular mo-

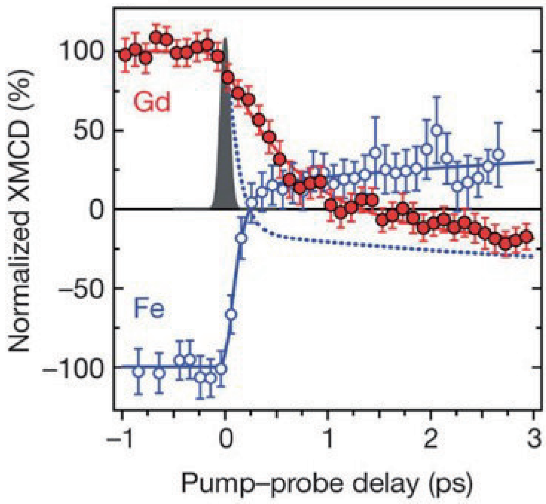

Figure 2.2: Time-resolved element-specific X-ray magnetic circular dichroism (XMCD) measurements of a GdFeCo thin film after laser-pulse excitation, which resolved the evolution of M_{Fe} and M_{Gd}. See text for details. Adapted from Radu *et al.*[94]

mentum due to the exchange scattering. Remarkably, a transient ferromagnetic-like state in the ferrimagnet was established. In other words, despite the antiferromagnetic coupled sublattices, the M_{Fe} and the M_{Gd} were aligned in the same direction within this timescale. Lastly, due to the antiferromagnetic coupling, the M_{Gd} was driven to switch, and after cooling down, a new thermal equilibrium in the reversed orientation was established.

This discovery provided new insights into the physics of ultrafast magnetism, as well as the emerging potential towards the opto-magnetic recording with an ultimate speed. Various theoretical models were developed to address the multi-sublattice behaviour[94–96], including the microscopic three temperature model - (M3TM)[97]. All of them reproduced a robust AOS toggle process in line with the three-step process.

Until the discovery of the all-optical toggle mechanism, it was generally believed that magnetization switching should be driven by a time-non-invariant vector as a stimulus, such as a magnetic field or a spin-polarized current (as in MRAM technologies discussed in Chapter 1). Heating, as a scalar, would not drive, but could only assist the magnetization switching, as already heavily used in the heat-

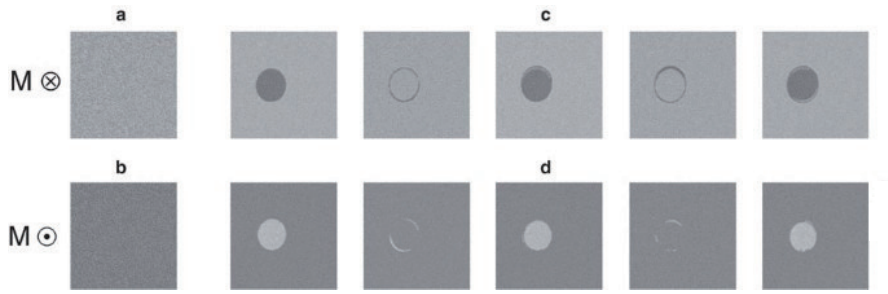

Figure 2.3: Single-pulse AOS measurement results of a GdFeCo film exposed by consecutive linearly polarized fs laser pulses, proving a purely thermal process. (a – b) Magnetization saturated in "up" and "down" direction, respectively. (c – d) Every odd number of laser pulses leads to a homogeneous optically written domain, whereas for every even number of pulses, the magnetization toggles back to original state. Adapted from Ostler *et al.*[98]

assisted magnetic recording (HAMR) technologies[19]. The discovery of AOS clearly disproved this necessity. A very elegant confirmation of the toggle scenario was reported by Ostler *et al.*[98] from the University of York. They demonstrated an AO-HIS of a GdFeCo by using a single linearly polarized laser pulse, without the presence of any magnetic field.

Fig. 2.3 shows the Kerr images of the GdFeCo film exposed to subsequent 100-fs laser pulses. Fig. 2.3 (a) and (b) are the initial saturated magnetization states with "up" and "down" directions. As shown in Fig. 2.3 (c) and (d), for every odd number of laser pulses, a homogeneous optically written domain was observed. For every even number of pulses, no net magnetization reversal was observed. This observation proved the single-pulse AO-HIS is a purely thermal process, which agrees well with results by atomistic simulations[95,96,99].

After have demonstrating that the ultrafast heating could act as a sufficient stimulus for AOS, the physical origin of the helicity dependence in the original studies wasn't clarified yet. To address this issue, it was soon found that AOS of GdFeCo exhibits a threshold fluence that is absorbed in the magnetic layer. This threshold fluence is independent of the laser helicity. Previous observations of helicity dependence were shown to be the result of the MCD effect[100,101], which describes the differential absorption of the σ^- and σ^+ circularly polarized light in a magnetic material. The MCD effect thus results in a helicity dependent AOS fluence window, which agrees well with all the experimental data on AOS.

Finally, having resolved that AOS is a purely thermal process, it opened the opportunities to use the very same mechanism in other approaches that don't (fully) rely on heating by a fs laser. Indeed, more recently, AO-HIS of GdFeCo has also been realized by hot-electron pulses (generated by laser heating) [102], as well as by picosecond current pulses (using a photoconductive switch) [103].

In conclusion, single-pulse AO-HIS has been found to be a robust process, with an appealing application potential. The speed of AOS is within several tens of ps, which is 1 – 2 orders of magnitude faster than conventional MRAM operation schemes [8,89,94]. Moreover, the AO-HIS is highly energy efficient [104]; it consumes only 100 fJ to switch a 50×50 nm^2 sized memory bit [7], making it even competitive compared to STT-MRAM (450 – 100 fJ) [35].

To realize scalable and high-density memory applications, pioneering efforts were initiated, including AOS in patterned microstructures [105], and laser-induced subwavelength domain patterns [106]. It turned out that the thermal stability of GdFeCo would be lost after downscaling below 200 nm due to its weak PMA, which is unfavourable for high-density recording.

It was considered very relevant that single-pulse AOS was demonstrated for highly anisotropic TbFeCo [107]. In this material, thermally stable domains down to 40 nm were written using plasmonic antennas [108], compatible with the current CMOS fabrication technology. Unfortunately, its practical applications were hindered by the extremely large H_c (up to 10 T), requiring a specifically designed magnet to saturate its initial state [109].

In summary, single-pulse AO-HIS in the GdFeCo is only suitable for a proof-of-concept spintronic integration. For that reason, research activities on exploration and synthesis of other AOS materials, aiming at general design rules, have gained considerable attention.

2.1.2 Development of the AOS material systems

The observation of AOS has been fuelling expectations for exciting technological applications. Towards this aim, the first research objective is to expand the range of material systems that facilitate the AOS phenomenon.

Engineered materials for AO-HDS

To address this issue, three empirical rules to design a material system that host AOS have been derived[110]. Firstly, the material system should contain two magnetic sublattices (or layers). Secondly, the two magnetic sublattices are coupled by an antiferromagnetic exchange interaction. Thirdly, different temperature dependencies of the magnetization of the two sublattices (or layers) are required[111,112], such that a compensation temperature (at which the net magnetizations is zero) is present.

Based on these criteria, Mangin *et al.*[113] reported on multiple-pulse AO-HDS in different RE-TM alloys, RE-TM multilayers, and the coupled RE-TM heterostructures. Moreover, engineered synthetic ferrimagnets, which were only composed of the antiferromagnetically coupled TM-based FM layers, were also shown to host such AO-HDS. Such RE-free heterostructures showed a high technological potential because their materials are compatible with the spintronic memories. These findings seemed to verify the necessity of the three key ingredients, especially the presence of a compensation temperature in the AOS material.

AO-HDS in ferromagnetic systems

Later, multiple-pulse AO-HDS was observed surprisingly in several *ferromagnetic* thin films, multilayers and granular media[114,115]. The breakthrough soon led to another boost of the AOS field, due to the material compatibility with spintronic memory technologies. They also posed a challenge of the established AOS framework, questioning the generality of the established design rules[116].

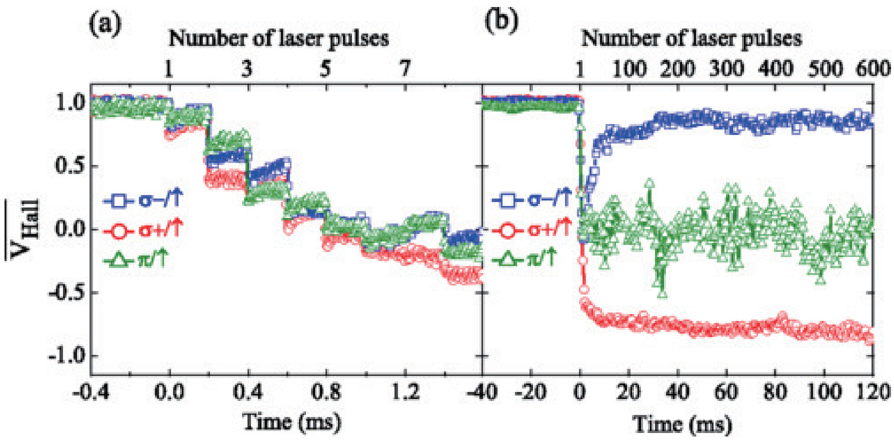

Figure 2.4: Multiple-pulse AO-HDS of the ferromagnetic (Co/Pt) multilayers. The magnetization evolutions upon consecutive fs laser pulses with different polarization were measured by AHE. Adapted from Hadri *et al.*[116]

Fig. 2.4 shows the magnetization evolution (as measured by the anomalous Hall voltage) of a Pt/Co/Pt multilayer upon subsequent fs laser pulses with either left (σ^-) or right (σ^+) circular or linear (π) polarization[116]. During the first few laser pulses, helicity-independent demagnetization of the sample was observed (Fig. 2.4 (a)). Afterwards, the magnetization recovered gradually upon subsequent laser pulses, where the direction was determined by the laser helicity (Fig. 2.4 (b)). Note that no remagnetization switching was observed using linearly polarized laser light. This result demonstrated the helicity dependence in the multiple-pulse AOS process. Further studies[117,118] revealed that such a helicity dependence originated from laser-induced domain wall (DW) motion. The underlying mechanism is not fully understood yet, but has been attributed to, e.g., the inverse Faraday effect[116,117,119], which was explored further by simulations using the M3TM model with an effective field[120], as well as *ab initio* studies[121].

In summary, after 10-year research efforts, two types of AOS mechanisms have been distinguished. One of them is the single-pulse AO-HIS, which is observed in the ferrimagnetic GdFeCo system. The AO-HIS is explained by a purely thermally-driven mechanism. On the other hand, multiple-pulse AO-HDS turned out to be a cumulative process, requiring several hundreds of laser pulses to achieve switching, thus losing the speed and energy advantages for spintronic integration.

Obviously, with an ultrafast opto-spintronic memory in prospect, the single-pulse AOS mechanism is of major technological relevance for spintronic integration. Aiming at this, verifying the single-pulse AOS in a spintronic device, especially an MTJ, has thus become a key scientific issue in this field. Further design of an AOS material system, aiming at a robust single-pulse AOS, high PMA, and high TMR, has also attracted considerable attention. In the following, we will introduce these research activities in more detail.

2.2 Integration of AOS with spintronic MTJ

By employing AOS to operate an MTJ, a spintronic-photonic integrated device idea was soon envisioned, which would exhibit a picosecond speed with least-dissipative energy consumption. To achieve this goal, the first key scientific objective was to verify the feasibility of AOS at a device level. In the following, several inspiring milestones toward these challenges are discussed.

2.2.1 AOS-MTJ device concept demonstration

Soon after the discovery of AOS in a variety of material systems, incorporating AOS in a realistic spintronic device has become an attractive scientific objective. The main idea is to manipulate the magnetic state by a short laser pulse, which later a while it can be read-out by electrical methods, rather than optical techniques (i.e., MOKE detection). As a first milestone, research efforts on electrical characterization of AOS in a patterned Hall cross by the anomalous Hall effect (AHE) were reported.

Among those activities, AOS of a fabricated GdFeCo Hall cross, using a near-infrared telecom-band femtosecond fiber laser[122], was demonstrated. This enabled an electrical readout of AOS by an AHE measurement. Similarly, AHE measurements were also performed on ferromagnetic Pt/Co/Pt heterostructures[123], enabling a statistical quantification of the multiple-pulse helicity-dependent switching.

In a following study by Chen *et al.*[124], GdFeCo films were patterned into pillars

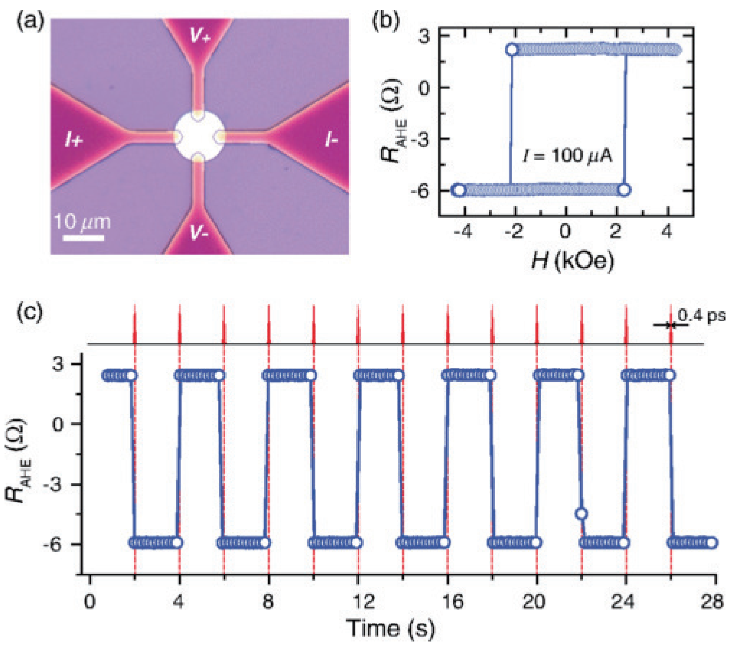

Figure 2.5: Direct magnetoelectrical AHE readout of the GdFeCo pillar upon single-pulse AOS measurement. (a) Optical microscope image of the pillar. (b) Hysteresis loop of the pillar measured by AHE, indicating a good PMA. (c) The AHE signal toggled upon every single laser pulse, confirming a robust and reproducible single-pulse AOS. Adapted from Chen *et al.*[124]

with a diameter of 15 µm, as shown in Fig. 2.5 (a). The measured hysteresis loop (Fig. 2.5 (b)) indicated good PMA with 100% remanence. Direct magnetoelectrical readout of the pillar upon exposure to a train of fs laser pulses was measured by the AHE method (Fig. 2.5 (c)). The AHE signal was reversed upon every single laser pulse, indicating a robust and reproducible single-pulse AOS of the magnetization in the GdFeCo pillar. These electrical characterization studies represented first steps toward opto-spintronic integration.

The work[124] further demonstrated the repeatability of AOS in the GdFeCo pillar, as shown in Fig. 2.6. The device was exposed to consecutive laser pulses with a repetition rate of 1 µs, meanwhile, the AHE voltage was measured with a sampling interval of 20 ms. In the setup, an acoustic-optic modulator (AOM) was used as a pulse picker, which was gated by electrical pulses. By proper tuning the width and duty ratio of the pulses generated by a signal generator, a group of laser pulses with an interval of 1 µs was realized. Briefly, the results revealed that, in case of an odd number of laser pulses, the AHE voltage was reversed to a high ohmic

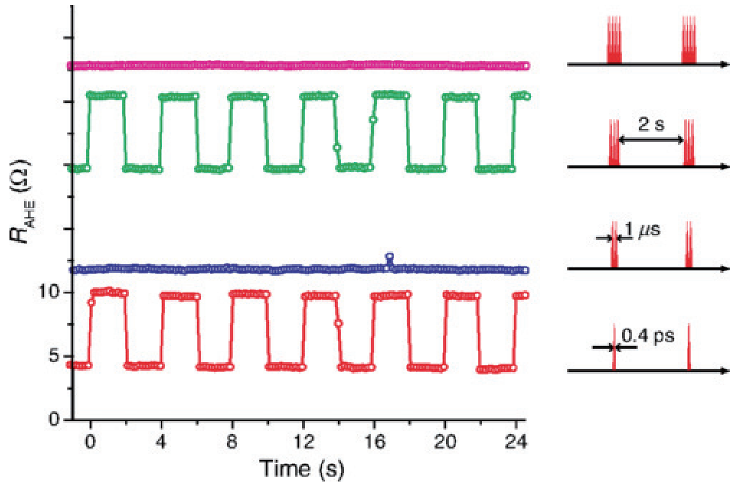

Figure 2.6: The repeatability of AOS in a GdFeCo Hall device. Consecutive laser pulses with a repetition rate of 1 µs were used to excite the device. This result showed that, in case of an odd number of laser pulses, the AHE voltage was reversed upon laser excitation, whereas in case of an even number of laser pulses, the AHE voltage toggled back to its original state, demonstrating an operation frequency of at least 1 MHz. Ref. from Chen *et al.*[124]

state. In contrast, in case of an even number of laser pulses, the AHE voltage toggled back to its original, low ohmic, state.

This result demonstrated a 1 MHz operation frequency of the device, but the ultimate AOS repetition rate remained unexplored for further investigations. Although the AOS usually takes tens of ps settling to a new equilibrium, it is believed that the next AOS process is possible prior to equilibrium. As a result, the opto-spintronic device is highly promising towards an ultimate operation frequency up to tens of GHz. However, the implementation of such devices requires careful design on material's thermal properties.

As one step further, employing GdFeCo as the FL of an MTJ was demonstrated[124], which was considered as another milestone towards opto-spintronic integration. The configuration of the designed MTJ is illustrated in Fig. 2.7 (a). Ta and Pd layers were used as the bottom electrode and the buffer. Co/Pd layers were used as the fixed layer, whereas a MgO layer was the tunnelling barrier. The FL consisted of all-optically switchable GdFeCo. Transparent indium tin oxide (ITO) was used to allow efficient optical access. The MTJ pillar was patterned using multistep

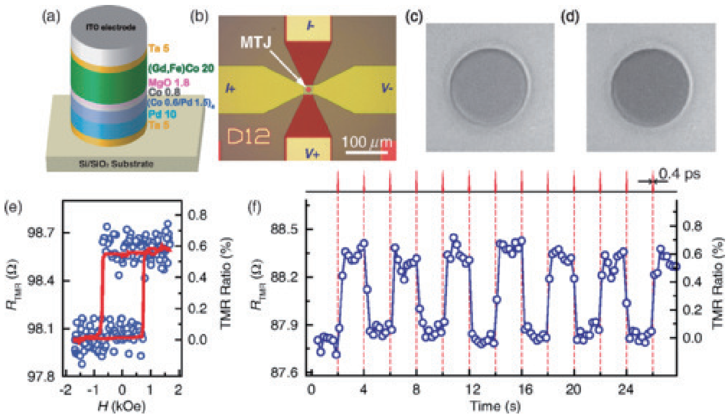

Figure 2.7: Single-pulse AOS of an MTJ employing the GdFeCo as the FL. (a) The configuration of the MTJ. The FL was the GdFeCo with PMA to enable AOS, whereas the MgO layer was the tunnelling barrier. (b) The fabricated MTJ device with a diameter of 12 µm. The transparent ITO was used as top electrode to enable efficient optical access. (c), (d) MOKE images of the MTJ device before and after AOS by single laser pulse. (e) $R-H$ loop measurement indicated a TMR ratio of 0.6%. (f) The resistance of MTJ toggled upon single-pulse AOS measurement, independent of the laser helicity. Adapted from Chen *et al.*[124]

optical lithography and ion beam etching (IBE), with a diameter of 12 µm.

As shown in Fig. 2.7 (e), a clear bi-stable $R-H$ loop with a TMR ratio of 0.6% was measured. Afterwards, the MTJ was exposed to consecutive linearly polarized fs laser pulses. The central wavelength of the laser was 1.55 µm (telecom band), with a pulse width of 0.5 ps. The repetition rate of the laser pulses was set at 0.5 Hz to distinguish each excitation, whereas its TMR was monitored in real time with a sampling interval of 100 ms.

Fig. 2.7 (f) shows that the resistance of the MTJ toggled upon each laser pulse, which was independent of the laser helicity. The TMR ratio was consistent with the value measured by sweeping a magnetic field, confirming a complete and reproducible switching. In addition, the MOKE images in Fig. 2.7 (c) and (d) proved that the magnetization of the GdFeCo layer was switched before and after AOS by a single laser pulse.

This work provided an inspiring precursor on verifying the AOS-MTJ device concept. However, some serious challenges have remained unsolved for the opto-spintronic field. Specifically, amorphous GdFeCo in direct contact with MgO led to a low tunnel spin polarization (TSP), resulting in an intrinsically low TMR ratio, which is far below the requirement for practical application.

In addition, although a 300°C thermal annealing is required for a high-performance MTJ deposition, the AOS effect in the GdFeCo alloys is extremely sensitive to the alloy composition and the annealing temperature. Moreover, GdFeCo is a soft magnetic material with a low anisotropy. Such a device will become thermally unstable and superparamagnetic after scaling down to below 200 nm, thus challenging towards integration with the advanced CMOS technology node.

2.2.2 Material design and optimization for AOS-MTJ

In this sub-section, further material-orientated work aiming for a practical AOS-MTJ with high performance is discussed. Furthermore, design and optimization of the AOS-MTJ's performance, including the thermal stability, energy efficiency, and scalability, are also presented.

As to the conventional MTJ design, a ferromagnetic system with a strong PMA and a high TSP has been widely adopted, such as Co/Pt or CoFeB/MgO[66]. However, multiple-pulse AOS is required for switching these ferromagnets, losing advantages on speed and efficiency. On the other hand, an MTJ employing a single GdFeCo layer exhibits a low PMA and TMR.

To address this dilemma, the exchange coupling of the AOS layer with a ferromagnetic layer has become a mainstream technological route. Among them, researchers from University of California[125] demonstrated single-pulse AOS in a ferromagnetic Co/Pt multilayer that was exchange coupled to a GdFeCo layer. They observed that the nanostructure switched within several ps due to the effective coupling. This general design route is highly promising to extend to other ferromagnetic systems with high TSP.

As a consequence, researchers from Spintec[126] designed an all-optically switchable Co/Tb multilayer that was coupled to a CoFeB electrode using a 0.2-nm-thick Ta layer. Such a CoFeB electrode in direct contact with MgO leads to high TSP, as heavily used in STT-MRAM technology. A simultaneous single-pulse AOS of this MTJ electrode was achieved due to the strong ferromagnetic coupling.

A further attempt on integration such an all-optically switchable electrode with a prototype MTJ was initiated[127], with a configuration of Ta/CoFeB/MgO/CoFeB /Ta/$(Co/Tb)_5$. The bottom CoFeB was used as the other FM layer of the MTJ, whose magnetization was not fixed by a bottom-pinned structure. After fabrication, the MTJ pillar showed a TMR up to 38%.

However, laser-indued operation of such a device was not successful yet, whereas a toggle TMR switching upon single-shot laser excitation is a basic operation for each binary memory. Furthermore, the magnetization dynamics of the AOS in such a nanoscale device remained unknown. Lastly, as to practical MRAM applications, a bottom-pinned RL is highly required. For an AOS-MTJ, a carefully design of the RL to minimize its stray field is nontrivial, since the stray field from the RL will affect the AOS process in the nanoscale device.

Thus, a fully functional AOS-MTJ with a robust AOS, a high TMR and a high Δ has not been demonstrated yet. A direct experimental proof of the operation speed, along with the time-resolved switching dynamics, requires further investigation. In Chapter 3 of this thesis, such a systematic study of the AOS dynamics of an MTJ is reported.

2.2.3 Synthetic ferrimagnetic multilayers: an ideal platform for AOS integration

As discussed above, amorphous GdFeCo alloys typically show a low anisotropy and a low spin polarization, and these alloys are also complex to tune their magnetic properties by adjusting the alloy composition. To address these shortages, crystallized AOS materials, especially synthetic ferrimagnetic multilayers[128], have gained considerable attention due to their substantial potential towards spintronic

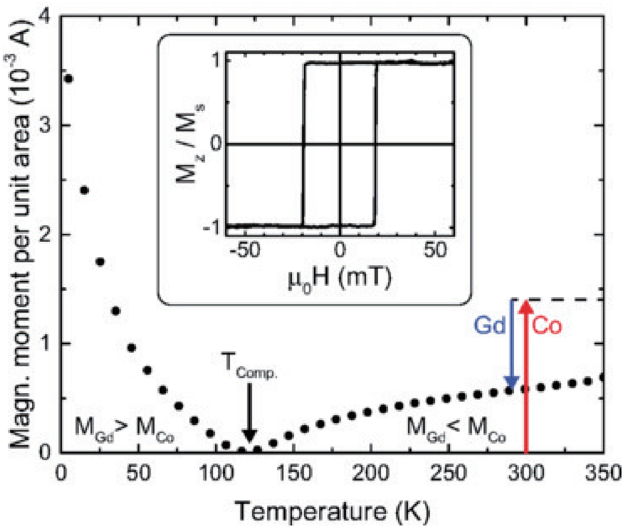

Figure 2.8: Inset: Hysteresis loop of the Pt/Co/Gd stack confirmed a well-defined PMA. Main: Magnetic moment per unit area measured by SQUID-VSM as a function of temperature. The antiferromagnetic coupling between the Co and Gd layers was demonstrated by the presence of a compensation temperature at 120 K. Adapted from Lalieu *et al.*[128]

integration.

Specifically speaking, in recent work, researchers from the Eindhoven University of Technology[128] demonstrated that helicity-independent single-pulse toggle switching could be also realized in ferrimagnetic Pt/Co/Gd stacks with PMA. The Curie temperature of bulk Gd lies just below room temperature, however, in the Pt/Co/Gd system, the Gd layer has a proximity-induced magnetization in an atomically thin region near the Gd/Co interface, which is antiferromagnetically coupled to the Co layer. The Pt seed layer in contact with Co leads to the presence of a strong PMA. The thermal AOS was realized due to the large contrast in their demagnetization times, as similar in ferrimagnetic alloys.

As illustrated in Fig. 2.8, the hysteresis loop of the stack, was measured by the magneto-optical Kerr effect, confirming a well-defined PMA due to the square shape with 100% remanence, Afterwards, the antiferromagnetic coupling[129,130] between the Co layer and the Gd layer was demonstrated by the presence of a compensation temperature at 120 K as measured by SQUID-VSM. At this temperature, the magnetic moments of the Co and Gd layers compensated each other

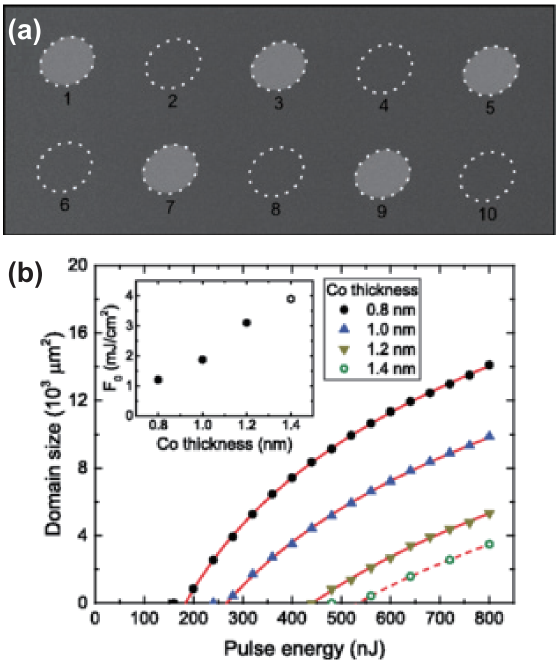

Figure 2.9: (a) Single-pulse AOS measurement of the Pt/Co/Gd stacks. The labels indicated the number of pulses each spot was exposed to. For every odd number of laser pulses, a homogeneous domain with an opposite magnetization direction was written, whereas no net magnetization reversal was observed for every even number of pulses. (b) Domain size as a function of pulse energy for stacks with different Co thickness. The threshold fluence was derived, which was lower than that of the GdFeCo alloy. Adapted from Lalieu *et al.*[128]

due to an antiparallel and equal alignment.

They then experimentally demonstrated helicity-independent single-pulse AOS of the Pt/Co/Gd stacks, which were exposed to consecutive linearly polarized 100-fs laser pulses. Magneto-optical Kerr microscopy was used to examine the magnetization state after AOS, as illustrated in Fig. 2.9 (a). The labels indicated the number of pulses each spot was exposed to. For every odd number of laser pulses, a homogeneous domain with an opposite magnetization direction was written, whereas no net magnetization reversal was observed for every even number of pulses. This behavior is consistent with the single-pulse AOS mechanism discussed in GdFeCo, in which the AOS was driven by transferring angular momentum[131,132] mediated by exchange scattering between the Gd and Co sublattices[133].

As to the energy efficiency, the AOS threshold fluence was determined by measuring the domain size as a function of the laser pulse energy, which will be explained in detail in Chapter 3. A threshold fluence down to 1 mJ/cm^2 was derived as shown in Fig. 2.9 (b), which is significantly lower than that in GdFeCo alloys (2.6 $\pm$ 0.2 mJ/cm^2)[101].

The synthetic ferrimagnetic multilayers fully facilitate the ultrafast AOS speed with energy efficiency, as well as high PMA. The system also shows extended flexibility on the fabrication process. This means that it is easier to tune their magnetic properties by simply controlling the film thickness during sputter deposition. In addition, as to interface engineering, this system has been demonstrated to show high domain wall (DW) velocity[129], and inherent built-in interfacial Dzyaloshinskii-Moriya interaction (iDMI). These advantages make Pt/Co/Gd highly suitable towards spintronic integrated devices.

One appealing device concept is to integrate this synthetic system with the racetrack memory[134]. Specifically, optically written domains could be coherently moved along the racetrack at high speed by the current-induced spin Hall effect (SHE). The researchers from the Eindhoven University of Technology[135] presented a proof-of-concept demonstration of this "on-the-fly" all-optical data writing in the racetrack. A more detailed discussion is presented in the following.

As illustrated in Fig. 2.10 (a), the AOS in the Pt/Co/Gd racetrack was investigated by exposing a train of linearly polarized laser pulses ($\approx$ 100 fs), which was set at a low repetition rate of 0.5 Hz, meanwhile, the AHE voltage was measured. Fig. 2.10 (b) confirmed a robust and reproducible toggle AOS of magnetization in the patterned Pt/Co/Gd racetrack.

Afterwards, "on-the-fly" SHE-driven transport measurements on these optically written domains were performed. Due to the inherent built-in iDMI[129], the domain walls could be moved coherently along the racetrack, which was originated from the current-induced SHE[136,137] in the heavy-metal Pt seed layer. In the measurement, as illustrated in Fig. 2.11 (a), a domain was written in the first leg of the wire by AOS. Meanwhile, a DC current was flowing through the wire. As a result,

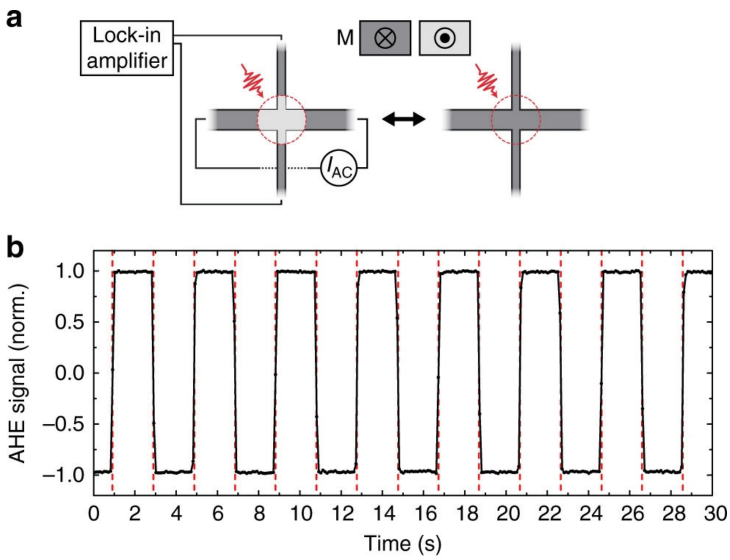

Figure 2.10: (a) Schematic overview of the AOS measurement in the Pt/Co/Gd racetrack. (b) By exposing a train of linearly polarized laser pulses, the toggled AHE voltage of the Hall crosses as a function of time confirmed a robust and reproducible single-pulse AOS. The repetition rate of the laser was set at 0.5 Hz. Adapted from Lalieu *et al.* [135]

the domains would move coherently along the current direction by the SHE as soon as they were written. This means that the full domain would be transported along the wire, passing the second Hall cross, and measured using AHE.

The AHE signals of the two legs as a function of time are shown in Fig. 2.11 (b). As to the first leg, the small peaks appeared in the AHE signal, whereafter it was quickly recovered to the saturation state, indicating that the domain was moved out of the cross. As to the second Hall cross, it was switched down (−1) shortly after AOS, then, it was switched back up (+1) again. These results indicated the transport of the optically written domain. The device feasibility was further verified using a Kerr microscope, as shown in the inset of Fig. 2.11 (b). This proof-of-concept demonstration showed that the Pt/Co/Gd racetrack is an ideal candidate to facilitate the integration of AOS with spintronics, exhibiting great potential to stimulate the innovation of future & emerging technologies (FET).

In this thesis, the main scientific aim is to develop a fully functional spintronic-photonic memory by integrating AOS with MTJs. Followed by the mainstream

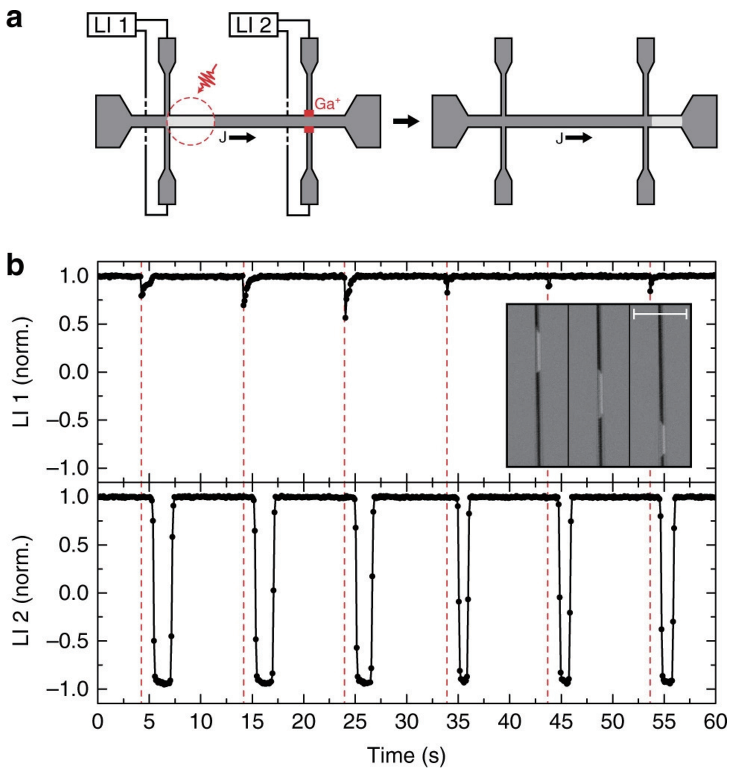

Figure 2.11: (a) Illustration of the device concept on integrating AOS with racetrack memory. "On-the-fly" SHE-driven transport of the AOS domains in a Pt/Co/Gd wire was measured by AHE signal in two Hall crosses. (b) Measurement results illustrated above. In the first leg, small peaks of the AHE signal were first observed, after a while, it was quickly recovered to the original state. In the second leg, the AHE signal was switched shortly after AOS, then it was toggled back again. These results indicated the transport of the optically written domain. Inset: Kerr microscope image verifying the SHE-driven domain wall motion. Adapted from Lalieu *et al.*[135]

technological route of the emerging AOS field, key scientific objectives are refined, which construct the research work of the thesis, as shown in the next 4 chapters. The output of the thesis is a first fully functional picosecond AOS-MTJ memory, which may ultimately pave the way towards large-scale opto-MRAM arrays with ultrafast speed and low power consumption.

3

Methodology

In this chapter, the experimental techniques on the deposition, fabrication and characterization used in this thesis are introduced. In the first part of this chapter, we start with an introduction of magnetron sputter deposition, which is employed to grow all the multilayered nanostructures investigated in this thesis. Afterwards, the fabrication process flow of the MTJ is presented, including thermal annealing, ultraviolet lithography, ion-beam etching and electron beam evaporation. In the second part, various characterization techniques used in the thesis are introduced. The magnetic characteristics of the thin-film samples are measured using vibrating sample magnetometry (VSM). The static and time-resolved magneto-optical Kerr effect (MOKE) measurements used to study laser-induced magnetization dynamics, as well as a dedicated Kerr microscope, are discussed. Finally, we introduce the AOS measurement setup, as well as the method for deriving the AOS threshold fluence. Lastly, the four-point TMR measurement of the MTJ device is presented.

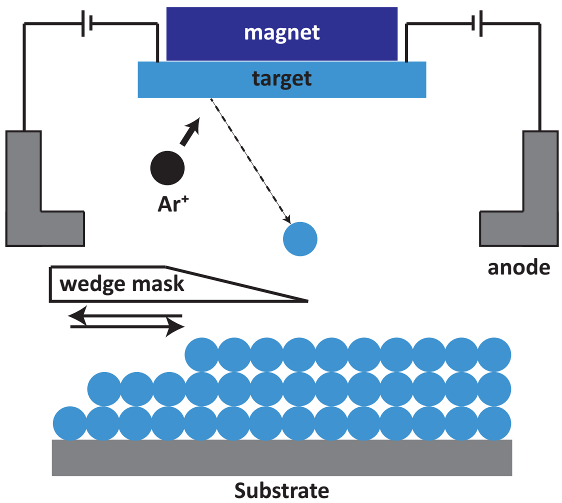

Figure 3.1: Schematic drawing of the magnetron sputter deposition. A high voltage is applied between the cathode target and an anode, ionizing the Ar gas into Ar^+ plasma. The highly energetic Ar^+ ions are accelerated toward the cathode target due to the electrical field potential, and bombard the target material. A magnet is set behind the target cathode to enhance the collision probability between the electrons and the Ar gas. These sputtered atoms from the target are then deposited on the substrate and form a thin film.

3.1 Sample deposition

This section introduces the deposition of the multilayered thin-film structures using magnetron sputtering.

As a mainstream deposition method for high-quality multilayered nanostructures, magnetron sputtering is a typical physical vapor deposition technique (PVD) with atomic precision, simplicity, and relatively high rate. The schematic overview of the magnetron sputtering technique is shown in Fig. 3.1. Before the sputtering process, the thermally oxidized Si substrate, which is commercially available, is cleaned thoroughly by ultrasound acetone bath. The preclean of the substrate is essential because the performance of an MTJ is extremely sensitive to the substrate uniformity. This 100-nm-thick SiO_2 oxidized layer offers good electrical isolation and sufficient heat diffusion performance. Afterwards, it is loaded to the sputter chamber.

The sputter chamber is maintained at ultra-high vacuum, with a typical base pressure of 10^{-8} mbar to prevent contamination. During the sputter deposition, the inert Argon gas with high purity is filled in the sputter chamber, elevating the pressure to 10^{-3} mbar. Meanwhile, a high voltage is applied between the cathode target and the anode, ionizing the Ar gas into Ar^+ plasma. The highly energetic Ar^+ ions are accelerated toward the cathode target due to the electrical field potential, and bombard the target material. For target materials such as metals, a direct-current (DC) power supply is used, whereas for insulating materials such as MgO, a radio-frequency (RF) power supply is required. In magnetron sputtering, a magnet is set behind the target cathode to confine electrons, which is employed to enhance the collision probability between the electrons and the Ar gas, promoting the ionization of the Ar plasma, and eventually the sputter rate. These sputtered atoms from the target are then deposited on the substrate and form a thin film.

In some cases, an in-situ characterization of the deposited nanostructure as a function of its thickness is highly desired. This requirement could be easily met using a wedge-shaped shutter mask set close to the sample. During sputtering, the mask is move linearly along the sample surface, leading to a wedge-shaped thin film (i.e., with a horizontal gradient in thickness). Such a technique is widely used to investigate the properties of a nanostructure as a function of its thickness, because of its high thickness resolution, rather than a large number of separated samples, as well as process variation during deposition.

The samples used throughout this thesis are all grown by DC/RF magnetron sputtering at room temperature with a base pressure of 10^{-8} mbar. As to the deposition of CoFeB/MgO based MTJ, a systematically control on deposition parameters is required. Specifically, the quality of MgO growth has a decisive effect on the device performance, such as PMA, TMR and resistance area product. Optimizing the key parameters during MgO deposition, including Ar pressure, sputtering rate, and DC/RF power, is of utmost importance for obtaining a high-performance MTJ. In addition, the uniformity of the substrate and the bottom electrode is also critical for the presence of PMA. The advantages of magnetron sputtering include high deposition speed, high reproducibility, and high uniformity in a wide thickness range. Moreover, it offers the availability to deposit compound (alloy) material directly from the corresponding alloy target. All these advantages make magnetron sputtering a versatile method for thin-film growth with an atom-thick precision in industrial applications. A more in-depth review on the magnetron sputtering can be found elsewhere[138,139].

3.2 Sample fabrication

In this section, the fabrication process and tools to pattern down these thin-film samples to several micrometer dimension are described. We start with a brief overview of the process flow of the MTJ fabrication used in this thesis. The basics principles, as well as some details of each step, are discussed in the following.

3.2.1 Overview of fabrication process flow

As the basic building block of MRAM, the fabrication of an MTJ is of utmost importance for spintronic applications. In the following, we present the process flow of the MTJ fabrication. As a current-perpendicular-to-plane (CPP) device[140,141], the key challenge on the MTJ fabrication is the electrical isolation between the bottom electrodes and the top electrodes. In this thesis, the conventional top-down process is employed due to its compatibility with industrialization.

The schematic overview of the process flow is illustrated in Fig. 3.2. A general introduction of the whole fabrication stream is previewed, whereafter a more detailed description on each technical process step is discussed in the following. Briefly, after the sputter deposition, the full-sheet MTJ stack is then subject to thermal annealing. Then, the bottom electrode is patterned using ultraviolet (UV) optical lithography and Ar ion beam etching (IBE), respectively. Next, the circular MTJ pillar is patterned using similar technique (UV lithography and IBE). The SiO_2 protection layer is evaporated to cover the whole pillar using electron beam (E-beam) evaporation, which is used to ensure electrical isolation between the bottom and top electrode, and to prevent thermal oxidation of the pillars. Lastly, the top electrode of the MTJ is patterned using UV lithography and E-beam evaporation, followed by a lift-off procedure. Note that the MTJ fabrication in this thesis is

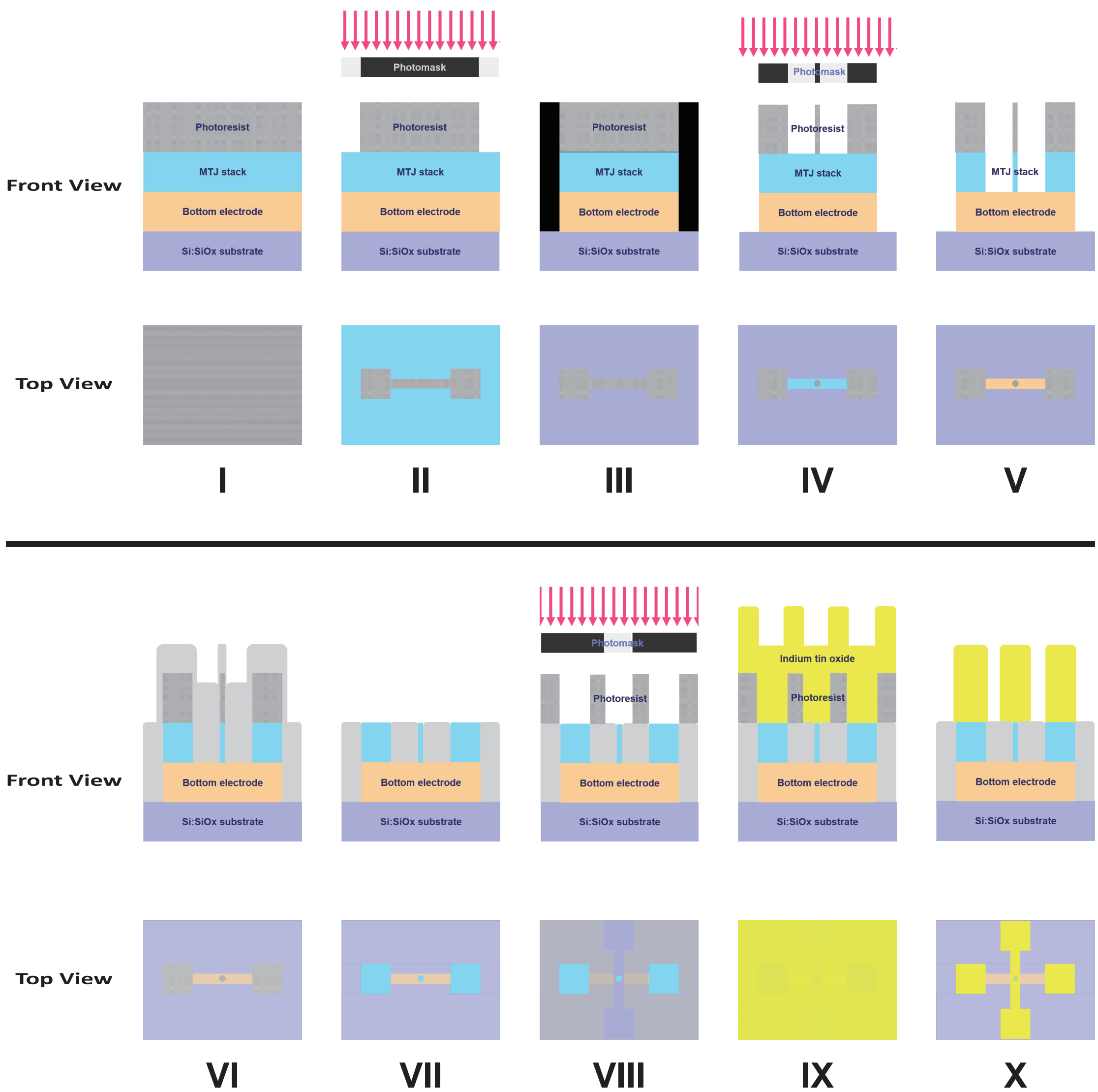

Figure 3.2: Schematic overview of the MTJ fabrication process flow. I – III: Ultraviolet (UV) lithography in combination with Ion beam etching are used to pattern the bottom electrode. IV – V: The circular MTJ pillars with a micron-sized dimension is patterned using similar techniques. VI – VII: The SiO_2 protection layer is evaporated to cover the whole pillar using E-beam evaporation and a lift-off technique. VIII: Ultraviolet (UV) lithography in combination with Ion beam etching is used to transfer the top electrode pattern to the sample surface. IX – X: The top electrode contacts are deposited using e-beam evaporation followed by a lift-off procedure.

based on a relatively standard process developed by Beihang University.

As a first procedure of the process flow, UV lithography in combination with IBE is employed to pattern the bottom electrode. The procedure starts by spin coating (Fig. 3.2.I) a positive photoresist (AZ702) layer of approximately 1 µm thickness on the sample surface, whereafter the pre-bake process using a hot plate is performed at 90°C for 90 s. The prebake process is used to remove the solvents in the photoresist. The sample is then exposed to ultraviolet light with a lithography mask. The photoresist on the irradiated region is removed by immersing the sample to the developer (PD238) for 15 s (wet removal technique), whereafter it is cleaned by water and blow-dried using Nitrogen gas. As the photoresist on the unexposed regions are conserved, an anisotropic dry ion beam etching technique is employed to transfer the pattern from the lithography mask to the thin-film surface, as shown in Fig. 3.2.II.

Subsequently, the MTJ pillar with a micron-sized dimension is patterned using similar techniques (UV Lithography in combination with IBE). This process also starts by spin-coating a thin (around 1 µm) photoresist layer onto the sample surface, which is positive AZ702 in our case, Fig. 3.2.III. Similarly, a pre-bake on a hot plate is performed to remove the solvents (90°C, 90 s). Upon exposure to the UV irradiation, the required MTJ pillar pattern is transferred onto the photoresist, Fig. 3.2.IV. After removing the photoresist using developer PD238 for 15 min, the remaining photoresist is hardened by a post-bake on the hot plate (110°C, 3 min). The MTJ pillar is etched from top to down using IBE with a tilting angle of 35° and real-time monitoring, Fig. 3.2.V. The SiO_2 protection layer is then evaporated to cover the whole pillar using E-beam evaporation and a lift-off procedure, Fig. 3.2.V – VI.

Next, the top electrode is patterned, which starts by spin-coating 1 µm negative photoresist 4620 on the sample. After a pre-bake process at 110°C for 90 s, the UV lithography followed by a wet-removal technique using PD238 is used to transfer the top electrode pattern to the sample surface (Fig. 3.2.VII – VIII). The Ti/Au or indium tin oxide (ITO) electrical contracts are created using E-beam evaporation, Fig. 3.2. IX. Lastly, the remaining photoresist, as well as the material evaporated on its top, is removed thoroughly by a lift-off procedure Fig. 3.2, X. The process consists of acetone immersion for 12 h and an ultrasound bath twice, whereafter it is cleaned by ethanol and blow-dried using Nitrogen gas. The performance of the fabricated device is checked by optical microscope and electrical TMR measurements. A more detailed discussion on each step will be presented in the following.

3.2.2 Thermal annealing

After deposition of the MTJ full-sheet stack by magnetron sputtering, the samples are subject to high temperature at a vacuum chamber for an hour, which is termed as thermal annealing. Optionally, an external magnetic field is applied to set the preferential direction of the easy axis, i.e., the magnetic anisotropy. In case of certain layers of the nanostructure that are intolerable to high temperature, an in-situ annealing, namely, annealing each layer locally in the course of sputtering, would offer a suitable method.

The post-annealing process is an essential process for optimizing CoFeB/MgO based MTJ performance. During annealing, amorphous CoFeB will crystallize to a bcc structure induced by the MgO (001), which is critical to obtain a high TMR and PMA. The heat diffusion of the Boron element upon annealing also improves the quality of the stack. In addition, thermal annealing offers an effective way to manipulate magnetic characteristics, such as coercive field (H_c), saturation magnetization (M_s), as well as PMA. Typically, the optimized annealing temperature for CoFeB/MgO-MTJ is around 300°C – 350°C, above which the both the M_s and the effective magnetic anisotropy energy (K_{eff}) will be deteriorated. Consequently, enhancing the annealing tolerance and the thermal stability of MTJ is another challenge for the large-scale MRAM industrialization, aiming for a full compatibility with the COMS post-annealing process.

It's also demonstrated that, in synthetic ferrimagnetic Gd/Co bilayer systems, annealing acts as a powerful tool to manipulate interfacial effects, such as the domain wall dynamics and the AOS threshold. In Chapter 4, the synthetic ferrimagnetic thin-film stacks are annealed for 0.5 h with temperature ranging from 0°C to 400°C, whereafter the annealing effects on magnetic characteristics and AOS efficiency on each sample are measured. The result shows that the AOS efficiency of Gd/Co bilayer is enhanced after annealing at 300°C, indicating its prospect on MTJ integration. In Chapter 5 and Chapter 6, the MTJ full-sheet stacks are annealed at 300°C in a vacuum for 1 h after deposition, which is used to enhance TMR and PMA of the device.

3.2.3 Ultraviolet optical lithography

UV optical lithography is a typical technique widely used for nanofabrication[142,143]. It is a critical procedure to transfer patterns with a feature size of sub-micrometer resolution using UV irradiation at a certain wavelength. The advantages of this technique include the large-area exposure, high reproducibility, and low cost.

In this thesis, UV lithography is used to create micron-sized MTJ pillars and electrical pads, respectively, as illustrated in Fig. 3.2. Before the process, the lithography mask with a required pattern is designed, which is made of opaque chromium metal. The mask is set between the UV light source and the sample surface. The lithography process starts by spin-coating a thin photoresist on top of the sample surface, leading to a uniformly coated layer caused by the centrifugal force at high-speed rotation. Afterwards, the sample is baked using a hot plate at 110°C for 90 s to remove solvents. The photoresist is a category of organic chemical, with its solubility changing upon UV light irradiation. As to the negative photoresist, the region within UV exposure hardens, resulting in a hard mask after development. As to the positive photoresist, the region where the UV light exposed will be dissolved in the developer.

During the lithography process, the UV light is employed to transfer the mask pattern to the photoresist above the sample surface. Then, the chemical developer removes part of the soluble photoresist. Afterwards, IBE technique is employed to mill away regions without hard mask protection, whereas the areas covered with photoresist is kept. As multiple lithography processes are used during MTJ fabrication, alignment marks are created on the lithography masks to eliminate pattern misalignment. The ion-beam etching technique will be discussed in the next section.

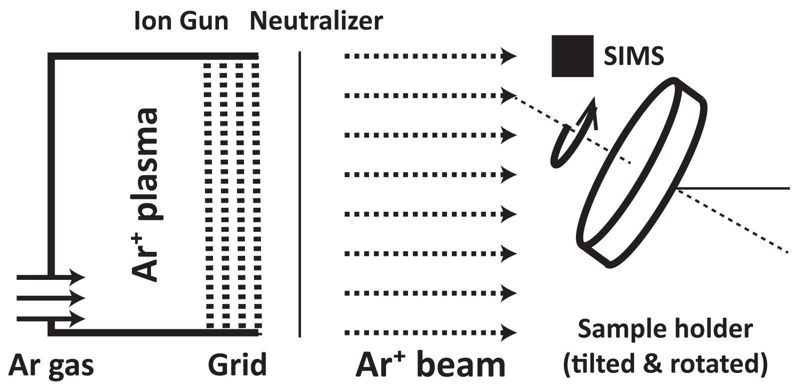

Figure 3.3: The working principle of ion beam etching process. The surface of the sample is bombarded by a parallel beam of energetic Ar^+. The accelerated Ar^+ beam transfers its momentum to the surface atoms, causing the target (sample surface) to be etched away. A rotatable sample holder and an optimized etching tilt angle at 35° (relative to the normal of the sample surface) is used to eliminate the redeposition phenomena during etching.

3.2.4 Ion-beam etching

Ion-beam etching (IBE) is an anisotropy dry etching technique with high universality and homogeneity. It employs a highly energetic parallel ion beam to etch the whole sample surface, and thus transfer the pattern from the photoresist to the thin-film surface. The working principle of IBE is illustrated in Fig. 3.3. During the etching process, the sample surface is bombarded by an accelerated beam of energetic Ar^+ up to several keV, which transfer their momentum to the surface atoms, causing them to be etched away. Moreover, a rotatable sample holder and an optimized etching tilt angle at 35° (relative to the normal of the sample surface) is used. Such a configuration would eliminate redeposition during etching, thus ensuring a homogeneous etching on both sides, which would also promote the steepness of the pillar sidewall.

To monitor the etching process in real time, the secondary ion mass spectrometer (SIMS) is equipped with an end-point detection, which is regarded as a quantitative method by measuring the element-specific mass-charge ratio of the ejected secondary ions. The etching rate of IBE is generally determined by the ion beam energy, beam density, as well as the etched material. As a result, a systematic optimization for high-quality etching is highly required. Due to the material-dependent etching rate with a high selectivity, the regions covered with photoresist are used as a hard mask, of which the etching rate is much lower than that of the sample surface needed to be patterned (typically 0.5 nm/s). The challenges for employing IBE in large-scale industrial production include etching precision for high-density pattern arrays, and a highly uniform ion-beam source for 6-inch Si substrate with high directionality as well.

3.2.5 Electron-beam evaporation

Electron-beam (E-beam) evaporation is also a commonly used physical vapor deposition technique[144,145]. In the MTJ fabrication, E-beam evaporation is used to deposit the top electrodes (Ti/Au or ITO) and the isolation layer for the MTJ device. During the process, the source material is evaporated in a high vacuum atmosphere. The vapor particles travel directly to the deposition target (substrate) in a high vacuum chamber, without colliding with other gas particles. Afterwards, they condense back into a solid state. Note that hot objects in the evaporation chamber, such as the heating filaments, would produce undesired vapor particles that deteriorate the process quality. After the E-beam evaporation, the remained photoresist is removed via a lift-off process by acetone for 12 hours at room temperature, whereafter ultrasonic cleaning and deionized water are used to clean the sample.

3.3 Measurement techniques

In this section, the heavily used techniques and setup for magnetic characterization in this thesis are introduced. This section starts with an introduction on Vibrating sample magnetometry (VSM). Next, a general introduction on magneto-optical Kerr effect (MOKE) is presented, followed by a detailed discussion on various MOKE configurations and setups. Specifically, the static MOKE is used to characterize the magnetic properties, and the time-resolved MOKE is used to investigate ultrafast magnetization dynamics . In addition, spatially-resolved Kerr microscopy is used to directly observe magnetic domains. Lastly, electrical transport measurement of the MTJ using tunnel magnetoresistance (TMR) effect is also presented.

3.3.1 SQUID-VSM

VSM is a typical technique to characterize the static magnetic properties of a sample, typically the hysteresis loop. As to the working principle of the VSM[146,147], the sample is set near a coil and starts vibrating, meanwhile an oscillating magnetic field originated from the magnetic moment of the sample is detected by the coil. Such an oscillating magnetic field will induce a current in the coil, which is proportional to the magnetic flux in the coil loop. Consequently, by measuring the induced electrical signal, the local magnetic moment of the sample can be determined. Similarly, the magnetization as a function of the magnetic field, can be measured based on this principle by applying an external field using conventional electromagnets or superconducting magnets for field strengths up to 16 T. VSM based on such sensing coils is constrained by a noise level of 10^{-9}A·m^2.

As to the nanostructured thin film with a low magnetic moment, VSM with a superconducting quantum interference device sensor (SQUID-VSM)[148] offers a detection resolution in the limit of 10^{-11} A·m^2 for practical measurement environment, (the highest sensitivity reached 10^{-15} A·m^2). Such a performance is highly suitable for our synthetic ferrimagnetic multilayered samples with a low net magnetic moment. It is noted that, due to the demagnetizing effect, the actual magnetic field exerted on the sample differs from the external field. Therefore, to perform a precise characterization on the local magnetic moment, care has to be taken to correct such demagnetization effects.

Moreover, in this thesis, it is often essential to precisely extract the magnetic properties of the sample as a function of temperature. Using the SQUID-VSM with a temperature range from 1.7 K to 400 K, such measurements are performed. The $M(T)$ measurement is critical to determine the compensation temperature (T_{comp})(for ferrimagnetic samples) or Curie temperature (T_C).

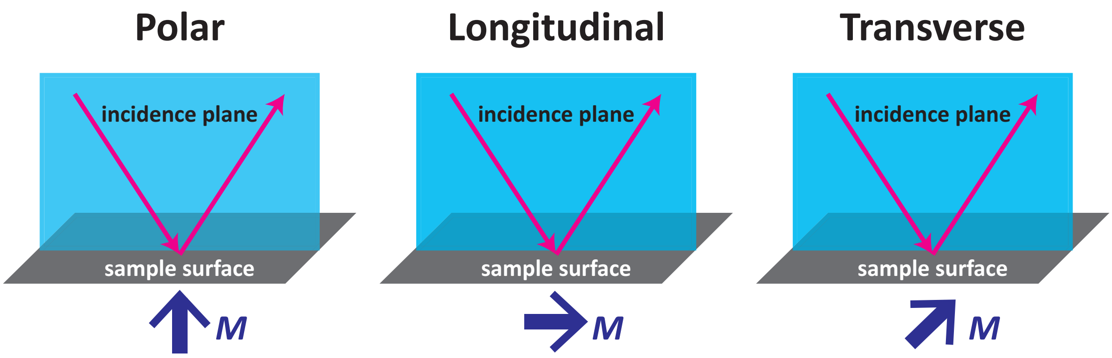

Figure 3.4: Schematic drawing of the MOKE in three different configurations. The specification is according to the magnetization direction with respect to the incident plane, as well as the reflecting surface. (a). In the polar MOKE configuration, the magnetization is perpendicular to the sample surface. In this case, the reflected MOKE signal is only sensitive to the out-of-plane component of the magnetization. (b). In the longitudinal MOKE configuration, the magnetization of the sample is parallel to the sample surface and the incidence plane. (c). In the transverse MOKE, the magnetization is parallel to the sample surface but perpendicular to the incidence plane.

3.3.2 Magneto-optical Kerr (MOKE) effect

When a beam of polarized light reflects from a magnetic material, the polarization direction will rotate and gain an ellipticity, which is called the Magneto-Optic Kerr Effect (MOKE). It was first discovered by John Kerr in 1877[149]. In fact, the most well-known magneto-optical effect on light-material interaction is the Faraday effect found in 1845[150], which is regarded as the emergence of the field of magneto-optics. Faraday observed that the polarization of the light rotates when it transmits through a transparent material with an applied magnetic field along the light propagation direction. MOKE is another common way to characterize the magnetic characteristics of the sample[151,152]. Despite it provides no quantitative determination of the magnetic moment, the advantage of MOKE is its fast-measuring speed with a relatively high accuracy in a local-probe setup[151].

Phenomenologically speaking, the MOKE effect originates from the fact that the complex refractive index of the two circular modes with opposite helicity is different in a magnetic material. Upon reflection, the light actually transmits through the magnetic medium (around 20 nm for typical metals). As a result, such two modes of the incoming light travel at different velocities with different absorption, leading to a change in the phase and amplitude of the incident light. More specifically, the phase change results in a rotation of the polarization axis, which is termed as the Kerr rotation, whereas the amplitude change causes the Kerr ellipticity. Note that both the Kerr rotation and Kerr ellipticity can be used to measure the magnetization, since the real part and imaginary part in refractive index is directly proportional to the magnetization of the material[153,154].

The magnetization of the sample can be measured in three different MOKE configurations, depending on the alignment direction of the magnetization with respect to the incident plane and the reflecting surface, as shown in Fig. 3.4. In the polar MOKE configuration, the magnetization is aligned perpendicularly to the sample surface (out-of-plane), i.e., parallel to the plane of incidence. In the case of the polar MOKE, the sensitivity to the out-of-plane component of the magnetization is the highest when the incident beam is perpendicular to the sample surface. For our PMA samples, a polar MOKE configuration is usually used with a perpendicular incident laser beam.

In the longitudinal MOKE configuration, the magnetization of the sample is parallel to the sample surface and the incidence plane. In the transverse MOKE, the magnetization is parallel to the sample surface but perpendicular to the incidence plane. Note that the transverse MOKE only results in an intensity change of the Kerr signal (Kerr ellipticity), without a polarization change of the Kerr signal (Kerr rotation). However, care must be taken when analysing the MOKE signal. The detected MOKE signal may be a combined effect under the above three MOKE configurations, due to an arbitrary magnetization direction. In the following, the MOKE measurement setup will be introduced based on the polar configuration. A more quantitative discussion of the physics behind the MOKE technique can be found elsewhere[155].

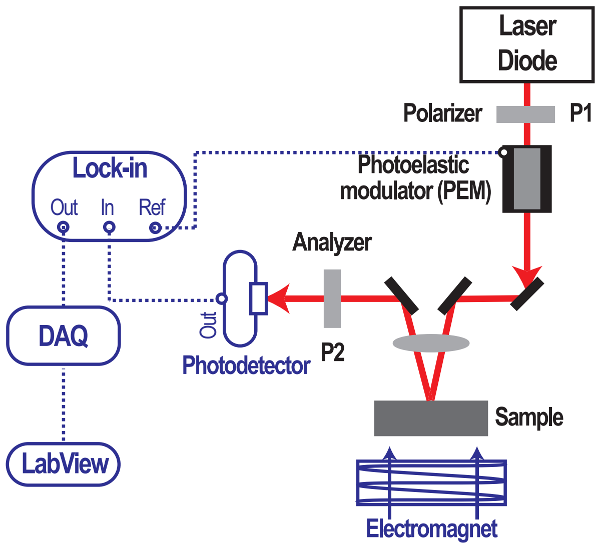

Figure 3.5: Schematic drawing of the static MOKE measurement setup. The incidence light travels through the polarizer P1, and is linearly polarized. Afterwards, it is reflected from the sample surface. The light is reflected back to the analyzer P2 (aligned in a cross-polarized configuration with P1.), whereafter its intensity is measured by a photodetector. The PEM in combination with the lock-in amplifier is used as a modulation technique to enhance the SNR of the measurement.

3.3.3 Static MOKE setup

The basic components for the static MOKE setup are two polarizers, which are termed as the polarizer (P1) and the analyser (P2), as is illustrated in Fig. 3.5. Upon traveling through the polarizer P1, the incident laser beam (laser diode, center wavelength of 658 nm) is polarized linearly, whereafter it is reflected from the sample surface. The reflected beam is sent back through the analyzer P2, whereafter its intensity is measured by a photodetector. The laser spot size is $\approx$ 50 µm in diameter, which could be focused to sub-µm using high-resolution objectives. By sweeping an external magnetic field, this MOKE setup is highly suitable for measuring the static response of the magnetization characteristics such as the hysteresis loop.

In order to enhance the signal-to-noise ratio of the detected signal, as well as to eliminate the non-magnetic background, the analyzer P2 is aligned almost perpendicular to the first polarizer P1. Moreover, a photo-elastic modulator (PEM)

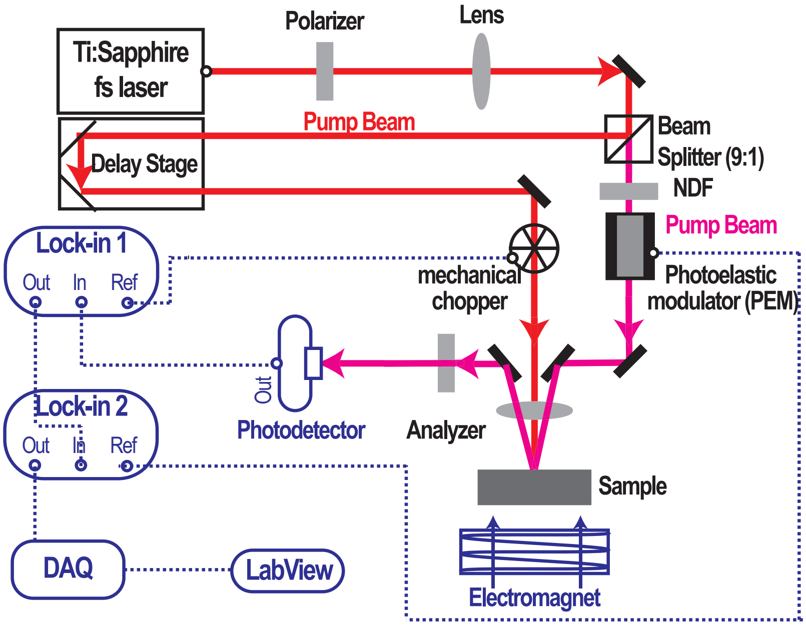

Figure 3.6: Schematic drawing of the time-resolved MOKE setup. A femtosecond laser pulse is divided into the pump pulse and the probe pulse using a beam splitter. The pump pulse is exposed to the sample surface, exciting the sample into a non-equilibrium state. The probe pulse is exposed to the same area on the sample surface, where the magnetization is measured using MOKE. By adjusting the time delay between the pump and probe pulses using the delay line, a complete pump-induced process could be obtained. A double modulation technique, using mechanical chopper and PET, in combination with two lock-in amplifiers, is employed to improve the SNR significantly.

and a lock-in amplifier is employed as a modulation method to further optimize the SNR. The PEM is placed between the polarizer and the sample. The principle of PEM is based on the photo-elastic effect, resulting in an oscillation of the light polarization. Meanwhile, the lock-in amplifier is used to eliminate other unwanted effect during the measurement, thus a much higher SNR can be expected. The lock-in amplifier is synchronized to the PEM's driving frequency or its second harmonic, facilitating the measurement on laser ellipticity and rotation, respectively.

3.3.4 Time-resolved magneto-optical Kerr (TR-MOKE) measurement

In the previous section, the static MOKE setup was discussed. In this section, the time-resolved MOKE setup is introduced, which is used to measure the ultrafast magnetization dynamics. The scheme of TR-MOKE is based on a typical concept in ultrafast optics, i.e., a pump-probe experiment. The illustration of the TR-MOKE setup is shown in Fig. 3.6.

Briefly speaking, a femtosecond laser pulse is divided into two parts using a beam splitter, which is called the pump pulse and the probe pulse, respectively. The pump pulse travels though a mechanic chopper, and is irradiated on the sample surface, exciting the sample into a non-equilibrium state. The chopper in combination with a lock-in amplifier is used as a modulation technique to enhance the measurement SNR[111]. The chopper periodically shutters the pump pulses at a certain frequency, which will be discussed below. After reflection, the pump pulse is blocked.

The response of the magnetization dynamics is measured in real time using a weaker probe pulse, which is focused on the same region of the pump spot on the sample surface. The working principle of the probe pulse is identical to the ordinary MOKE configuration discussed in previous section. The probe beam measures the magneto-optical response in the area excited by the pump pulse. The pump-induced dynamics is measured by adjusting the time delay between the pump and probe pulses. As the delay between the pump and the probe pulse is scanned continuously, a complete switching process could be obtained.

The delay-line is composed of a linear translation stage with a retroreflector, which is used to adjust the optical path length of the probe pulse. To improve the SNR of the detected signal, a second modulation technique using a PEM (with a modulation frequency at 50 kHz in this thesis) is employed. In this technique, a lock-in amplifier set at the same or double frequency of the PEM is used to measure the output voltage of the photodetector, which is used to measure the Kerr ellipticity (real part of the Kerr angle) and the Kerr rotation (imaginary part of the Kerr angle), respectively.

The measured MOKE signal oscillates between the pumped and un-pumped values at the frequency of the chopper. Another lock-in amplifier (set at the frequency of the chopper) measures the output of the first lock-in amplifier. In this way, the

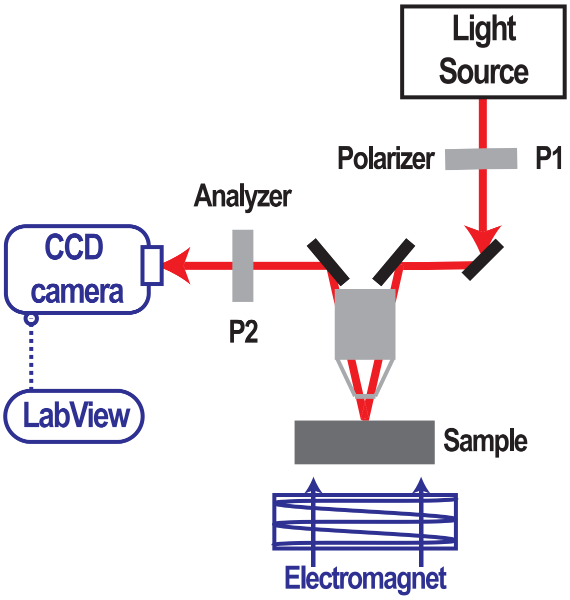

Figure 3.7: Schematic drawing of the Kerr microscope setup. The incident light, which is generated from a stable light source, travels through a focusing lens and the polarizer. Afterwards, the incident light is transmitted to an objective, which is set normal to the sample surface. The reflected beam passes the analyzer using crossed-polarizer configuration, thus a polar MOKE configuration is setup. A differential imaging processing technique is used to improve the quality of the Kerr images.

response of the magnetization induced by the pump beam will be measured with a significantly enhanced SNR.

3.3.5 Kerr microscopy

In the static MOKE described in the previous section, the response of magnetization is measured by sweeping the applied field, leading to a hysteresis loop of the sample. In other words, the detected MOKE signal in the entire laser probed area is averaged according to the spatial profile of the laser intensity. Another typical application based on MOKE is Kerr microscopy. This technique is also heavily used in this thesis to generate a spatially resolved image and observe magnetic domains directly.

Generally speaking, a Kerr microscope is an optical microscope employing MOKE to construct a spatially resolved Kerr contrast image, as illustrated in Fig. 3.7. In the setup, a stable light source with high intensity is employed to ensure a uniform high-quality Kerr image. The generation of the Kerr image is also based on polar MOKE, which is discussed in the previous section using a crossed-polarizer configuration. As the Kerr signal is relatively small, high-quality polarizer and analyzer with an extinction ratio of at least 10^{-4} are required.

The incident light first travels through a focusing lens and the polarizer, which holds a linear polarization with a narrow spot size. Then, the incident light is transmitted to an objective, which is set normal to the sample surface and detects the sample. Such a configuration results in a polar MOKE configuration that is most sensitive to the out-of-plane magnetization.

The objective determines the vision field area as well as the resolution of the Kerr microscope. That is to say, an objective with a low (high) magnification rate gives a large (small) vision field, thus a low (high) resolution. During the measurements, the optimal objective is determined according to the experimental requirement. Upon being reflected by the sample, the light travels back to the objective and beam splitter, whereafter it is filtered by the analyzer and captured by the monochromatic CCD camera. In this way, the spatially resolved magnetization response (i.e., the magnetic domain pattern) of the tested magnetic thin film sample is acquired in the form of Kerr contrast.

To improve the SNR and the Kerr contrast in the captured series of Kerr images, a differential imaging processing technique is required. Specifically, a background reference image is captured under a saturated magnetization prior to the measurement. The measured live Kerr image is subtracted by this background image to eliminate non-magnetic contributions and to optimize the SNR.

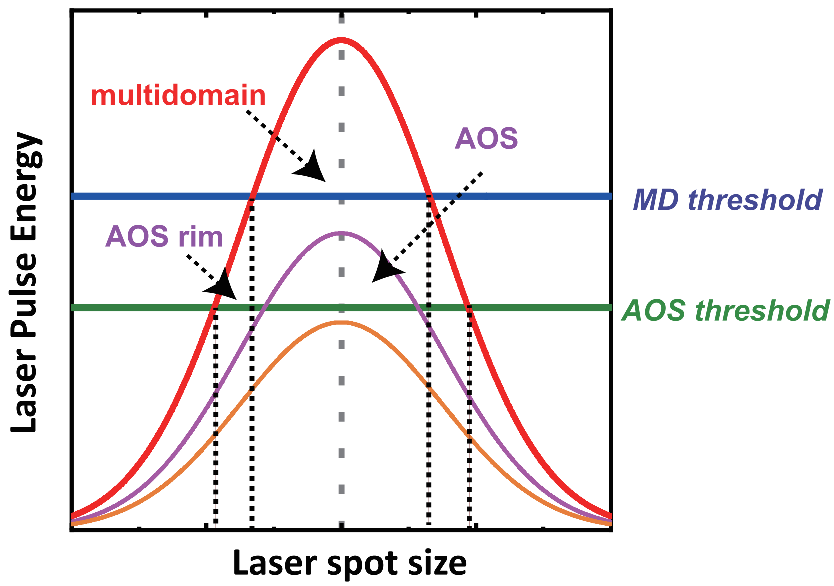

Figure 3.8: Illustration of the spatial Gaussian-shape laser pulses with different laser energies (E_p). Green line: AOS threshold energy (E_0). Blue line: multidomain threshold energy (E_{MD}). Above the E_0, the domain size increases with the E_p. For E_p higher than E_{MD}, a multidomain state is formed in the center area of the domain, whereas an AOS region is formed at the rim of the laser spot.

3.3.6 All-optical switching measurement setup

The AOS measurement setup is based on a Spectra Physics Spirit-NOPA laser system. The output laser pulses are linearly polarized, with a pulse duration of $<$ 100 fs, a central wavelength of 700 nm, a spot radius (1/e Gaussian pulse) typically of 25 µm, and a base repetition rate of 500 kHz. By using a pulse picker and a mechanical shutter, an individual laser pulse can be picked out.

In the measurements, which are performed at room temperature, the magnetization of the sample is first saturated by an external field. Afterwards, the field is turned off and the sample is exposed to subsequent laser pulses. After laser-pulse excitation, magneto-optical Kerr microscopy is used to study the magnetization response of the sample. The Kerr microscopy is performed in a steady state (i.e., long after laser excitation), where light and dark regions are corresponding to up and down magnetization direction, as described in Section 3.3.5.

The threshold fluence (F_0) describes the critical laser fluence needed for AOS.

Fig. 3.8 illustrates the spatial Gaussian-shape laser pulses with different laser energies (E_p). The green horizontal line indicates that a minimum E_p (termed as the AOS threshold energy, E_0) is required to enable AOS. Above E_0, the domain size (indicated by the length of the yellow line intersected with the laser pulse) increases with E_p, which is originated from the Gaussian shape of the laser pulse). As indicated by the blue horizontal line, in case of laser energy higher than the multidomain threshold energy (E_{MD}), a multidomain state is formed in the center area (indicated by the length of the blue line intersected with the laser pulse) of the domain, whereas an AOS region is formed at the rim of the laser spot, as indicated in Fig. 3.8. The F_0 is defined as E_0 divided by the area of the laser spot (using the FWHM of a Gaussian spot as the diameter).

Experimentally, F_0 is measured by the optically written domain size as a function of the laser pulse energy. In the measurement, the sample is exposed to single laser pulses with different E_p, whereafter the size of each domain is measured using Kerr microscopy. Based on the Liu's method[156], the relation between the domain size (D) and the F_0 is derived to be

$$\mathrm{D} = \pi r \sigma^2 \ln\left(\frac{P}{F_0 \pi r \sigma^2}\right) \tag{3.1}$$

where F_0 is the threshold fluence, and σ is the beam radius along the short axis (the laser spot is slight elliptical). r is the ratio between the long and short axis of the elliptical spot, which is measured form the Kerr microscopy data. As a result, F_0 is obtained by fitting the measurement data.

As to the AOS measurement performed on an MTJ device, the MTJ pillar is excited by subsequent fs laser pulses, meanwhile, the tunnel magnetoresistance is measured by a four-point TMR measurement in real time. The tunnel magnetoresistance measurement will be discussed in the following.

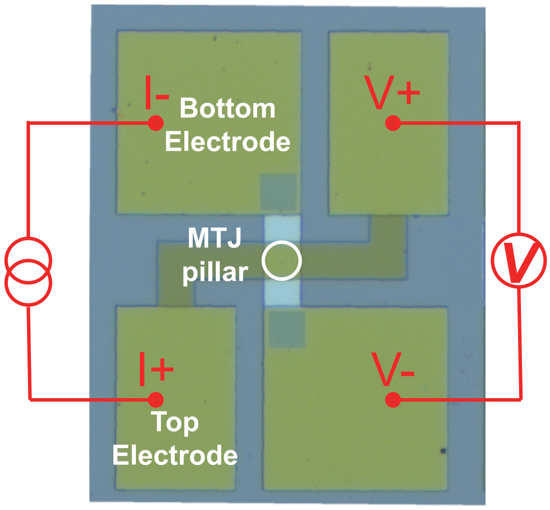

Figure 3.9: Schematic drawing of the four-point TMR measurement setup. The DC/AC current is sent through the MTJ from the top electrode to the bottom electrode. The voltage of the MTJ device is measured by a source-meter, thus the TMR of the device is obtained using Ohm's law. Alternatively, the output voltage can be measured using a lock-in amplifier, which is synchronized to the frequency of an AC current.

3.3.7 Tunnel magnetoresistance measurement setup

As described in Chapter 1, the TMR of an MTJ is determined by the relative magnetization orientation (i.e., parallel or antiparallel) of the two FM layers, leading to a bi-stable resistance state. The TMR measurement setup is based on a conventional four-probe resistance measurement technique, which is used to avoid experiment deviations due to the electrode resistance.

The schematic drawing of this magneto-electrical transport setup is shown in Fig. 3.9. In the setup, a current source (Keithley 6221) generates a DC current ($\approx$ 100 µA), which is sent through the MTJ in a CPP configuration, i.e., from the top electrode to the bottom electrode. The voltage of the MTJ device is measured by a source-meter (Keithley 2400), thus the TMR of the device is obtained using Ohm's law.

Alternatively, the output voltage can be measured using a lock-in amplifier (Stanford Research 830), which is used to eliminate noise during the measurement. The lock-in amplifier is synchronized to the AC current frequency that is generated by the current source. All the components in the setup are controlled by LabVIEW automatically.

4

Enhanced all-optical switching and domain wall velocity in annealed synthetic-ferrimagnetic multilayers

All-optical switching (AOS) of the magnetization in synthetic ferrimagnetic Pt/Co-/Gd stacks has received considerable interest due to its high potential towards integration with spintronic devices, such as magnetic tunnel junctions (MTJs), to enable ultrafast memory applications. Post-annealing is an essential process in the MTJ fabrication to obtain optimized tunnel magnetoresistance (TMR) ratio. However, with integrating AOS with an MTJ in prospect, the annealing effects on single-pulse AOS and domain wall (DW) dynamics in the Pt/Co/Gd stacks haven't been systematically investigated yet. In this study, we experimentally explore the annealing effect on AOS and field-induced DW motion in Pt/Co/Gd stacks. The results show that the threshold fluence (F_0) for AOS is reduced significantly as a function of annealing temperature (T_a) ranging from 100°C to 300°C. Specifically, a 28% reduction of F_0 can be observed upon annealing at 300°C, which is a critical T_a) for MTJ fabrication. Lastly, we also demonstrate a significant increase of the DW velocity in the creep regime upon annealing, which is attributed to annealing-induced Co/Gd interface intermixing. Our findings show that annealed Pt/Co/Gd system facilitates ultrafast and energy-efficient AOS, as well as enhanced DW velocity, which is highly suitable towards opto-spintronic memory applications. [*]

[*]This chapter has been published: **L. Wang**, Y. L. W. van Hees, R. Lavrijsen, W. Zhao, and B. Koopmans, "Enhanced all-optical switching and domain wall velocity in annealed synthetic-ferrimagnetic multilayers", *Applied Physics Letters* **117**, 022408 (2020)

4.1 Introduction

The emerging potential of integrating all-optical switching (AOS) of magnetization with spintronics devices for ultrafast and energy-efficient memory applications has been soon recognized after the first observation in ferrimagnetic GdFeCo alloys[8,94,98], such as employing it as part of the free layer of magnetic tunnel junctions (MTJs)[124,126]. Recently, it was demonstrated that efficient single-pulse AOS can be also realized in Pt/Co/Gd synthetic ferrimagnetic multilayers with perpendicular magnetic anisotropy (PMA)[128,132].

The AOS speed of both Pt/Co/Gd stacks and GdFeCo alloys is on the 100 fs time scale, which is 2 orders of magnitude faster than conventional switching mechanisms in MTJ that usually operate in sub-ns regime[157–159]. However, compared with GdFeCo alloys, Pt/Co/Gd multilayers show the flexibility in fabrication and interface engineering, as well as efficient field-driven domain wall (DW) velocity[135] and considerable built-in interfacial Dzyaloshinskii-Moriya interaction (iDMI)[129]. These interface-induced phenomena inherent to multilayered system are essential components for future ultra-high density memory applications[160–163]. Moreover, Co in direct contact with the MgO will increase the tunneling spin polarisation (TSP), leading to a high tunnel magnetoresistance (TMR). Consequently, integrating all-optical switchable Pt/Co/Gd stack with an MTJ is highly potential for ultrafast and ultra-high density opto-spintronic device application[7,113,135,164].

Typically, as to fabrication of MTJs with high TMR and thermal stability, it is well known that thermal annealing around 300°C after film deposition is an essential process[157,165]. However, with integrating Pt/Co/Gd with an MTJ in prospect, the effects of annealing on AOS and DW dynamics has not been studied yet. Although one might expect that annealing degrades the interface, and thereby reduce interface related properties like efficient AOS and DW motion as well, very recently, Beens *et al.*[166] theoretically predicted that Gd/Co interface intermixing strongly reduces AOS threshold fluence based on the extended microscopic three-temperature model (M3TM)[111]. Clearly, a systematic study of annealing effects is of utmost importance to further substantiate the applicability of the integration.

In this work, we experimentally demonstrate that single-pulse AOS is observed in Pt/Co/Gd stacks annealed up to 300°C. Moreover, annealing leads to a significant reduction of the switching threshold fluence. In addition, we show a strong increase of DW velocity in the creep regime upon increasing annealing temperature (T_a), while the iDMI constant reduces slightly.

4.2 Experimental results

The measurements are performed on Ta(4)/Pt(4)/Co(1)/Gd(3)/Pt(2) stacks (thickness in nanometer), which are deposited on Si:B substrate at room temperature (RT) using DC magnetron sputtering at 10^{-8} mbar base pressure. After deposition, the thin film stacks are annealed for 0.5 h with T_a ranging from 0°C to 400°C. Afterwards, the magnetization of the Pt/Co/Gd stacks are measured by a VSM-SQUID at RT, as a function of out-of-plane and in-plane applied magnetic field, respectively.

Fig. 4.1 (a) shows the out-of-plane magnetic hysteresis loops of the Pt/Co/Gd stacks annealed at T_a ranging from 0°C to 400°C. All these samples result in PMA, as indicated by the 100% remanence and the squareness of the hysteresis loops. Note that the coercive field (H_c) increases from 12.5 mT to 24 mT as T_a increases, as shown in Fig. 4.1 (b). The enhanced H_c may possibly originate from the intermixing at Co/Gd and Pt/Co interfaces, which becomes more prominent at higher T_a[167].

In addition, saturation magnetization (M_s) shows a significant reduction upon annealing, as also shown in Fig. 4.1 (b). The reduced M_s in this synthetic ferrimagnetic system may originate from annealing-induced interface intermixing. More specifically, although the Curie temperature for bulk Gd is slightly lower than RT, it is elevated at the Co interface due to the presence of the antiferromagnetic (AF) coupling[128]. Upon annealing, intermixing may lead to a reduction of M_s in the synthetic ferrimagnetic multilayer as T_a rises[167], which explains a gradual reduction of the net magnetization as a function of T_a.

To investigate the annealing effects on PMA, we plot the anisotropy field (H_k)

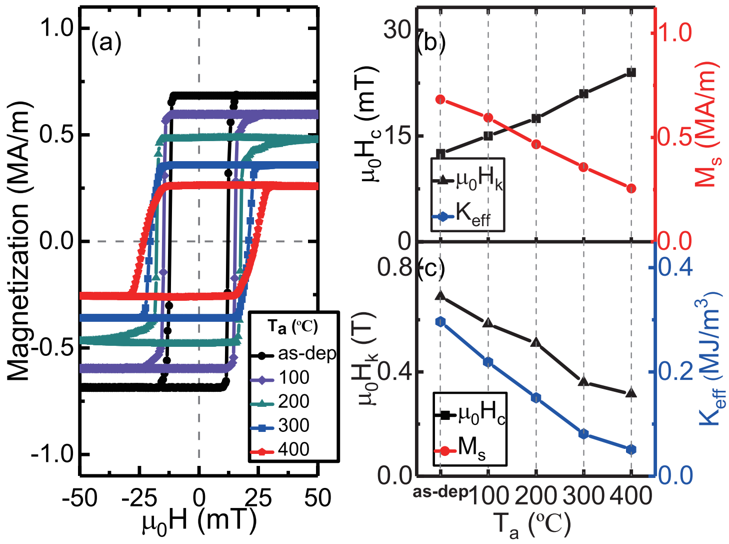

Figure 4.1: (a) Hysteresis loops with out-of-plane magnetic field for the annealed Pt/Co/Gd stacks. (b) Coercive field (black cubes) and saturation magnetization (red dots) as a function of T_a. (c) Anisotropy field (black triangles) and effective anisotropy (blue hexagons) as a function of T_a.

and the effective anisotropy (K_{eff}) as a function of T_a) in Fig. 4.1 (c), where H_k is determined from the hard-axis loops, and K_{eff} is calculated from $\frac{1}{2}\mu_0 M_s H_k$. We observe that H_k and K_{eff} show a gradual reduction as T_a) increases. Moreover, annealing at 400°C results in poor PMA. These results indicate that annealing leads to a significant degradation of the PMA in the Pt/Co/Gd stacks, which is consistent with the previous studies that annealing deteriorates PMA in Pt/Co system[167,168].

Next, to further verify the AF exchange interaction between the Co layer and the Gd layer of the annealed Pt/Co/Gd stacks , the moment per unit area is measured as a function of temperature from 350 K to 5 K by using VSM-SQUID. As shown in Fig. 4.2, all the samples show AF coupling by the presence of a compensation temperature (T_{comp}) ranging from 120 K to 200 K, at which the magnetic moment of Co (m_{Co}) and the magnetic moment of Gd (m_{Gd}) compensate each other. Above T_{comp}, the net magnetic moment equals to $m_{Co} - m_{Gd}$. Indeed, T_{comp} shows an increasing trend from 120 K to 200 K upon higher T_a, as shown in the inset of Fig. 4.2.

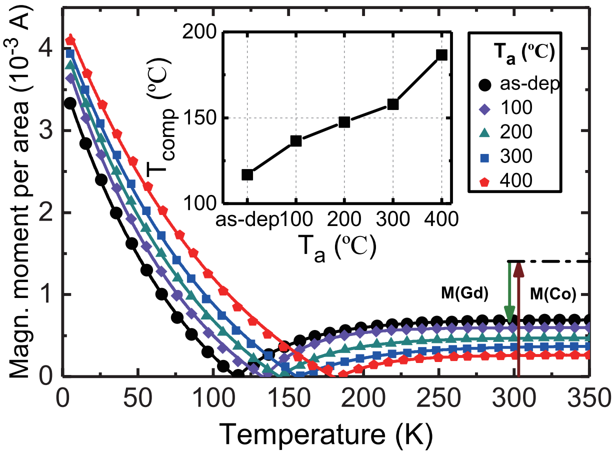

Figure 4.2: VSM-SQUID measurements of the magnetic moment per unit area as a function of T_a) for the annealed Pt/Co/Gd stacks. Inset: compensation temperature (T_{comp}) as a function of T_a.

The increased T_{comp} is in agreement with previous studies on Co/Gd multilayers[167], and may originate from the modification of the exchange interaction at Co/Gd interface, resulting from annealing-induced intermixing. Notably, a gradual reduction of M_s at RT is also observed, which is also evidenced in Fig. 4.1 (b). To quantitatively explain the reduction of M_s, the thickness of fully magnetized Gd layer at RT is estimated by using the data in Fig. 4.2. The analysis, presented in Section 4.3, shows that a larger thickness of 0.56 nm equivalent of fully magnetized Gd layer at RT is formed upon annealing at 300°C, whereas we find that only 0.43 nm for the as-dep sample (in reasonable agreement with our previous work[128]). These results confirm the reduction of M_s in Pt/Co/Gd synthetic ferrimagnetic stacks.

Afterwards, we investigate annealing effect on single-pulse AOS in the annealed Pt/Co/Gd stacks. In the measurements, the samples are first saturated by an external magnetic field, afterwards, they are exposed to a number of consecutive laser pulses ranging from 1 to 5 pulses with a single-pulse energy of 400 nJ.The laser pulse is linearly-polarized, with a pulse duration of ≈100 fs, a spot size of typically 100 μm and a wavelength of 700 nm. The responses of magnetization after laser excitation are measured by magneto-optical Kerr microscopy, where light and dark regions are corresponding to up and down magnetization direction.

Fig. 4.3 (a)shows the typical AOS measurements performed on samples annealed at 300°C (see Section 4.3 for measurements on different T_a) . For samples annealed below 400°C, a homogeneous domain with an opposite magnetization direction is written for every odd number of laser pulses, whereas no net magnetization reversal is observed for every even number of pulses. This behavior is consistent with the thermal single-pulse AOS mechanism discussed in previous studies[113,132], in which the laser induced switching is driven by transferring the angular momentum mediated by exchange scattering between the Gd and the Co sublattices[132].

In contrast, upon annealing at 400°C, only a multidomain state is created after any arbitrary number of pulses, as shown in Fig. 4.3 (b).These results indicates that the critical T_a for AOS in Pt/Co/Gd stacks must be in the range of 300°C - 400°C. Such a high T_a tolerance up to at least 300°C is promising for fabricating integrated opto-spintronic MTJ devices, since a post-annealing process at 300°C is generally required to improve TMR and thermal stability of the MTJ[157,165].

To investigate annealing dependence on the AOS energy efficiency, we systematically investigate the threshold fluence as a function of T_a in the Pt/Co/Gd stacks. In the measurements, the samples are exposed to single laser pulses with different laser energies. Afterwards, the pulse energy dependence of the AOS written domain size is measured by Kerr microscopy (see Section 4.3) and plotted in Fig. 4.3 (c). In case of annealing below 400°C, the threshold laser energy (P_0) of AOS in the measurements decreases gradually upon annealing. Specifically, compared to $P_0 = 270$ nJ for the as-dep sample, it reduces to 150 nJ upon annealing at 300°C. The threshold fluence for AOS (F_0) can be extracted by assuming a Gaussian shape of the laser pulse (inset of Fig. 4.3 (c)). A significant annealing dependence of F_0 is observed, decreasing for higher T_a. Note that in the case of annealing at 400°C, although no homogenous AOS domain is created for all pulse energies, threshold fluence for multidomain state still decreases, as shown in the open dot in Fig. 4.3 (c).

We also observe that the minimum F_0 for homogenous AOS of 1.09 mJ/cm^2 is

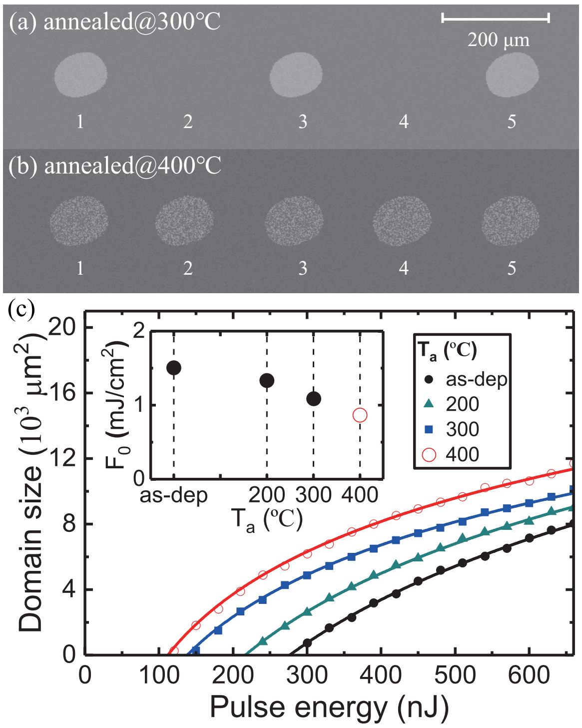

Figure 4.3: (a)-(b) AOS toggle switching measurements performed on annealed Pt/Co/Gd stacks annealing 300°C and 400°C, respectively. (c) AOS domain size as a function of laser pulse energy for the annealed Pt/Co/Gd stacks. Inset: AOS threshold fluence as a function of annealing temperature for Pt/Co/Gd stacks.

achieved upon annealing at 300°C, 28% lower than the F_0 found for as-dep sample. Moreover, the F_0 for annealed Pt/Co/Gd stacks is significantly lower than F_0 for GdFeCo alloys[8]. This adds to the advantage of Pt/Co/Gd stacks of being more suitable for integrating with spintronics as it allows for interface engineering to be used.

The above results are consistent with recent theoretical work by Beens *et al.*[166] using the extended microscopic three-temperature model (M3TM)[111], where it was demonstrated that Co/Gd interface intermixing leads to a significant reduction of F_0 in synthetic ferrimagnetic multilayers, this effect can be traced down to a combination of more efficient exchange scattering and reduction of the thin film's Curie temperature. In our present work, annealing leads to strong Co/Gd intermixing, which results in a decrease of F_0 with higher T_a.

We then investigate annealing effects on DW dynamics and DMI in Pt/Co/Gd stacks. Previous studies[128,129] reported that Pt/Co/Gd stacks exhibit efficient field-driven DW motion and considerable DMI value, which are highly promising for integrating AOS with DW devices[102,169,170] or skyrmion-electronics[160,171]. Fig. 4.4 (a) shows the typical measurements of DW velocity, which is extracted from the average expansion of a bubble domain under an out-of-plane magnetic field pulse (H_z) with a pulse duration ranging from 10 μs to 1000 μs. The breaking of radial symmetry in the measurement originates from the presence of an effective iDMI field. In Fig. 4.4 (b), the DW velocity as a function of $\mu_0 H_z$ for all T_a is plotted on a logarithmic scale according to the universal creep law[172],

$$v = v(H_{dep}) \exp\left[-\frac{U_C}{k_B T}\left(\left(\frac{H_{dep}}{H_Z}\right)^{\mu} - 1\right)\right] \tag{4.1}$$

where U_c is the scaling energy constant, k_B is the Boltzmann constant, T is the temperature, H_{dep} is the depinning field at 0 K, and $\mu = 1/4$ is the critical exponent for a 2D system (see Section 4.3). Remarkably, a significant enhancement of DW velocity in the creep regime is observed upon increasing T_a. In this creep regime, the DW velocity is mainly determined by the pinning of DW resulting from structural defects in the ultrathin film system. To explain the enhancement of DW velocity, the pinning potential (P)

$$P = \left(\frac{U_C}{k_B T}\right) H_{dep}^{\mu} \tag{4.2}$$

as a function of T_a is plotted in Fig. 4.4 (c). The pinning potential, which is correlated with the linear slope in Fig. 4.4 (b), shows a progressive reduction when increasing T_a . This reduction may be due to annealing-induced intermixing at the Co/Gd interface, which results in the significant enhancement of the DW velocity.

Finally, to investigate the variation of iDMI in Pt/Co/Gd stacks upon annealing, the DMI effective field ($\mu_0 H_{DMI}$) is measured by asymmetric domain bubble expansion under $\mu_0 H_z$ as a function of in-plane magnetic field ($\mu_0 H_x$). Fig. 4.5

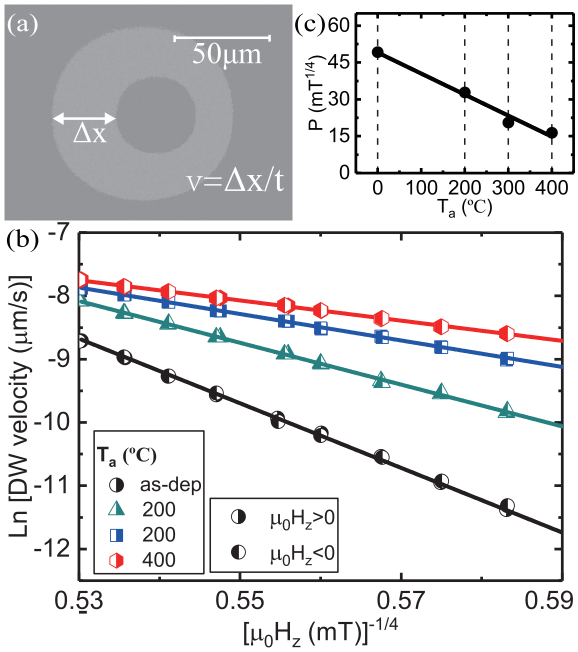

Figure 4.4: (a) Typical differential Kerr image for DW velocity measurement for annealed Pt/Co/Gd stack (b) DW velocity as a function of out-of-plane magnetic field pulse $\mu_0 H_z^{-1/4}$. (c) Pinning potential as a function of annealing temperature for Pt/Co/Gd stacks.

(a-b) show the typical differential Kerr images under an in-plane field of ±340 mT. Notably, the asymmetry of DW expansion along the x axis in the measurements is due to the interplay between the internal $\mu_0 H_{DMI}$ and the external $\mu_0 H_x$, from which $\mu_0 H_{DMI}$ can be estimated by $\mu_0 H_x$ corresponding to the slowest DW speed (see Section 4.3).

Fig. 4.5 (c) shows $\mu_0 H_{DMI}$ as a function of T_a in Pt/Co/Gd stacks, where a slight decrease is observed upon annealing. Specifically, $\mu_0 H_{DMI}$ for as-dep samples is around 300 mT, whereas $\mu_0 H_{DMI}$ for the sample annealed at 300°C reduces to 250 mT. The DMI constant D is then deduced from $\mu_0 H_{DMI} = D/M_s\sqrt{A/K_{eff}}$, where A is the exchange stiffness constant of 16 pJ/m taken from literature[129] and assumed to be constant for all samples. Note that a DMI constant of 1.1 mJ/m^2 is observed for the as-dep Pt/Co/Gd stack, which is in reasonable agreement with previous reports. In addition, although D shows a decreasing trend with $\mu_0 H_{DMI}$ when increasing of T_a (shown in Fig. 4.5 (c)), a considerable D value of 0.75 mJ/m^2

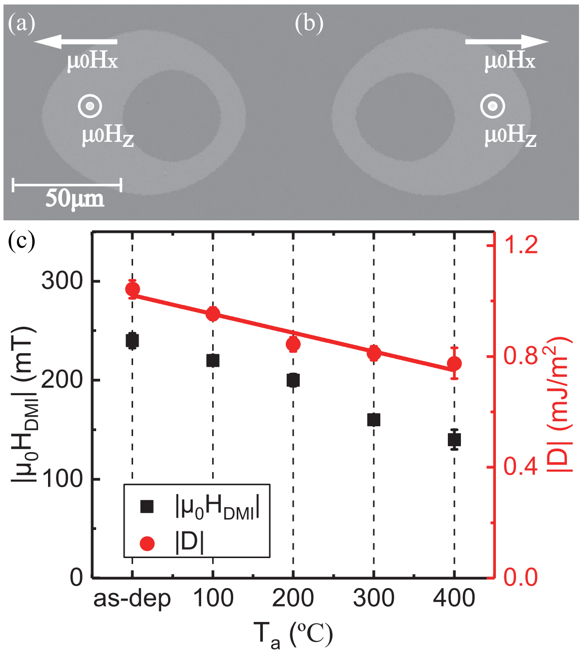

Figure 4.5: (a)-(b). Typical differential Kerr images for iDMI measurement for the annealed Pt/Co/Gd stacks. (c) effective DMI field ($\mu_0 H_{DMI}$) (black cubes) and DMI constant (D) (red dots) of the annealed Pt/Co/Gd stacks as a function of T_a.

is still observed for 300°C annealing. Like the trends in AOS and DW velocities, the results on iDMI could well be explained by annealing-induced intermixing at the Pt/Co and Co/Gd interfaces, which leads to subtle changes of the exchange interaction between the atoms near interfaces.

4.3 Supplemental information

Analysis of the SQUID-VSM measurement on the annealed Pt/Co/Gd stack

To quantitatively analyze the annealing effect on the reduction of M_s in Pt/Co/Gd stacks from a synthetic ferrimagnet viewpoint, the equivalent thickness of the fully magnetized Gd layer as a function of T_a at room temperature can be extracted from the data in the Fig. 4.2.

The detailed estimation process is as follows, which is the same method as used in a previous study[128]. In case of T_a = 300°C, a magnetic moment per unit area of 4.22 MA/m at 0 K can be extrapolated from Fig. 4.2. By using the magnetization

Table 4.1: The thickness of proximity induced fully magnetized Gd layer at room temperature ($t_{Magn.Gd}$) as a function of T_a. An enhancement of $t_{Magn.Gd}$ upon higher T_a indicating a possible explanation for the reduction of M_s.

T_a	$t_{Magn.Gd}$
0	0.43
100	0.45
200	0.51
300	0.56
400	0.59

of 1.4 MA/m for bulk Co, 1 nm Co layer results in the magnetic moment per unit area of 1.4 Am (as indicated as red arrow in Fig. 4.2). Due to the antiferromagnetic coupling of the Co and Gd sublattices, this leaves a magnetic moment per unit area of 5.62 Am for the Gd film.

This value corresponds to a magnetization of 1.87 MA/m for 3 nm Gd layer, which is consistent with the magnetization of bulk Gd. At room temperature (300 K), a magnetic moment per unit area of 0.36 Am is measured. Above t_{comp}, this value equals to the moment of the Co minus that of the Gd. By using the moment per unit area of 1 nm Co layer, a magnetic moment per unit area of 1.04 Am for the Gd layer can be obtained. Using the magnetization for the Gd layer, the value of 1.04 Am corresponds to 0.56 nm of fully saturated Gd, which is in the same order as found in previous studies.

Based on this method, the thickness of fully magnetized Gd layer at room temperature ($t_{Magn.Gd}$) as a function of T_a can be determined and is shown in Table S1. We observe an enhancement of $t_{Magn.Gd}$ upon higher T_a. More specifically, compared with 0.43 nm for as-dep sample, $t_{Magn.Gd}$ increased to 0.56 nm in case of T_a =300°C. Due to the antiferromagnetic coupling between the Co and the Gd layer, the increased $t_{Magn.Gd}$ leads to a reduction of net moment per unit area at room temperature.

This estimation demonstrates a possible explanation for the reduction of M_s as found in our experiment on annealed Pt/Co/Gd stacks. This result is also consistent with previous studies on Gd/Co multilayers. However, it is worth noting that other annealing induced interface phenomena, such as alloying and increase of interface roughness at Co/Gd interface are also crucial factors during annealing. Under the joint effects of all these annealing-induced interface related mechanisms, the modification of magnetic properties in Pt/Co/Gd stacks eventually result in the reduction of M_s observed in our experiment.

This estimation demonstrates a possible explanation for the reduction of M_s as found in our experiment on annealed Pt/Co/Gd stacks. This result is also consistent with previous studies on Gd/Co multilayers[167]. However, it is worth noting that other annealing induced interface phenomena, such as alloying and increase of interface roughness at Co/Gd interface are also crucial factors during annealing. Under the joint effects of all these annealing-induced interface related mechanisms, the modification of magnetic properties in Pt/Co/Gd stacks eventually result in the reduction of M_s observed in our experiment.

Single-pulse toggle AOS measurement for the annealed Pt/Co/Gd stacks

In Section 4.2, we investigate annealing effects on AOS toggle switching for Pt/Co-/Gd stacks. The consecutive laser pulses measurement up to 10 laser pulses is performed at T_a = 0, 200°C, 300°C, 400°C, respectively, as shown in Fig. 4.6.

In case of $T_a \leq 300$°C, a homogeneous domain with an opposite magnetization direction is written for every odd number of laser pulses, whereas no net magnetization reversal is observed for every even number of pulses. These results demonstrate that each next laser pulse completely reverses the domain created by a previous sequence of AOS events. The observed switching behavior is consistent with previous studies on the thermal single-pulse switching mechanism.

In case of $T_a = 400$°C, the absence of single-pulse AOS demonstrates that exceeding an annealing temperature higher than 300°C leads to the loss of single-pulse AOS behavior in Pt/Co/Gd, which is discussed in more detail in Section 4.2. These results indicate that the threshold T_a for single-pulse AOS in Pt/Co/Gd

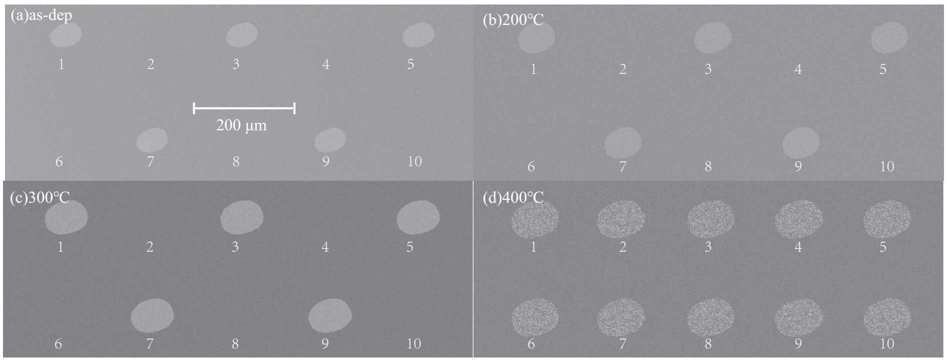

Figure 4.6: AOS toggle switching measurements performed on annealed Pt/Co/Gd stacks after annealing for 0.5 h at 0, 200°C, 300°C and 400°C, respectively. The number of laser spots are indicated in the figure, up to 10 consecutive laser pulses. We observe single pulse toggle switching upon $T_a \leq 300$°C. However, in case of $T_a = 400$°C, a multidomain state is created for any arbitrary number of pulses.

stacks is above 300°C, which is a crucial temperature for MTJ post-annealing process.

Pulse-energy dependent AOS measurement on the annealed Pt/Co/Gd stack

In Section 4.2, we investigate annealing effects on AOS threshold fluence for Pt/Co/Gd stacks. The threshold fluence is determined by pulse-energy dependent measurements, as shown in Fig. 4.7. The size of domains and its dependence on laser energy is calculated and analyzed in Fig. 4.3 (c).

Fig. 4.7 (a)–(c) show that, in case of $T_a \leq 300$°C, a homogenous domain is created after the laser excitation, as found in previous work. Moreover, the threshold laser energy P_0 decreases from 300 nJ for as-dep sample to 150 nJ upon $T_a =$ 300°C. These results show that the energy efficiency of AOS in Pt/Co/Gd stacks is enhanced upon annealing in the range of 0 – 300°C. However, in case of $T_a =$ 400°C, a multidomain state can be written from P_0 at 120 nJ and up, showing that exceeding T_a can lead to substantial change of AOS inherent to annealed Pt/Co/Gd stacks (discussed in Section 4.2).

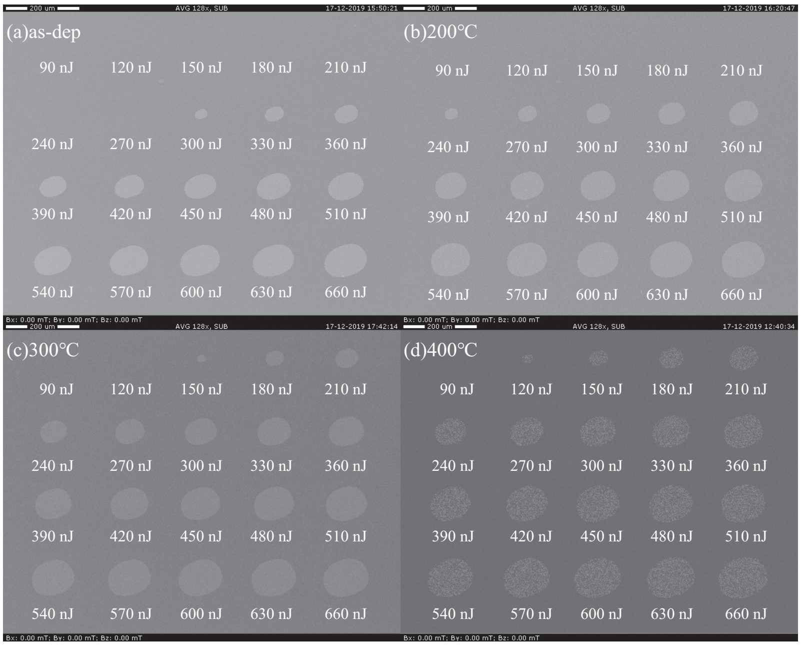

Figure 4.7: Kerr microscope image of the pulse-energy dependence of domain size measurements performed on the Pt/Co/Gd stacks annealed at different T_a. Laser pulse energies are indicated in the figure. The results show that in case of $T_a \leq 300°C$, a decreasing threshold laser energy is observed upon higher T_a, while in case of $T_a = 400°C$, a multidomain state is created for all pulse energies from the threshold laser energy.

DW velocity as a function of magnetic field pulse of the annealed Pt/Co/Gd stacks

To investigate annealing effects on field-driven DW velocity in the creep regime, Fig. 4.8 plots the DW velocity on a linear scale as a function of out-of-plane magnetic field pulse ($\mu_0 H_z$) for both directions ($\mu_0 H_z < 0$ and $\mu_0 H_z > 0$, respectively), for Pt/Co/Gd stacks annealed at 0, 200°C, 300°C, 400°C, respectively. In the figure, a significant enhancement of DW velocity in the creep regime upon annealing can be observed directly.

Determination of the DMI effective field for annealed Pt/Co/Gd stacks

To investigate the variation of the DMI effective field ($\mu_0 H_{DMI}$) upon annealing, asymmetric bubble-domain expansion measurements are performed on Pt/Co/Gd annealed stacks. In the measurements, the DW motion is driven by an out-of-

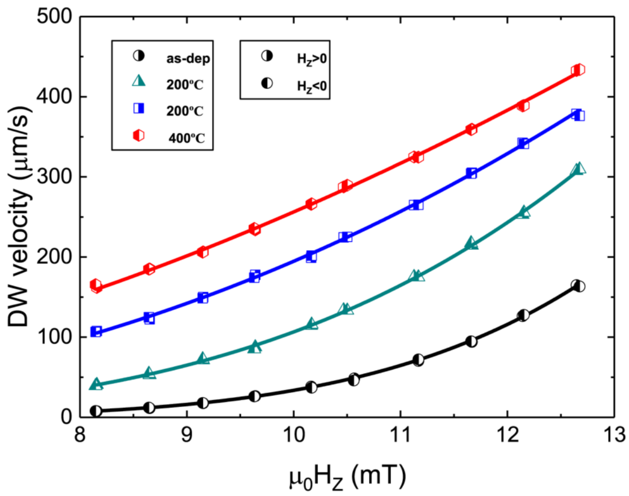

Figure 4.8: Domain wall velocity as a function of out-of-plane magnetic field pulse ($\mu_0 H_z$) for Pt/Co/Gd stacks with different T_a (plotted in normal scale).

plane magnetic field pulse $\mu_0 H_z$ with both directions (as indicated in red and black cubes for $\mu_0 H_z < 0$ and $\mu_0 H_z > 0$, respectively) as a function of in-plane magnetic field ($\mu_0 H_x$). Since the asymmetry of DW expansion along the x axis in the measurements is due to the interplay between the internal $\mu_0 H_{DMI}$ and the external $\mu_0 H_x$, the effective DMI field can be estimated by $\mu_0 H_x$ corresponding to the slowest DW speed[129].

Fig. 4.9 shows the result of the asymmetric bubble-domain expansion measurement performed on Pt/Co/Gd stack annealed at 0, 200°C, 300°C,400°C, respectively. Examining the domain wall velocity as a function of the $\mu_0 H_x$, the DMI effective field corresponding to the slowest DW velocity is determined by fitting the parabola, as indicated by the vertical dashed lines in the figure. These results constitute Fig. 4.5 (c).

4.4 Conclusion

In conclusion, we have experimentally demonstrated enhancing AOS and DW velocity through annealing in synthetic ferrimagnetic Pt/Co/Gd stacks. Notably, toggle switching behavior is observed upon annealing up to 300°C, which is essential for the integration with MTJ devices due to the required post-annealing

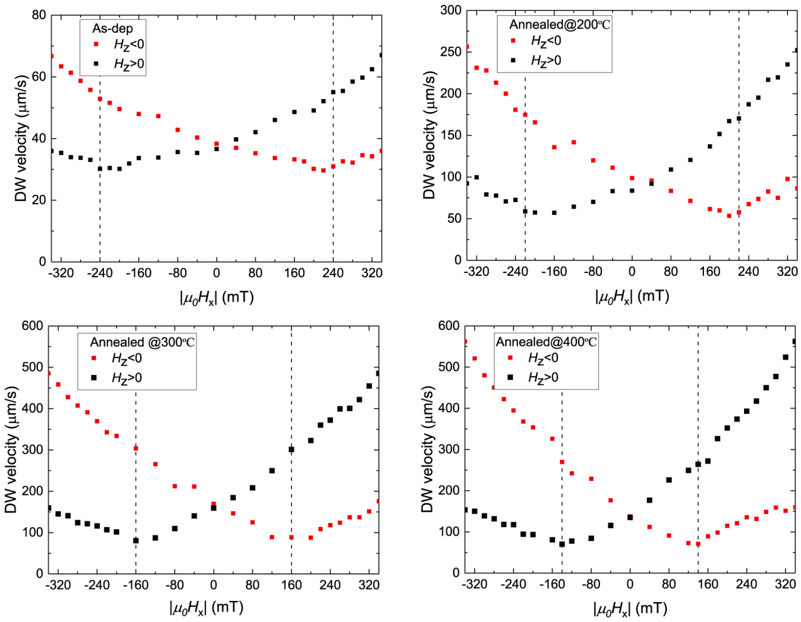

Figure 4.9: Domain wall velocity under out-of-plane magnetic field pulse ($\mu_0 H_z$) as a function of in-plane magnetic field ($\mu_0 H_x$) for Pt/Co/Gd stacks annealed at 0, 200°C,300°C, 400°C, respectively.

process. Moreover, the AOS threshold fluence reduces significantly upon annealing, which indicates an enhancement of AOS energy efficiency for data writing.

In addition, a significantly enhancement of DW velocity upon annealing is also observed, which is in accordance with a reduction of the DW pinning potential at the Co/Gd interface. Lastly, a considerable DMI value is observed for samples annealing up to 300°C. Therefore, our results demonstrate that the synthetic ferrimagnetic Pt/Co/Gd stack is an ideal candidate for integrating AOS in spintronic devices, such as MTJs or magnetic DW devices, which may pave the way towards ultrafast and energy efficient opto-spintronics memory application.

5

Femtosecond Laser-Assisted Switching in Perpendicular Magnetic Tunnel Junctions With Double-Interface Free Layer

Perpendicular MTJs with double-interface free layer (p-DMTJs), which exhibit enhanced TMR and Δ at the nanoscale, have received considerable interest as building blocks for spintronic data storage devices. The HAMR technique have been widely employed in mainstream magnetic storage to enable ultrahigh storage density. However, the data access is achieved by sensing the stray field of the selected magnetic element using a mechanical "read head," resulting in an unfavourable speed limitation and design complexity. To address this issue, we experimentally explored fs laser-assisted switching in a p-DMTJ device using a direct electrical TMR readout. We demonstrate two reconfigurable switching operations, i.e., binary "write" and unidirectional "reset," by the interplay of the fs laser and synchronized magnetic field sequence. We further explored the joint effect, and a switching phase diagram was obtained. The effect of the stray field of p-DMTJ, as well as laser helicity, on switching is also discussed. Results show the feasibility of fs laser-assisted writing p-DMTJs, which can pave the way in high-density optospintronic storage applications.[*]

[*]This chapter has been accepted for publication: **L. Wang**, W. Cai, K. Cao, K. Shi, B. Koopmans, and W. Zhao, "Femtosecond Laser-Assisted Switching in Perpendicular Magnetic Tunnel Junctions with Double-Interface Free Layer", *Science China Information Sciences* (2021)

5.1 Introduction

The emerging potentials of magnetic tunnel junctions (MTJs) as building blocks for next-generation spintronic data storage devices have attracted significant attention owing to their nonvolatility and high scalability[3–5,52,171,173,174]. CoFeB/MgO-based MTJs with perpendicular magnetic easy axis (p-MTJs), where perpendicular magnetic anisotropy (PMA) originates at the CoFeB/MgO interface[158], have high thermal stability (Δ) for nanoscale devices, high tunnel magnetoresistance ratio (TMR), and low power consumption simultaneously[66,159,175]. Recently, it was reported that TMR and Δ can be further increased in p-MTJs using a MgO/CoFeB/W/CoFeB /MgO double-interface free layer (FL) structure (p-DMTJs)[157,176] with atom-thick W spacer and bridging layers[177–179]. This offers a suitable candidate to facilitate high-performance spintronic data storage[180].

As to mainstream magnetic storage, such as hard disc drives, heat-assisted magnetic recording (HAMR) techniques have been widely employed to enhance storage density[19,181]. In an HAMR device, switching is assisted by the local laser heating of the magnetic element, which momentarily lowers its coercive field. Moreover, a reduced magnetic field is generated by the "write head" to set the magnetization direction. Nevertheless, as to data access, a mechanical "read head" is always required to sense the stray field or magnetic–optical contrast of the selected magnetic element, which results in an unfavorable access delay and design complexity.

To address this issue, integrating heat-assisted switching with MTJs has been considerably investigated in spintronic R&D[182], such as thermally-assisted switching (TAS) schemes[73,74]. By circulating current in write lines, Joule heating has been used to assist the switching of specially designed in-plane MTJs while a reduced magnetic field is applied. However, current-induced Joule heating unavoidably results in drastic energy dissipation and heat-up delay. For future high-density spintronic storage[7,135], the fs laser-assisted switching of a high-performance p-DMTJ has not yet been proposed. The effect of additional magnetic FLs on the switching process has not been clarified. Moreover, no systematic study has been reported on the joint effect of laser and synchronized magnetic field.

In this work, we experimentally investigated fs laser-assisted switching in a high-performance p-DMTJ device, which was read out directly through a real-time electrical TMR measurement. Using an fs laser pulse train and a synchronized magnetic field sequence, reconfigurable switching operations, such as the toggle "write" and unidirectional "reset," were investigated. The synergy between the fs laser pulses and magnetic field sequence was further investigated, and a switching phase diagram was obtained. Finally, the effect of the stray field of p-DMTJ, as well as laser helicity, on switching is discussed.

5.2 Experimental results

5.2.1 Device characterization

Figure 5.1 (a) shows a magnetic thin film of the p-DMTJ used in this study. This film comprises, from the substrate side upwards, Ta (3)/Ru (20)/Ta (0.7)/[Co (0.5)/Pt (0.35)]$_6$/Co (0.6)/Ru (0.8)/Co (0.6)/[Pt (0.35)/Co (0.5)]$_3$/W (0.25)/CoFeB (0.9)/MgO (0.8)/CoFeB (1.2)/W (0.3)/CoFeB (0.5)/MgO (0.8)/Pt (1.5), deposited on a thermally oxidized Si (001) substrate at room temperature (30°C) through Singulus DC and RF magnetron sputtering (numbers in parentheses denote the thicknesses of each layer in nanometers, and the subscripts for Co/Pt multilayers are the numbers of repeat).

The composition of the CoFeB target was $Co_{20}Fe_{60}B_{20}$ (in atomic %). The Ta/Ru/-Ta layer was used as the bottom electrode. The bottom $(Co/Pt)_m$ and top $(Co/Pt)_n$ multilayers, with the CoFeB layer, were antiferromagnetically coupled through a thin Ru layer, forming a synthetic antiferromagnetic (SAF) reference layer. The MgO layer was the tunnel barrier. For the FL, the bottom and top CoFeB layers were ferromagnetically coupled with a 0.3-nm W spacer layer. The double-FL structure was employed to enhance Δ while maintaining the writing energy efficiency. After deposition, the stacks were annealed at 400°C in a vacuum for 1 h to enhance PMA.

We investigated the magnetic characteristics of the full-sheet MTJ stack using physical properties measurement system-vibrating sample magnetometer (PPMS-

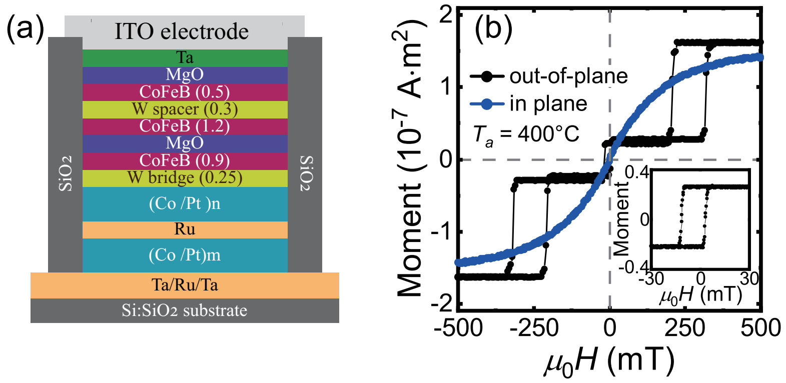

Figure 5.1: MTJ stack structure and magnetic characteristics. (a) Schematic of the p-DMTJ stack structure. Ta/Ru/Ta is the bottom electrode. The bottom $(Co/Pt)_m$ and top $(Co/Pt)_n$ with the CoFeB layer were antiferromagnetically coupled with a thin Ru layer to form a synthetic antiferromagnetic (SAF) reference layer. The MgO layer is the tunnel barrier. The double-free-layer structure (CoFeB/W/CoFeB/MgO) with an atom-thick W spacer was used. (b) M-H hysteresis loops measured as a function of out-of-plane (black) and in-plane (blue) applied magnetic field at room temperature using PPMS-VSM. The film exhibited strong PMA in both the free and reference layers. Inset: Out-of-plane M-H minor loop of the p-DMTJ stack.

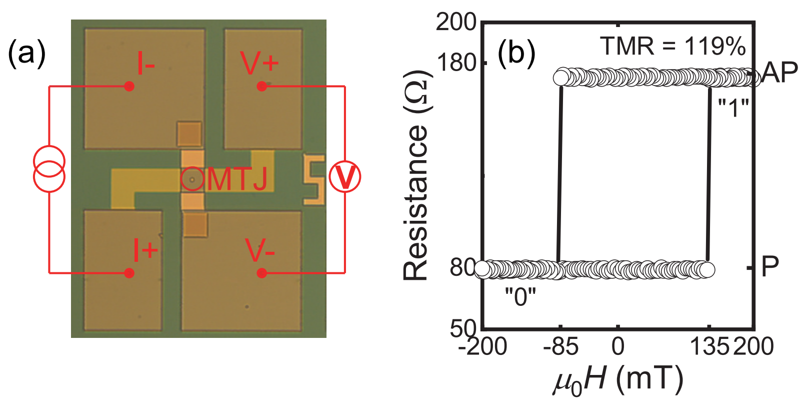

Figure 5.2: Characterization of the fabricated p-DMTJ device. (a) Optical microscope image of the p-DMTJ device. Circular MTJ pillars were fabricated using multistep optical lithography and Ar ion milling. The diameter of the MTJ pillar was 5 µm, with four electrode pads to perform TMR detection. A 100-nm-thick indium tin oxide (ITO) film was employed as the transparent top electrode, enabling both efficient optical access and electrical detection. (b) R-H magnetoresistance loop measured as a function of applied out-of-plane magnetic field ranging from -200 to $+200$ mT. The result shows that the double-free layers simultaneously switched, and the TMR ratio was calculated to be 119%.

VSM) at room temperature (30°C). Figure 5.1 (b) shows the M-H hysteresis loops of the p-MTJ film, i.e., without the device fabrication, as a function of the out-of-plane (black) and in-plane (blue) applied magnetic field. The film exhibits that strong PMA was present in both the free and reference layers, as indicated by the 100% remanence and squareness of the major hysteresis loops.

According to the minor loop (inset of Figure 5.1 (b)), the two CoFeB FLs simultaneously switched due to the ferromagnetic coupling from the atom-thick W layer, which is critical for the p-DMTJ performance. As reported in our previous work[157], the enhanced annealing endurance, up to 400°C, originates from reduced atom diffusion when a W bridging and spacer layer is used. This improves the crystalline quality of the MgO layer and bcc texture of the CoFeB layers, resulting in high TMR.

Note that the loop shift was relatively small for the full-sheet sample (~ -3 mT), indicating a significant reduction in the stray field attributed to the SAF reference layer. A coercive field of 7 mT was achieved. The anisotropy field was determined from the hard-axis loops by sweeping the in-plane field, and it was found to be as large as 300 mT. These results are consistent with those of previous studies on similar double-FL p-DMTJ stacks.

Furthermore, the full films were used to fabricate circular MTJ pillars using multistep optical lithography and Ar ion milling. A 100-nm-thick ITO layer was used as the transparent top electrode through electron beam evaporation, which allows both efficient optical access and high signal-noise-ratio electrical detection. Because the transparency and electrical conductivity of ITO are significantly dependent on deposition conditions, the deposition process was carefully optimized before the MTJ fabrication, which is a crucial step in laser-assisted switching measurements. Figure 5.2 (a) shows the optical microscope image of the fabricated MTJ devices with a pillar diameter of 5 µm and four electrode pads for TMR detection.

After fabrication, TMR measurements were performed on the patterned MTJ device by sweeping an out-of-plane magnetic field ranging from -200 to $+200$

mT, as shown in Figure 5.2 (b). The result shows that the double FLs switched simultaneously, and the MTJs exhibited a bi-resistance state, denoted as $R_{AP} = 173.7\ \Omega$ (AP: antiparallel) and $R_P = 79.3\ \Omega$ (P: parallel).

Specifically, resistance transition events were observed at the switching field of +135 and −85 mT, which is attributed to the stray field from the Co/Pt SAF layers. The difference in the loop shift between the full-sheet film and patterned MTJ is in agreement with that of the previous studies[157,159]. The TMR ratio was calculated to be 119%, which could be further enhanced by optimizing the MTJ structure, as reported in previous studies; however, this was beyond the scope of the present work.

5.2.2 Fs laser-assisted "write" operation

We further investigated single-pulse fs laser-assisted switching in the p-DMTJ device. In the measurement, the p-DMTJ was first saturated by an external magnetic field. Thereafter, as shown in Figure 5.3, the p-DMTJ was exposed consecutively to linearly polarized laser pulses with the laser energy of 600 nJ, which was synchronized with a bipolar out-of-plane magnetic field sequence of ±60 mT (+ and − denoted as "1" and "0", respectively) for a duration of 1 s.

The laser pulse duration was ≈ 100 fs, with a spot size of 100 µm and wavelength of 700 nm. The repetition rate of the laser was set to 0.5 Hz to avoid the accumulated heating effect. The magnetoresistance response of the p-DMTJ was measured using a four-point TMR measurement in real time, with a sampling interval of 250 ms.

Figure 5.3 shows the results of fs laser-assisted switching in the p-DMTJ under different configurations. In Region I, which was used as a comparison, in the case when only a bipolar magnetic field sequence was applied without firing a laser pulse, both the P and AP states were stable against such disturbances. Switching was only possible when the magnetic field sequence was synchronized by the fs laser pulse train with the pulse energy of 600 nJ.

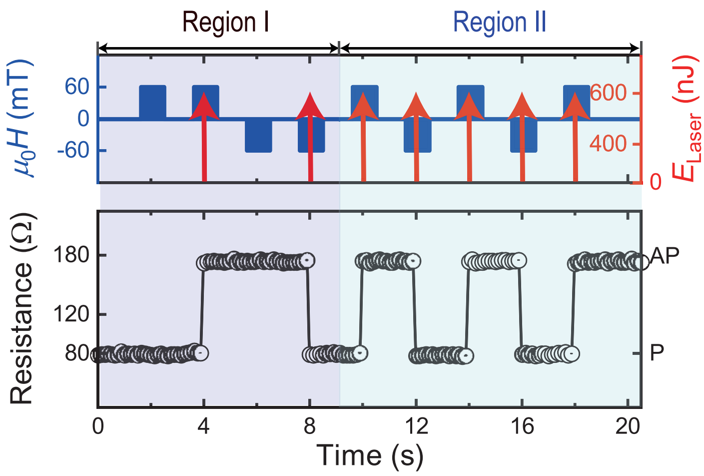

Figure 5.3: Experimental demonstration of fs laser-assisted toggle "write" in the p-DMTJ device. In the measurement, the p-DMTJ was exposed consecutively to linearly polarized laser pulses, which were synchronized with a bipolar out-of-plane magnetic field sequence of ±60 mT. The switching was readout electrically through four-point TMR measurement in real time. In Region I, when only a bipolar magnetic field sequence was applied without firing a laser pulse, both the P and AP states were stable against such a magnetic field disturbance. Switching was only possible when the magnetic field sequence was synchronized by the fs laser pulse train with a pulse energy of 600 nJ. In Region II, robust fs laser-assisted switching of the p-DMTJ was observed, which was determined by the direction of the bipolar magnetic field sequence. The resistance was equal to that in the R-H loop, indicating a complete reversal. The final resistance state (R_P, R_{AP}) was determined by the direction of magnetic field sequence ("0" and "1").

As shown in Region II, a robust toggle switching of the p-DMTJ upon every fs laser pulse was observed. The fs laser-assisted TMR switching was determined by the direction of the bipolar magnetic field sequence. The resistance was equal to that in the R-H loop, indicating a complete reversal. The final resistance state (R_P, R_{AP}) was determined by the direction of the magnetic field sequence ("0" and "1"). These results indicate that the proposed laser-assisted writing scheme could be well implemented in p-DMTJ devices because a reliable "write" operation is critical for binary storage devices.

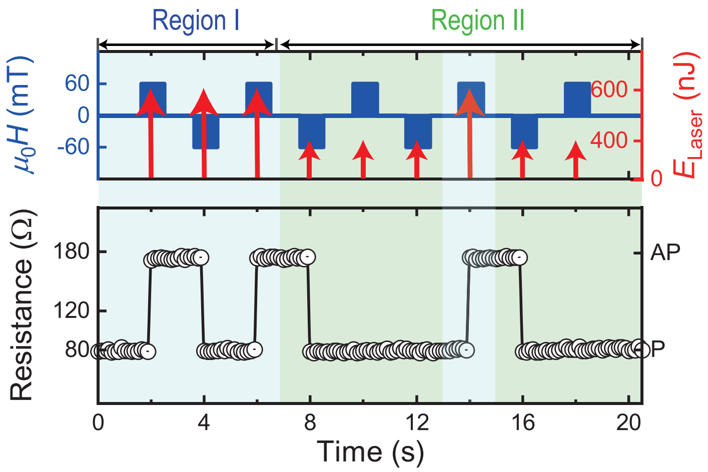

Figure 5.4: Experimental demonstration of fs laser-assisted unidirectional "reset" in the p-DMTJ device. In Region I, which was the reference, a magnetic field sequence was synchronized again by the fs laser pulse train with the single-pulse energy of 600 nJ. A reliable toggle switching was also observed. In Region II, the laser pulse energy was reduced to 400 nJ. Here, only a unidirectional switching to the P state was observed, and it never toggled back to the AP state using the same configuration. Switching back to AP was only possible with higher laser energy.

5.2.3 Fs laser-assisted "reset" operation

In magnetic storage devices, controllably resetting the memory bit before a "write" operation is often desirable. To validate the unidirectional "reset" operation, the fs laser-assisted switching measurement was performed, as shown in Figure 5.4.

In Region I (the reference), the magnetic field sequence was synchronized again by fs laser pulse train with the single-pulse energy of 600 nJ. A reliable toggle switching to both the AP and P directions was also observed, as shown in Figure 5.3. In Region II, the laser pulse energy was reduced to 400 nJ. Here, only the unidirectional switching to the P state was observed; it never toggled back to the AP state for the same configuration. Switching back to AP was only possible with higher laser energy (600 nJ in our measurements). This asymmetrical switching behavior could be partially attributed to the stray field of the p-DMTJ, which is further discussed in a next section.

We verified the feasibility of the fs laser-assisted switching in the p-DMTJ. Two

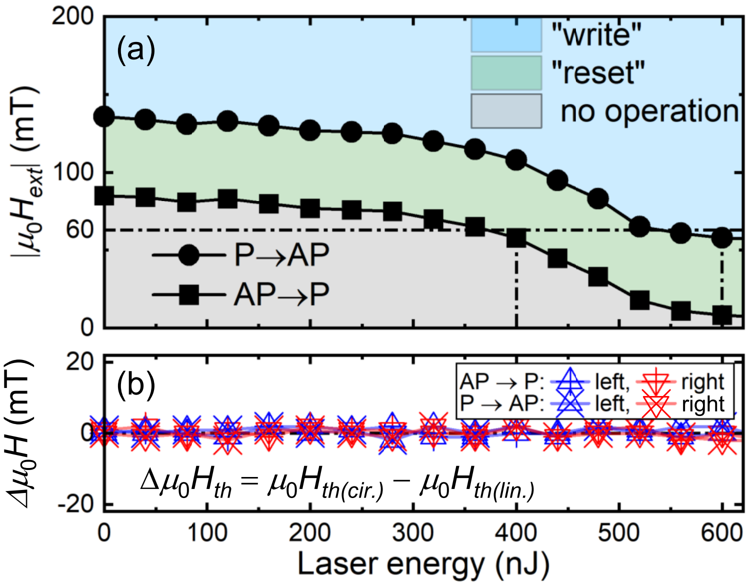

Figure 5.5: Joint effect of the fs laser, magnetic field, and stray filed of p-DMTJ on the proposed switching scheme. (a) Switching phase diagram of fs laser-assisted switching in the p-DMTJs, with the interplay between the fs laser pulse energy and write sequence. Three configuration regimes of the proposed switching scheme are shown. In the case of $|H_{ext}| < |H_{th,AP\to P}|$ (gray region), no successful MTJ switching was observed for both states. In the case of $|H_{ext}| > |H_{th,P\to AP}|$ (blue region), a regime of toggle "write" was observed. For $|H_{th,AP\to P}| < |H_{ext}| < |H_{th,P\to AP}|$ (green region), only the unidirectional AP $\to$ P switching was observed. (b) Typical helicity-dependent measurement for AP $\to$ P and P $\to$ AP switching by fs laser pulse with left- and right-handed circular polarizations, respectively. $\Delta\mu_0 H$ denotes the $|H_{th}|$ deviation relative to the ones for linear polarization. No significant helicity dependence effect was observed using different laser helicity, indicating the major role of conventional TAS induced by laser heating and negligible circular dichroism.

proofs-of-concept functionalities, i.e., toggle "write" and unidirectional "reset," were implemented by the interplay of the laser energy and magnetic field sequence. These reconfigurable laser-assisted switching operations indicate an emerging potential for integrated photonic–spintronic storage devices.

5.2.4 Discussion

We further investigated the effect of the laser pulse energy (E_p), magnitude of the magnetic field ($|H_{ext}|$), and stray field of the p-DMTJ on the proposed switching scheme. The p-DMTJ device was exposed to a laser pulse train with E_p ranging from 0 to 600 nJ. Thereafter, a synchronized H_{ext} write sequence with the magnitude from 0 to 140 mT was applied. The repetition rate of each measurement was set to 0.1 Hz to avoid accumulative laser heating. The switching was electrically monitored with a real-time TMR measurement.

Figure 5.5 (a) shows the switching phase diagram of the p-DMTJ under the joint effects. For both P $\rightarrow$ AP and AP $\rightarrow$ P cases, the threshold $|H_{ext}|$ for deterministic switching (denoted as $|H_{th}|$) gradually decreased as the laser energy increased, indicating lowered coercive field. A 92% decrease in $|H_{th,AP\rightarrow P}|$ was observed at $E_p = 600$ nJ. The relatively small laser energy to almost fully demagnetize the FL is attributed to an efficient heat transmission of the fs laser pulse compared with current-induced heating in TAS.

Furthermore, due to the thermal nature of the proposed scheme, the required laser energy could be scaled down to tens of fJ to write a nanosized MTJ. As already implemented in HAMR technology, using integrated photonic techniques, such as using a nano-photonic plasmonic antenna, a spot radius below 40 nm could be generated[135]. Thus, the proposed scheme shows good potential with enhanced efficiency and scalability.

We observed three configuration regimes of the fs laser-assisted switching scheme, as depicted in Figure 5.5 (a). In the case of $|H_{ext}| < |H_{th,AP\rightarrow P}|$ (gray region), no successful MTJ switching was observed for both states. For $|H_{ext}| > |H_{th,P\rightarrow AP}|$ (blue region), a regime of binary "write" was observed. These results are consistent with those shown in Figure 5.3. Moreover, in the case of $|H_{th,AP\rightarrow P}| < |H_{ext}| < |H_{th,P\rightarrow AP}|$ (green region), only unidirectional AP $\rightarrow$ P switching was observed, as shown in Figure 5.4.

The difference between the $|H_{th,P\rightarrow AP}|$ and $|H_{th,AP\rightarrow P}|$ demonstrates the asymmetric switching behavior of the proposed scheme, which may be partially attributed to the spatially nonuniformly distributed out-of-plane stray field of the p-DMTJ. The spacing between the two $|H_{th}|$ was almost independent of laser energy, indicating a negligible demagnetization of the reference layer that produces the stray field. Because switching in micro-sized p-MTJ devices is initiated by the domain nucleation and wall propagation, the inhomogeneous distribution of the stray field significantly affects the region where the nucleation starts[183]. Moreover, the out-of-plane stray field acting on the edges of FLs is much higher than that at the center[183,184]. Accordingly, lower $H_{th,AP\rightarrow P}$ might be attributed to the stray field that assists nucleation at the edges, and a smaller $|H_{ext}|$ is needed for complete switching.

However, other magnetic interactions, together with the joint effects of ultrafast heating, might also be nontrivial factors causing the asymmetry behavior observed here. Further quantitative investigation on the role of the stray field of p-DMTJs is beyond the scope of the present work. Above all, the combined effects, with the switching phase diagram, provide some insights into the proposed fs laser-assisted switching scheme.

Finally, we investigated if either all-optical helicity-dependent switching (AO-HDS) or magnetic circular dichroism in the PMA layers[8,128,132] gives rise to significant laser helicity dependence on the p-DMTJ. Previous studies[113] reported that laser-induced helicity-dependent switching can be observed using multiple laser pulses in some of the ferromagnetic systems, such as Co/Pt multilayers and FePt granular media, although not including the CoFeB/MgO system yet. Thus, we consider if significant laser helicity dependence on the CoFeB/MgO-based p-DMTJ exists because it may add functionality for future integrated optospintronic storage applications.

To this end, we measured the fs laser-assisted switching in the p-DMTJ using left- and right-handed circularly polarized laser pulses. Figure 5.5(b) shows the results for AP $\rightarrow$ P and P $\rightarrow$ AP of the $|H_{th}|$ deviation compared to the ones using linear polarization. No significant helicity dependence was observed using different laser helicity for switching to both the directions, indicating the major role of conventional TAS induced by laser heating and negligible circular dichroism.

To enhance the helicity-dependent effect, we propose that material explorations are the first step. By properly designing multilayer stacks or using ferrimagnetic systems such as GdFeCo, the helicity-dependent effect could be enhanced and implemented into device applications, but it was beyond the scope of our present paper.

5.3 Conclusions

In this study, we experimentally investigated fs laser-assisted switching in a high-performance p-DMTJ device. The feasibility of the proposed scheme was explicitly verified through real time electrical TMR measurements. Notably, reconfigurable laser-assisted switching operations, including binary "write" and unidirectional "reset," were validated using fs laser pulses and synchronized write sequence.

Moreover, the joint effects of the laser, magnetic field, and stray field of the p-DMTJ were investigated, and a switching phase diagram was obtained. Negligible laser helicity dependence was also observed, which is attributable to the dominance of thermally-assisted magnetic switching induced by the fs laser pulse. The proposed fs laser-assisted writing scheme for p-DMTJs is promising for future high-density optospintronic storage applications.

6

Picosecond Optospintronic Tunnel Junctions

Perpendicular magnetic tunnel junctions (p-MTJs), as the building blocks for spintronics, offer substantial potential for next-generation nonvolatile memory architectures. However, the performance of such devices is fundamentally hindered by spin-polarized-current-based switching mechanisms. Here, we report an optospintronic tunnel junction (OTJ) device with picosecond switching speed, ultralow power, high magnetoresistance ratio, high thermal stability, and non-volatility. This device incorporates an all-optically switchable Co/Gd bilayer coupled to a CoFeB/MgO-based p-MTJ by subtle tuning of the Ruderman-Kittel-Kasuya-Yosida (RKKY) interaction. An all-optical "write" operation faster than 10 ps is explicitly confirmed by time resolved magneto-optic Kerr effect measurements. Moreover, the device shows a reliable resistance "read-out" with a relatively high tunnel magnetoresistance (TMR) of 34%, as well as promising scalability towards the nanoscale with ultralow power consumption (< 100 fJ for a ∼ 50 nm sized bit). Our work, as a proof-of-concept demonstration of optospintronic memory device, may pave the way for next-generation electronics.[*]

[*]This chapter has been submitted: **L. Wang**, C. Cheng, P. Li, Y. L. W. van Hees, Y. Liu, K. Cao, R. Lavrijsen, X. Lin, B. Koopmans, and W. Zhao, "Picosecond Optospintronic Tunnel Junctions", (2021)

6.1 Introduction

For decades, CoFeB/MgO-based perpendicular magnetic tunnel junctions (p-MTJs) have become the building blocks of the magnetic random-access memory (MRAM), highly promising towards next-generation nonvolatile memory architecture[5,6,35]. As to the operation mechanisms of the p-MTJ bit cell, the prototype of MRAM was typically based on magnetic field-induced switching, whereas state-of-the-art MRAM technologies are dedicated to spin polarized current-induced switching schemes[64,66,157,185–187], such as spin transfer torque (STT) or spin orbit torque (SOT). Unfortunately, limited by the spin precession process, the operation speed of these p-MTJs is still around sub-nanosecond whilst requiring extremely high current densities[103,159,188], reducing of which remained a long-existing challenge for modern spintronic R&D.

To address this issue, integrating femtosecond laser, i.e., the fastest stimulus commercially available, with MRAM, has been conceptually considered as a competitive route toward ultrafast non-volatile memory[7,189,190]. About one decade ago, all-optical switching (AOS) was discovered in ferrimagnetic alloys[94,98,113], which further features ultrafast (< 20 ps) and energy-efficient (< 100 fJ for a ~ 50 nm sized bit). The AOS shows high potential towards integrating high-throughput interconnect advantages of photonics, with the non-volatile and ultra-low-power performance of spintronics. Consequently, all optically addressable optospintronic tunnel junction (OTJ) devices, with picosecond switching speed and least-dissipative energy consumption, are envisioned[7,189,190]. However, key scientific issues related to physical mechanisms, material exploration, as well as device fabrication still need to be solved.

Fundamentally, the implementation of OTJ devices involve physical effects in terms of laser-induced magnetization switching mechanisms, electrical resistance read-out, and nonvolatile storage features. Specifically, to ensure ultrafast data writing and reliable resistance read-out, single-pulse helicity-independent AOS (AO-HIS)[94,98,128] and appreciable TMR effects become indispensable[64,66,157]. In addition, to increase data storage density and improve thermal stability, strong perpendicular magnetic anisotropy (PMA) is highly required[66,185].

Incorporation and optimization of these physical effects to realize the OTJ device functionalities further raise requirements regarding materials design and device structures. As to the materials issue, the multilayered stack of an OTJ device include electrode layers (especially the need for an optical transparent electrode layer on the top), an optically switchable free layer (FL), MTJ core layers to ensure high TMR, a synthetic antiferromagnetic (SAF) reference layer (RL), etc. To realize single-pulse AO-HIS effect with the ability of efficient switching, rare earth - transition metal (RE-TM) alloys or multilayers, including GdFeCo, Co/Tb, Co/Gd are feasible[98,113,128].

A suitable FL structure for the OTJ should also be compatible with robust AO-HIS, high TMR, and strong PMA effects. Thus, a synthetic FL with the optically switchable layer coupled to a CoFeB/MgO layer has become a mainstream technological route[7,125,127]. Among the attempts, Avilés-Félix *et al.*[127] reported single-pulse AOS of a MTJ electrode using Co/Tb multilayers[127]. However, scientific and engineering issues, such as the OTJ stack design, the fs switching dynamics, as well as the integration of bottom-pinned structure, still need to be solved before the advent of practical applications.

As to the device functionalities, a robust single-pulse laser-induced TMR toggle switching, as well as a high thermal stability at the nanoscale with non-volatility, should be maintained simultaneously. Among the attempts, Chen *et al.*[124] employed all-optically switchable GdFeCo directly as the free layer to fabricate an MTJ[124], although resulting in a relatively low TMR ratio of 0.6% and weak PMA. To fully utilize the great potential of opto-spintronics for next-generation memory, experimental demonstrations as well as performance verifications of prototype OTJ devices are still highly desired.

In this work, we design and experimentally demonstrate a fully functional optospintronic tunnel junction (OTJ) memory device with an ultrafast operation speed (< 20 ps), sufficiently high TMR ratio (34%), low threshold fluence (3.1 mJ/cm^2), as well as high thermal stability and non-volatility. By using Ruderman-Kittel-Kasuya-Yosida (RKKY) interaction, a synthetic free layer structure, with

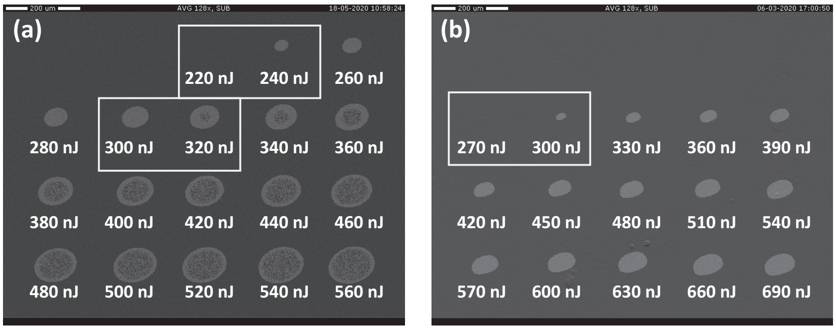

Figure 6.1: Typical AOS measurements on two types of the engineered material systems. textbf(a) AOS measurement performed on the Gd/CoFeB/MgO system using Kerr microscopy. Single fs laser pulses with different E_p (indicated in the figure) were used to excite the film. **(b)** AOS measurement performed on the composite Gd/Co/Ta/CoFeB/MgO system using the same method. A significantly broader AOS writing window is observed, in contrast to (a).

an all-optically switchable ferrimagnetic Co/Gd bilayer coupled to a ferromagnetic CoFeB layer is developed. Such an interlayer exchange interaction through an atom-thick spacer realizes the simultaneous AOS of the synthetic FL with a high PMA and TMR effect.

Moreover, as a nonvolatile photonic memory, the proposed OTJ exhibits efficient all-optical toggle writing, as well as a reliable electrical TMR read-out in real time even for single shot switching using a 100-fs laser pulse. Lastly, the picosecond switching speed of the OTJ device with full scalability, is explicitly confirmed by time-resolved magneto-optical measurements, demonstrating its potential towards nanoscale applications.

6.2 OTJ free layer design by material exploration

In this section, our research efforts on exploring a novel AOS material system are summarized. The goal is to explore a suitable free-layer structure for the OTJ device. To design such a materials platform, several multi-dimensional considerations have to be addressed. Specifically, i.) a robust single-pulse AOS is required to enable an ultrafast and energy-efficient data "write", as already discussed in Chapter 2; ii.) a high TMR ratio is required to achieve a high "read" margin of the bi-stable OTJ device; iii.) a relatively high anisotropy, i.e., PMA, is required to maintain a long data retention and high thermal stability at nanoscale.

Focusing on these requirements, nanostructured material design and engineering are carried out, leading to two types of material systems that are highly relevant to this thesis. Here we only summarize the experimental results very briefly.

As discussed in the Chapter 1, the CoFeB in direct contact with the MgO would lead to a high TMR and PMA, which has become the mainstream technological route of MTJ design. As a result, we design and investigate two types of structures, which we will refer to as "type I" and "type II" in the following. In the "type I" design, a structure employing Gd in direct contact with CoFeB, i.e., Gd/CoFeB/MgO, is synthesized. The system is chosen because the Gd and CoFeB are antiferromagnetically coupled, and are known to have two very contrasting laser-induced demagnetization times, thus single-pulse AOS could be expected.

In the "type II" design, a composite Gd/Co/Ta/CoFeB/MgO structure is proposed. In this configuration, the Co and the CoFeB are ferromagnetically coupled through an atom-thick Ta spacer due to the RKKY interlayer coupling. This composite structure is chosen because it would simultaneously facilitate the robust AOS feature of the ferrimagnetic Gd/Co layers, and the high PMA and TSP advantages of the CoFeB/MgO interface as well.

AOS measurements are first performed on the "type I" samples, with a configuration of Pt (3)/Gd (2)/$Co_{20}Fe_{60}B_{20}$ (t)/MgO (2)/Ta (3). The stacks were deposited on a glass substrate at room temperature (RT) using DC magnetron sputtering at a base pressure of 10^{-9} mbar. Numbers in parentheses denote the thicknesses of each layer in nanometer, and t is $1 - 1.2$ nm. A considerable PMA is achieved for the thin-film sample series, as verified by SQUID-VSM measurements.

Next, we investigate the response of the magnetization of the film upon a train of laser pulse excitation. The experimental setup has been discussed in Section 3.3.6, which is also heavily employed in Chapter 4. In the measurements, which are performed at room temperature, the sample is first saturated by an external magnetic field. Afterwards, the field is turned off and the film is exposed to subsequent linearly polarized laser pulses, with different laser pulse energies (E_p). The duration of each laser pulse is 100 fs, with a spot radius of typically 60 µm and a wavelength of 700 nm. The responses of the magnetization after laser-pulse excitation are measured by Kerr microscopy, where dark or light regions show "up" or "down" magnetic domains in the film.

Fig. 6.1 (a) illustrates typical AOS results using Kerr microscopy on the Gd/CoFeB/MgO system. The film is exposed to single fs laser pulses with E_p indicated in the figure. We observe that, as to $E_p < 240$ nJ, no AOS written domain is observed, whereas for the $E_p > 240$ nJ, a gradual increase of the AOS domain size upon higher laser energies is found. In addition, a multidomain state begins to appear upon $E_p > 320$ nJ, the region in which this occurs shows an increasing area for higher laser energies. In this case, single-pulse AOS is only observed in a relatively narrow rim of the AOS domain.

These results reveal that the AOS energy window is extremely narrow in this type of system, corresponding to an insufficiently small "write" margin for practical device applications. As a result, it may not be suitable for our further studies at a device level. The physical mechanism behind it was partly attributed to the role of heat diffusion in the system.

To solve this limitation, in the "type II" design, a composite Gd/Co/Ta/CoFeB/MgO structure is investigated. In the AOS measurements, which are performed on Pt (2)/Gd (3)/Co (1)/Ta (0.3)/$Co_{20}Fe_{60}B_{20}$ (1)/MgO (1)/Ta (3) stacks, all optically reversed domains are observed upon 300 nJ$< E_p <$ 690 nJ, the area of which increases upon higher E_p. A significantly broader AOS window compared to the "type I" design is clearly observed, as shown in Fig. 6.1 (b).

In other words, in the "type II" design, we were able to increase the laser energy to more than 100% above threshold without obtaining a multi-domain state, whereas a multidomain state emerged already 30% above threshold in the "type I" design. As a result, such a composite free-layer structure would be more suitable to incorporate at a device level in our further research. By incorperating RKKY interaction, this design rule may also be feasible for other opto-spintronic

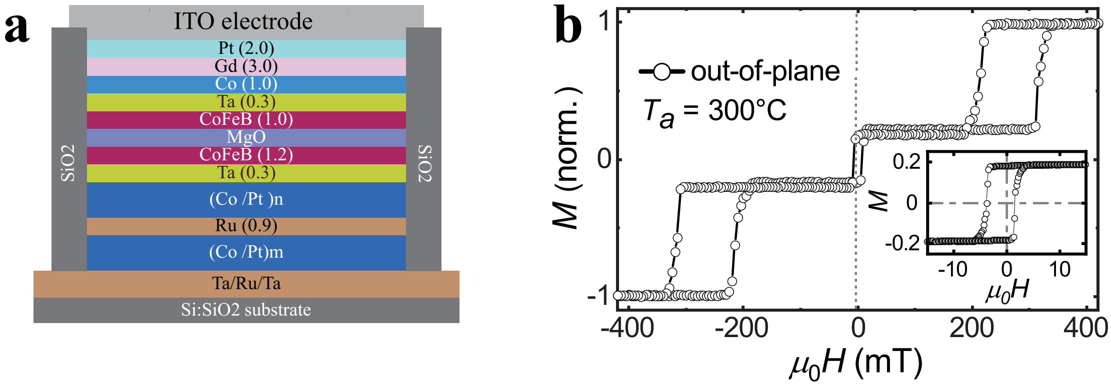

Figure 6.2: OTJ structure and magnetic characteristics. (a) Schematic structure of the proposed OTJ memory device. Ta/Ru/Ta and ITO are the bottom and top electrode, respectively. [Co/Pt]m/n multilayers based SAF is used as the reference layer (RL), MgO as the tunnel barrier. The composite free layer (FL) consists of the top CoFeB layer and the Co/Gd bilayer, which are RKKY coupled through an atom-thick Ta spacer. **(b)** Out-of-plane hysteresis loop of the OTJ stack after post-annealing at 300°C measured by a VSM-SQUID. The square hysteresis loops with 100% remanence indicates a well-defined PMA in both FL and RL. The minor loop of the OTJ stack, as shown in the inset, indicates that two parts of the FLs switch simultaneously due to the strong RKKY coupling.

devices. Next, we employ the composite material platform in to a mainstream CoFeB/MgO-MTJ stack, and characterize the device in a systematic manner.

6.3 Results and discussion of the OTJ device

6.3.1 OTJ film structure and PMA characterization

As illustrated in Fig. 6.2 (a), the designed OTJ stack is composed of, from the substrate side upwards, Ta (3)/Ru (20)/Ta (0.7)/$[Co/Pt]_m$ (9.8)/Ru (0.9)/$[Co/Pt]_n$ (3.6)/Ta (0.3)/CoFeB (1.2)/MgO (1)/CoFeB (1)/Ta (0.3)/Co (1)/Gd (3)/Pt (2) (numbers in parentheses denote the layer nominal thicknesses in nanometer, and the subscripts are the repeated numbers), which is deposited by DC and RF magnetron sputtering (see Section 6.4).

In this configuration, Ta/Ru/Ta is the bottom electrode, the combination of the $[Co/Pt]_{m/n}$ multilayers with the bottom CoFeB serve as the SAF RL. Such design is used to fix the magnetization direction of CoFeB, which is crucial for practical

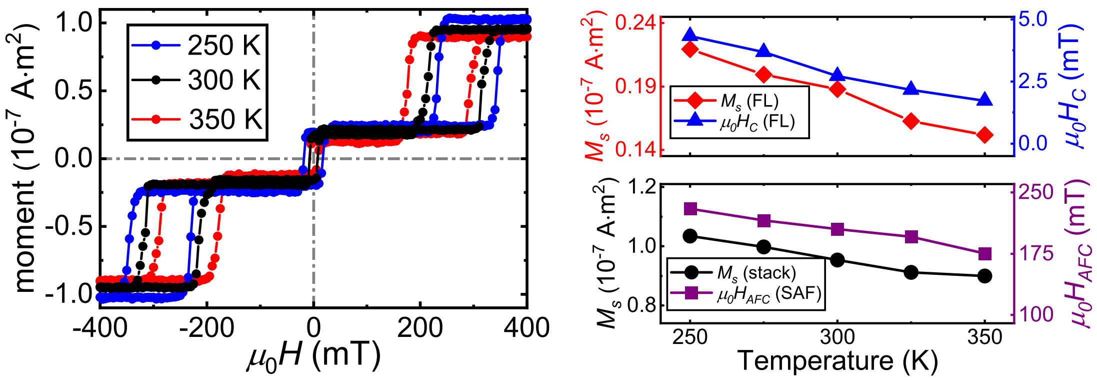

Figure 6.3: Temperature dependence of the magnetic properties of the OTJ stack. (a) Magnetic hysteresis loops of the OTJ stack versus an external perpendicular magnetic field (M-H) loops, measured at 250 K, 300 K, 350 K, respectively. **(b)** Bottom: Temperature dependence of the saturation magnetization (M_s) of the complete stack (left, black dots) and antiferromagnetic coupling field (μ_0 H_{AFC}) (right, purple squares) ranging from 250 K to 350 K. Top: Temperature dependence of M_s of the free layer (left, red diamond) and their coercive field (μ_0 H_c) (right, blue triangles).

MRAM application. The MgO layer is the tunnel barrier. As to the synthetic FL, the top CoFeB/MgO layer and the all optically switchable Co/Gd bilayer are coupled through an 0.3-nm-thick Ta spacer. Such stack design ensures high TMR, high PMA, and effective AOS simultaneously.

Recently, we demonstrated the merits of ferrimagnetic Co/Gd for future ultra-high density spintronic memories[132,135,191], such as a fully compatible fabrication process, as well as extended flexibility on interface engineering for high domain wall (DW) velocity and inherent built-in interfacial Dzyaloshinskii-Moriya interaction[129,171,192]. The Ta spacer is used to ensure an effective RKKY coupling, where moderate coupling strength is adopted to guarantee all-optical toggle switching of the synthetic FL.

As typical AOS materials are extremely sensitive to alloy composition and annealing, in a recent study[193] we showed that the AOS efficiency is considerably enhanced after 300°C thermal annealing, offering a fully compatible fabrication process with p-MTJ integration. After deposition, the stacks are thus subjected to thermal annealing at 300°C in vacuum for an hour, which is used to enhance the crystalline quality of the MgO barrier and the bcc (body-centered cubic) texture

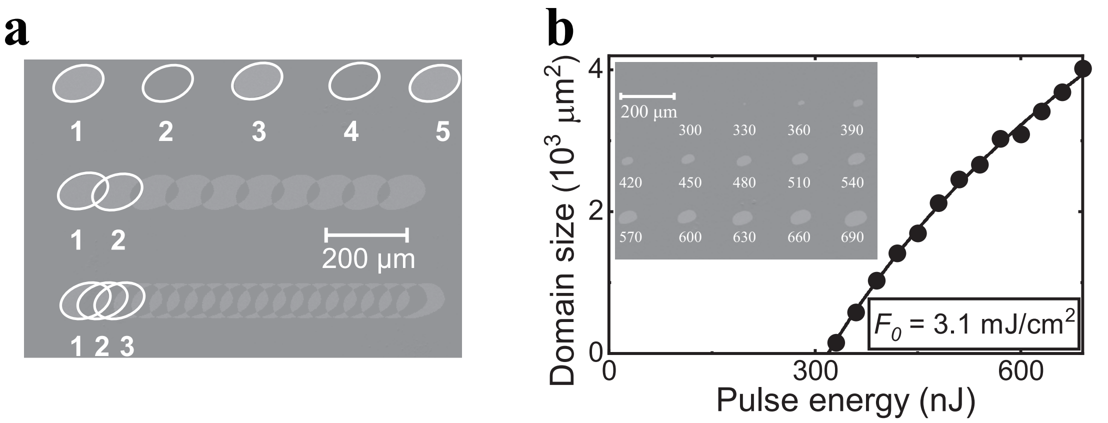

Figure 6.4: Deterministic single-pulse AOS measured by Kerr microscopy. **(a)** Row (.9): Single-pulse AOS measurement by subsequent fs laser pulses. The numbers correspond to the number of pulses that the region is exposed to. Row (II – III): AOS measurements by laser pulse train at a repetition rate of 2.5 Hz and 5 Hz, respectively, leading to partly overlapping pulses. **(b)** Laser-pulse energy dependence of the AOS domain size, showing the threshold laser energy (P_0) of 330 nJ, and an increasing domain size with higher laser energies. The threshold fluence (F_0) of the OTJ stack is calculated to be 3.1 mJ/cm^2. Inset: Kerr microscopy of the measurement performed on the OTJ stack. The numbers correspond to the laser energy of each spot in unit of nJ.

of the CoFeB, thus a higher TMR can be expected.

Fig. 6.2 (b) shows the out-of-plane magnetization versus magnetic field (M-H) hysteresis loop of the OTJ stack using a VSM-SQUID at room temperature (see Section 6.4). The film exhibits the presence of strong PMA in both the FL and the RL indicated by the 100% remanence and squareness of the hysteresis loops, which ensures high thermal stability and nonvolatility. According to the steep minor loop (inset of Fig. 6.2 (b)), the coercive field of the FL reaches 4 mT, and two parts of the FLs switch simultaneously, which is paramount for the OTJ performance. Note that a relatively small shift of the hysteresis loop indicates a significant reduction of stray field due to the Co/Pt multilayered based SAF structure. Such a pinned layer design is essential for our OTJ, because a large stray field would hinder AOS in the opposite direction, losing toggle operation characteristics.

In addition, the M-H hysteresis loop of the OTJ ranging from 250 K to 350 K is

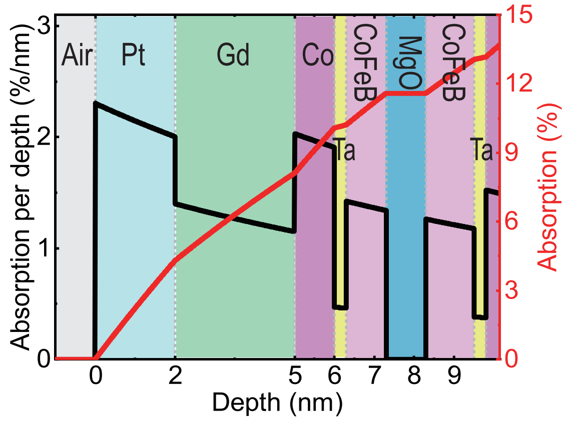

Figure 6.5: Calculation of optical absorption profile of the OTJ stack. The full stack structure as well as the thermally oxidized Si:SiO_2 substrate are included in the calculation. Left: Optical absorption per depth (%/nm) vs. Layer Depth.

measured, as shown in Fig. 6.3 (a). Fig. 6.3 (b) shows the temperature dependence of the magnetic properties, which are extracted from the M-H hysteresis loops. The left axis in the bottom panel shows the saturation magnetization (M_s) of the full stack (black dots), whereas the left axis in the top panel shows the M_s of the FL (red diamonds). A clear temperature dependence of M_s is observed, enhancing upon lower temperature, as expected from the Bloch law. Note that although the Curie temperature of the bulk Gd is slightly lower than room temperature, it is enhanced at the Co interface due to the proximity induced effect[128,135].

The left axis of the bottom panel shows the temperature dependence of the antiferromagnetic coupling field ($\mu_0 H_{AFC}$) of the SAF layer (purple squares). Specifically, compared with $\mu_0 H_{AFC}$ = 175 mT at 350 K, it is enhanced to 230 mT at 250 K. The right axis of the top panel shows the coercive field $\mu_0 H_c$ of the FL (blue triangles), which is also enhanced from 1.7 mT to 4.3 mT, corresponding to a 153% increase. These results indicate a broad working temperature range of the OTJ stack for practical applications.

6.3.2 Single-pulse all-optical switching of the OTJ film

We first investigate the single-pulse AOS of the OTJ full stack before device patterning. In the measurements (see Section 6.4), the sample is exposed to subsequent linearly polarized laser pulses, whereafter its magnetization response is measured using magneto-optical Kerr microscopy in a static state. As shown in the Fig. 6.4 (a), five separate spots are excited by a different number of laser pulses (Row I). We observe that a homogeneous domain with an opposite magnetization direction is written for every odd number of laser pulse, whereas it toggles back for every even number of pulses.

Then, the OTJ stack is exposed to a laser-pulse train with partly overlapping area (Row II – III, see Section 6.4). As to the regions exposed by a single or three-overlapping pulses, a reversed domain is observed. In contrast, for the regions where only two pulses overlap, no net reversal is observed. Here, we also note that the DW at the overlapping regions stay intact, whereas the domains toggle upon every laser excitation. The observed results are consistent with the thermal AOS mechanism discussed in previous studies[94,128], demonstrating a robust toggle AOS operation in the OTJ stack.

As to the next-generation memory device, it is always essential to reduce the critical writing energy needed to switch a memory bit cell. Therefore, the threshold laser energy, to write the OTJ stack is investigated, which is done by measuring the pulse energy dependence of the domain size (see Section 6.4). As shown in Fig. 6.4 (b), a threshold laser energy (P_0) of 330 nJ is observed for a laser spot with a diameter of approximately 50 µm. Above P_0, the laser written domain size increases with higher laser energies.

The AOS threshold fluence (F_0) of 3.1 mJ/cm^2 is then determined by assuming a Gaussian shape of the laser pulse[128], which is lower than that for GdFeCo alloys[94,98]. Further reduction of F_0 can be expected by decreasing the thickness of the ferromagnetic layer, as discussed in previous studies[128]. Moreover, due to the thermal nature of the AOS, the energy for writing a sub-20 nm OTJ bit could scale down to a few tens of fJs using a plasmonic antenna[105,135,194] as already used in heat assisted magnetic recording (HAMR) techniques, which is potentially competitive with state-of-the-art spintronic memories[6,7].

To evaluate the feasibility of the AOS in the RKKY-coupled FL, we calculate the optical absorption of each layer in the OTJ stack using a transfer matrix scheme. The optical profile of the complete stack is shown in Fig. 6.5. The optical absorption in this OTJ stack is calculated by inputting the layer-specific refractive index values at 700 nm. The left axis indicates the absorption per depth (%/nm), as a function of layer depth. The absorption in the layer is then calculated by integrating over the thickness, as plotted in the right axis.

One might expect that the relatively thick stack, with a Pt layer on top, would lead to a strong loss of optical energy, thus negligible laser-induced phenomena in the OTJ. However, in our calculation, we observe that nearly 12% of the laser energy is absorbed by the synthetic FL layer. We find that this value is significantly enhanced due to the Si:SiO$_x$ substrate, which acts as a reflective layer. The total absorption in the FL is consistent with previous studies using Gd/Co bilayers[132,135]. Moreover, it has been proven that F_0 is partially attributed to the effective optical absorption in the Gd/FM (FM: ferromagnetic) layer, which partially explains that the F_0 of the OTJ stack is only slightly lower than more conventional AOS systems[98,128].

6.3.3 OTJ device fabrication and TMR measurements

Circular pillars are patterned using multistep UV lithography and an Ar ion milling process (see Section 6.4). Fig. 6.6 (a) shows an optical microscope image of the fabricated OTJ device with a pillar diameter of 3 µm (see the inset of Fig. 6.6 (a) for the zoom-in of the pillar) and four electrode pads. Note that the 100-nm-thick indium tin oxide (ITO) is employed as top electrode, which is crucial for our hybrid optospintronic device. Compared with the conventional Ti/Au electrode, the transparent ITO enables an efficient laser-pulse access, as well as a reliable electrical detection with a high signal-to-noise ratio (SNR).

The resistance versus magnetic field (R-H) loop is measured by sweeping an out-of-plane magnetic field, as shown in Fig. 6.6 (b). A clear bi-stable tunnel magnetoresistance (TMR) is observed, with R_{AP} = 227 Ω (AP: antiparallel) and R_P = 169 Ω (P: parallel), respectively. The RKKY coupled FL is found to switch

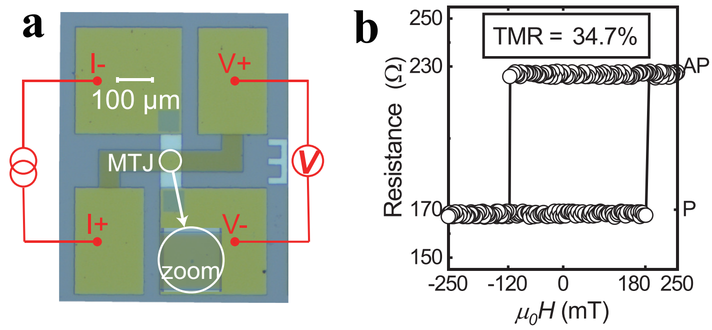

Figure 6.6: Characterization of the fabricated OTJ device. (a) Microscope image of the fabricated OTJ device with a 100-nm-thick transparent ITO top electrode, as well as four electrode pads to perform 4-point TMR detection. The inset shows the zoom-in of the OTJ pillar. **(b)** *R-H* magnetoresistance loop measured by sweeping an out-of-plane magnetic field, showing a typical TMR ratio of 34%.

as a single unit, as indicated by steep resistance transition events at +190 mT and −115 mT, respectively. A typical TMR ratio $(R_{Ap} - R_P)/R_P = 34\%$ is obtained for our proof-of-concept OTJ device after post-annealing, which could be further enhanced by optimizing the stack design, but goes beyond the aim of the present work. In addition, the improved SNR in the *R-H* measurement indicates an improved interface quality between the ITO and the OTJ pillar.

6.3.4 All-optical "write" operation of the OTJ device

Next, we investigate the electrical read-out performance of OTJ. As sketched in Fig. 6.7 (a), the programming of the OTJ is demonstrated using subsequent laser pulses, whereas the read operation is realized by an electrical TMR measurement in real time with down to sub-ns time resolution (see Section 6.4). The complete measurement is performed without any external magnetic field.

As shown in Fig. 6.7 (b), the TMR of the OTJ device toggles deterministically between the AP and the P state at the same frequency as the incoming laser pulses. In other words, binary programming a "1"/"0" of the OTJ is realized for every odd/even number of pulses, which is a basic writing operation for memory devices. The repeatability of the operation is further verified by a 100% success rate up to millions of repeated switches. Moreover, the magnetoresistance values mea-

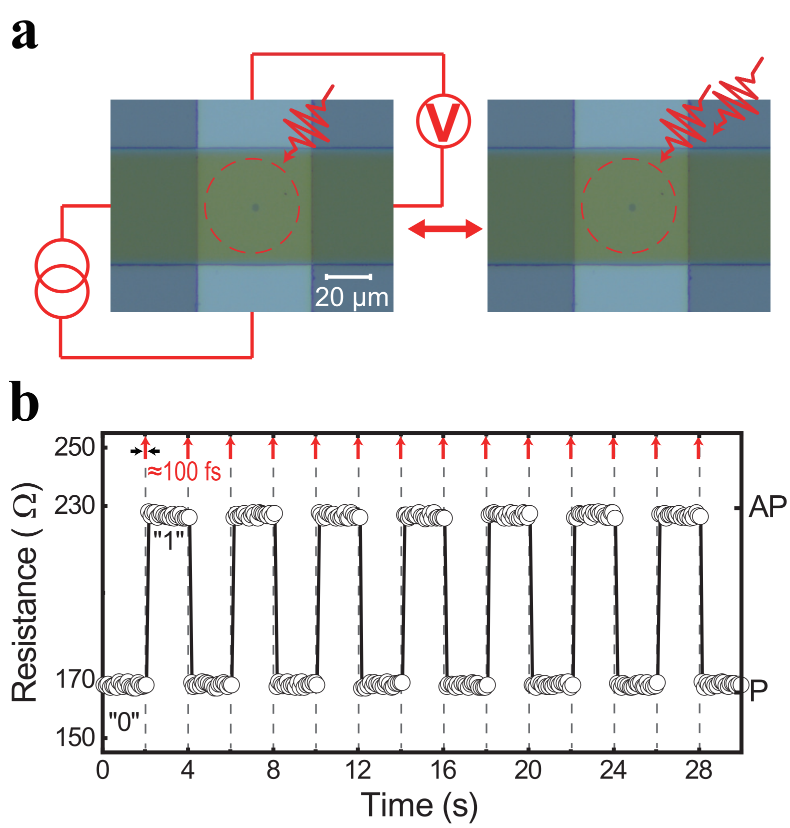

Figure 6.7: OTJ device functionalities: all-optical "write" operation and electrical TMR read-out. **(a)** Schematic overview of the AOS "write" operation of the OTJ device. A small current is applied through the OTJ, while the resulting TMR voltage is measured in real time. The OTJ pillar is excited by a train of linearly polarized laser pulses. **(b)** Typical TMR measurement as a function of time upon laser-pulse excitation. The resistance toggles between P and AP state upon every laser pulse excitation. No external field was applied during the measurements.

sured by AOS are equal to the ones in the *R*-*H* loop (Fig. 6.6 (b)), unambiguously demonstrating a complete reversal of the composite FL in the bottom-pinned OTJ.

We stress that this robust AOS is not trivial, since for our synthetic FL with a more complex structure, the toggle AOS could have been hindered by the stray field provided by the RL ($\sim$ 30 mT). Thus, the tendency for AOS of our entire FL is strong enough to overcome such bias field, and a toggle TMR operation is clearly observed.

To further address the potential of our OTJ for high data rate electrical read-out, we investigated the time-resolved TMR upon single-pulse laser excitation. Here, the OTJ is again exposed to subsequent laser pulses with a pulse width of 100 fs, whereas a fast-sampling oscilloscope with a sub-nanosecond resolution is employed to enable a time-resolved measurement (see Section 6.4). As a typical result shown in Fig. 6.8 (a), in case of a laser energy of 300 nJ, a robust switching faster than 1 ns is observed. However, as expected, in case of a laser energy of 145 nJ, i.e., below the threshold for switching, only an ultrafast thermal demagnetization followed by a demagnetization during 10 ns upon cooling down is observed.

Lastly, we stress that the design rules of such OTJs are not limited to Gd/Co bilayers. Under proper material design to maintain ultrafast AOS, high TMR as well as high thermal stability simultaneously after post-annealing, other emerging ferrimagnetic AOS systems may also hold great potential for further optimized performance[7,113,189].

6.3.5 Fs-time-resolved measurements of the OTJ switching

Lastly, we demonstrate the picosecond operation speed of the OTJ, which is a key characteristic for the next-generation ultrafast memory. Previous studies[94,98,113] have reported tens of picosecond AOS in some ferrimagnetic alloys. However, no time resolved AOS dynamics have been performed in an MTJ with additional optically switchable magnetic layers yet. Moreover, in the RKKY coupled FL, whether the switching speed is impeded has also remained unclear. Thus, time-resolved magneto-optical Kerr (TR-MOKE) measurements are performed (see Section 6.4) to clarify such concerns.

As illustrated in Fig. 6.8 (a), the laser-induced magnetization dynamics of the OTJ stack shows typical characteristics that are consistent with previous studies on time-resolved AOS studies[94,111]. Briefly, in the first several picosecond time scale, a rapid demagnetization is caused by the ultrafast laser heating. Afterwards, magnetization reversal takes place within 20 ps, due to the distinct demagnetization times[94] between the antiferromagnetically coupled Co and Gd sublattices, which is driven by the angular momentum transfer mediated by exchange scatter-

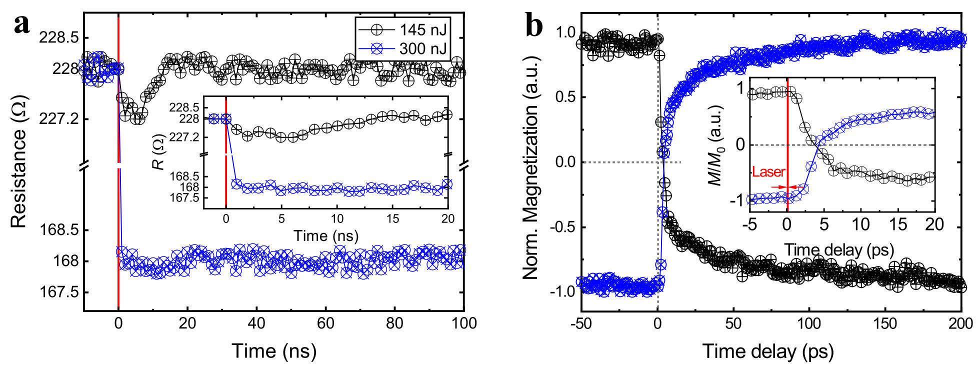

Figure 6.8: Picosecond speed demonstration of the OTJ by time-resolved measurements. **(a)** Typical time resolved TMR measurement result using a fast-sampling oscilloscope with a sub-nanosecond resolution. In the measurement, the OTJ is excited by subsequent laser pulses, whereas the TMR is measured in real time by a fast-sampling oscilloscope. In case of the laser energy of 300 nJ, we observe a clear TMR switching with the speed faster than 1 ns. However, in case of the laser energy of 145 nJ, only a thermal relaxation with a time scale of 10 ns is observed. This results clearly indicate that the operation speed of OTJ is beyond nanosecond regime. **(b)** Time-resolved magneto-optical Kerr (TR-MOKE) measurements performed on the OTJ full stack. The inset shows the zoom-in of the first 20 ps time scale. The switching speed is confirmed by magnetization reversal within 5 picoseconds.

ing[132]. Lastly, a reversed magnetization orientation indicates its settling to a new thermal equilibrium.

More importantly, we observe the zero-crossing point (see inset of Fig. 6.8 (b) for zoom-in) occurring at several picoseconds, and a full reversal to the saturated reversed state within tens of picoseconds. These results confirm that the CoFeB layer follows the Co/Gd quasi instantaneously on a picosecond time scale and highlight the ultrafast feature of the OTJ device.

After we have shown that the synthetic FL ensures single-pulse AOS with high PMA and thermal stability, we finally demonstrate a proper scaling behavior between the ultrafast operation speed and the patterned device size. TR-MOKE measurements on devices with pillar diameters of 10 µm, 5 µm, and 3 µm are performed, respectively, as shown in Fig. 6.9. Note that the relatively low SNR, compared to Fig. 6.8 (b), is attributed to the OTJ pillar size being smaller than the laser spot size (typically 20 µm), reducing the total magnetic signal collected

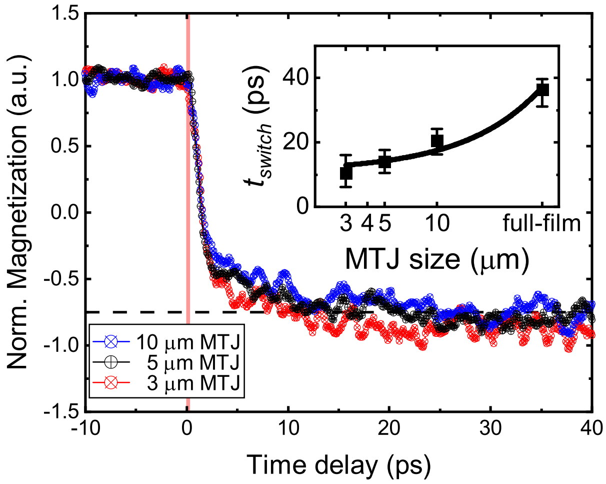

Figure 6.9: Scaling performance of the OTJ device. TR-MOKE measurements performed on the OTJ with pillar diameters of 10 µm, 5 µm, 3 µm, respectively. The results show that the ultrafast AOS speed is unimpeded in patterned devices, as proven by the magnetization reversal still within the picosecond time scale. Inset: the time needed for 75% magnetization reversal (t_{switch}) as a function of OTJ pillar size. The results may indicate a scaling dependence of t_{switch}, i.e., compared to $t_{switch} \approx 40$ ps for the full-sheet stack, it reduces to 10 to 25 picoseconds for the OTJ device.

by Kerr effect. We observe that the picosecond AOS speed is preserved upon scaling down to 3 µm, as proved by the magnetization reversal within 5 picoseconds.

For application purposes, we define the operation speed of the OTJ as the time (t_{switch}) needed to reach 75% opposite magnetization state, which is chosen because of a sufficient read margin for binary electronics chips[194]. As plotted in the inset of Fig. 6.9, t_{switch} of all the measured OTJ devices is in the range of tens of picoseconds. In addition, our results may even indicate a scaling dependence of t_{switch}, more specifically, a faster operation speed is observed for reduced dimensions. Although care has to be taken because of the limited SNR, the trend in our results is in reasonable agreement with recent studies using GdCo nanodots[194]. Especially, compared to $t_{switch} \approx 40$ ps for the full-sheet stack, it reduces to 10 – 25 ps for micro-sized OTJ devices (see inset).

We conjuncture that the nonuniform heat diffusion to the ambient, which causes the magnetization to settle to a new thermal equilibrium faster, may play a crucial role in this observed size dependence. However, other laser-induced magnetization phenomena, such as spin-lattice coupling and energy transfer rates as speculated in previous studies[111,194], may not be fully ruled out. Above all, by time-resolved studies, we demonstrate a picosecond operation speed of the OTJ device, highly promising towards future ultrafast memory applications.

6.4 Materials and Methods

Sample deposition

The OTJ stacks used in this work were deposited using DC and RF magnetron sputtering (AJA International Physical Vapor Deposition) at room temperature, which were deposited on a thermally oxidized Si (001) substrate at a base pressure in the deposition chamber of 10^{-9} mbar without an external magnetic field. The CoFeB target composition was $Co_{20}Fe_{60}B_{20}$ (in atomic percent), with a deposition rate of 3 min/nm at Ar pressure of $8{\cdot}10^{-4}$ mbar. The deposition rate for MgO was 5.5 min/nm at Ar pressure of $8{\cdot}10^{-4}$ mbar. After deposition, the stacks were annealed in vacuum (with a base pressure of 10^{-9} mbar) at 300°C for one hour without an external magnetic field.

Device fabrication

Micro-sized OTJ pillars were patterned by using a standard UV optical lithography in combination with argon ion milling process, at the center of Ta/Ru/Ta bottom electrode. The diameter of the OTJ pillars were 10, 5, 4, 3 µm, respectively. The samples were then covered with SiO_2 insulation by electron beam evaporation (EBV) and a lift-off procedure. Subsequently, the 100-nm-thick transparent indium tin oxide (ITO) were deposited as the top electrodes, also by EBV and a standard lift-off procedure. The quality of ITO deposition process is essential for the OTJ device, leading to an efficient laser-pulse access, and a reliable electrical detection as well.

Magnetic properties characterization

The magnetic characteristics of the full-sheet OTJ stack were investigated at 250K – 300K, respectively (Fig. 6.3), using a vibrating sample magnetometer - superconducting quantum interference device (VSM-SQUID), under an out-of-plane magnetic field ranging from ±400 mT.

The tunnel magnetoresistance of the OTJ were characterized at room temperature by a conventional four-point TMR measurement under an out-of-plane magnetic field in the range of ±200 mT. To measure the TMR signal, a small current (100 µA) was sent through the OTJ device, whereas the resulting magnetoresistance was measured using a lock-in amplifier.

Deterministic all-optical switching measurements

The response of magnetization in the OTJ stack upon subsequent femtosecond laser pulses (Spectra Physics Spirit-NOPA) were investigated. The laser pulse was linearly polarized, with a pulse duration of ≈ 100 fs at sample position, a central wavelength of 700 nm, a spot radius (1/e Gaussian pulse) typically of 25 µm, and a base repetition rate of 500 kHz. By using a pulse picker and a mechanical shutter, individual laser pulses could be picked out.

In the single-pulse AOS measurements (Fig. 6.4 (a), Row I), which were performed at room temperature, the magnetization was first saturated by an external field. Afterwards, the field was turned off and the stack was exposed to subsequent laser pulses. The numbers labelled in the figure correspond to the laser-pulse numbers of each spot. Then the OTJ stack was exposed to laser-pulse trains with partly overlapping areas. The laser-pulse train was set at a velocity of 0.2 mm/s, with a repetition rate of 2.5 Hz (Row II) and 5 Hz (Row III), respectively.

The responses of the magnetization after laser-pulse excitation were measured in steady state using magneto-optical Kerr microscopy, where light and dark regions were corresponding to up and down magnetization direction. As to the Kerr microscopy images, a differential technique was used to enhance the magnetic contrast. Specifically, a "background" image was captured in the magnetization saturation state. This "background" was then subtracted from the subsequent Kerr images after laser-pulse excitation. The scale bars in the Kerr images were 200 µm.

To determine the AOS threshold fluence of the OTJ stack, the OTJ stack was exposed to single laser pulses with different laser energies (E_P) as indicated in the inset of Fig. 6.4 (b) (in unit of nJ), whereafter the laser-pulse energy dependence of the AOS domain size was measured by Kerr microscopy (see inset of Fig. 6.4 (b) for the Kerr microscopy image). By assuming a Gaussian energy profile of the laser pulse, the AOS threshold fluence could then be determined.

All-optical operation of OTJ device

To investigate the all-optical programming operation of the device, the fabricated OTJs were excited by subsequent linearly polarized fs laser pulses, with the same laser configuration described above. The laser pulse train was set at a relatively low repetition rate of 0.5 Hz to identify each single pulse. Meanwhile, as to the read operation, we measured its real-time electrical read-out upon laser-pulse excitation, using a four-point TMR measurement and a fast-sampling oscilloscope, respectively. The complete measurements were performed without external magnetic field.

Time-resolved Kerr measurements

The TR-MOKE measurements were performed using a typical pump-probe configuration at a repetition rate of 100 kHz. In the measurements, the sample was first exposed by a pump pulse with a duration of 100 fs, a spot size of typically 35 µm and a laser-pulse energy of typically 600 nJ to write an AOS domain. Meanwhile, a probe pulse, which arrived at the sample with a different time delay and much lower laser energy, measures the time evolution of the magnetization via the Magneto-optic Kerr effect. The probe spot size was typically 12 µm for successful detection for OTJ pillars, integrating the magnetic signal over the full OTJ pillar element.

Due to the toggle switching behavior of the OTJ, an external magnetic field with an opposite direction was applied, which is slightly higher than the sample's coercive filed. This method is consistent with other time-resolved AOS studies[111,194]. A series of TR-MOKE measurements were averaged by using both positive and negative magnetic field direction. Data normalization was done based on the averaged magnetization Kerr signals in both positive and negative saturation states, which was extracted from the averaged TR-MOKE results for each pillar size.

6.5 Conclusion

We report an integrated spintronic-photonic OTJ device with picosecond switching speed, ultralow power, sufficiently high TMR, and nonvolatility. The device incorporates an all-optically switchable ferrimagnetic Co/Gd bilayer that is RKKY coupled to a CoFeB/MgO-based p-MTJ to ensure robust AOS, high TMR and PMA simultaneously. The all-optical toggle operation of the OTJ within 20 picoseconds is experimentally demonstrated, with a considerably high TMR of 34% for electrical read-out, and a low threshold laser fluence of 100 fJ/bit for efficient optical writing.

Our proof-of-concept OTJ device provides an essential milestone towards opto-MRAM arrays with ultrafast data access and ultralow power consumption. Additionally, by directly storing femtosecond optical information, it represents a new category of nonvolatile magneto-photonic memory, which extends the inherent advantage of photonics like data transfer and processing.

7

Conclusions and Outlook

In this chapter, general conclusions and perspectives of this thesis are provided. As discussed in earlier chapters, the integrated photonic-spintronic memory shows appealing technological advantages as to its picosecond speed and low energy dissipation, which are beyond state-of-the-art. Research efforts of this emerging field started from a material-orientated exploration on single-pulse AOS. Afterwards, by employing the AOS at the device level, several proof-of-concept demonstrations have been highlighted, including the picosecond "opto-MTJ" device that is explored in this thesis, as well as the aforementioned "on-the-fly" photonic racetrack memory. Future research trends in optimizing and exploiting these integrated spintronic-photonic platforms are summarized, together with possible routes towards a higher circuit/system level of integration.

7.1 General conclusions

As the building blocks of spintronic MRAMs, the p-MTJs allow fast nonvolatile data access, offering substantial potentials to revolutionize the mainstream computing architecture. However, conventional switching mechanisms of such devices are fundamentally hindered by spin polarized currents, either spin transfer torque or spin orbit torque with spin precession time limitation and excessive power dissipation. These physical constraints significantly stimulate the advancement of modern spintronics.

To overcome such bottlenecks, this thesis aims at the research and development of a "hybrid" spintronic-photonic memory technology *at the device level*. By integrating a fs laser with a spintronic MTJ, the proposed "opto-MTJ" device achieves a picosecond speed and a high energy efficiency.

The process compatibility of the MTJ with the AOS material system is investigated. The post-annealing effects on the all-optically switchable Pt/Co/Gd stacks are experimentally explored, revealing an enhanced AOS efficiency upon the required post-annealing temperature of the MTJ (300°C).

Integrating the HAMR technique with a high-performance p-DMTJ device is demonstrated. The data is read-out directly by TMR electrically, avoiding the fragile mechanical "read head". Typical operations of the proposed storage device are demonstrated, additionally, the synergy between the fs laser and the magnetic field is discussed.

Design of the free layer structure of the "opto-MTJ" is performed. Key characteristics of merits include a deterministic AOS, a high TMR ratio, and a high PMA. Based on systematic measurements, a composite structure, which incorporates an all-optically switchable ferrimagnetic Co/Gd bilayer coupled to a ferromagnetic CoFeB/MgO system by the RKKY interaction, could meet all the aforementioned requirements, thus highly suitable for MTJ integration.

The fabrication and characterization of the "opto-MTJ" device are reported. The device employs the Gd/Co/Ta/CoFeB/MgO structure into a full MTJ device. As to the "read"/"write" performance, it shows a considerably high TMR ratio ($\approx$ 34%) and high energy efficiency. More importantly, a picosecond all-optical operation is explicitly confirmed by time-resolved measurements, with promising scalability as well. The proof-of-concept device represents an essential step towards a new category of ultrafast spintronic memory with photonic integration.

As to the technological implications, it could lead to large-scale "opto-MRAM" arrays, within the scope of a THz memory/computing architecture. Additionally, by direct transfer of femtosecond optical information into magnetic memory, it represents a non-volatile photonic memory, extending the inherent advantage of photonics like data transfer and processing.

From a more fundamental viewpoint, the proposed "opto-MTJ" offers a unique playground for further fundamental studies on the interdisciplinary field merging spintronics and photonics. Thus, it exhibits great potential to stimulate the innovation of future & emerging technologies, A more detailed outlook will be briefly discussed in the following.

7.2 Outlook and perspectives

The proposed "opto-MTJ" represents a versatile platform in the field of spintronic-photonic integration. To access these possible application scenarios described in Section 7.1, further design requirements and possible routes for the "opto-MTJ" device are of crucial relevance, leading to several next-level scientific objectives. In the following, we will discuss them from several different aspects.

Downscaling issues

One of the prominent challenges is the downscaling of the "opto-MTJ" towards nanometer dimensions, which is constrained by the laser spot size due to diffraction limit (typically on the order of laser wavelength).

A possibly effective route is to exploit plasmonic antennas[195,196] to focus laser spot substantially beyond the diffraction limit (down to 10 – 100 nanometer scale), and write the memory bit. This technique has already been well-developed in the HAMR technology[19,181,197], by reducing laser spot below 40 nm, and locally heating the magnetic disc. Due to the purely thermal nature of the single-pulse AOS, the plasmonic technique could be well implemented in an "opto-MTJ" device, resulting in nanoscale confinement of all-optical "write".

Integrating plasmonics-based approaches with the "opto-MTJ" device might be of great technological relevance for future photonic-spintronic integration. The feasibility of this idea has been demonstrated using gold two-wire antennas placed on a RE-TM film[107]. Nevertheless, future research efforts are highly required, with an emphasis on implementing such plasmonic structures to operate a nanoscale spintronic device[198].

Ultimate data rate

Exploring the ultimate data rates of the "opto-MTJ" is another important trend for future research, aiming at high-speed data processing. Although the picosecond "write" speed has been demonstrated, the applicability of this technology is dominated by the repetition rate of the two succeeding "write" operations, i.e., the data rate.

Very recently, first attempts on the ultimate repetition rate of AOS on a RE-TM film have been investigated by dual-shot time-resolved studies in a stroboscopic manner, resulting in a repetition rate of up to 3 GHz ($\approx$ 300 ps)[199]. However, determining the maximum data rate of the "opto-MTJ", is still an unexplored scientific question.

Picosecond laser/current-induced writing

For real applications, a highly sophisticated fs laser would become a major drawback. Thus, it would be more technologically favourable to trigger AOS by picosecond laser pulses, due to the flexibility and low cost towards on-chip applications.

The rapid development of single-pulse AOS in RE-TM films using ps laser pulses (with a duration up to 10 ps) has been witnessed[100,200], which is much longer than the timescale (1 ps) of ultrafast heating of electrons (i.e., electron-phonon interaction).

As on-chip sub-10-ps current pulses are possible in conventional CMOS electronics, it may be highly interesting to implement ultrafast on-chip "opto-MTJ" devices. Such picosecond electrical pulses could be generated by Auston photo-switches, which have been demonstrated to reverse the magnetization of a GdFeCo thin film efficiently by Yang *et al.*[103].

By integrating this technique with an "opto-MTJ", this research line would open up a new frontier for ultrafast charge current-driven spintronic devices, which is orders of magnitude faster than any electrical schemes based on spin polarized current, highly promising for on-chip MRAM applications.

Skyrmions in the "opto-MTJ"

The "opto-MTJ" device might represent a versatile platform to fuel future fundamental research on ultrafast spintronics, leading to highly original applications as well. As a prominent example, a novel idea, an *"opto-skyrmion-MTJ"*, is also in the air.

Magnetic skyrmions are topologically stable, particle-like chiral spin textures, which are highly promising as information carriers in spintronic devices, because of their nano-sized dimensions and superior stability[160,171]. As to a table-top realization of a skyrmion-based device, one major challenge is an efficient electrical approach to detect skyrmions, rather than using highly sophisticated microscopy techniques.

In this context, the "opto-MTJ" may offer a unique physical playground for creating skyrmion in its free layer, manipulating by fs laser pulses, as well as detecting simply by electrical approaches. This idea has also been supported by several theoretical works[201,202], which may empower the fundamental research on skyrmion-electronics, especially their laser-induced dynamics.

Another challenge for such a *"opto-skyrmion-MTJ"* is the fast and controllable generation of skyrmions. Among them, fs laser-induced approaches might open up enormous possibilities, as initiated in Je *et al.*[163] using a ferromagnetic thin film. This new device might find application in artificial synapse, since the synaptic weights could represent by creating clusters of skyrmions in the laser spot region and read-out electrically.

In the following, future research trends of all-optical switching from a material perspective are highlighted.

Rare-earth-free AOS material platform of the "opto-MTJ"

As to materials that host single-pulse AOS, until now, it seems that rare earth elements (Gd, Tb) are key elements, although the in-depth reason for it is still unknown. This partly reflects that more insights into the underlying physical process of AOS, such as exchange scattering and the role of spin current, are still highly needed.

Beyond RE-TM ferrimagnets, exploring other rare-earth-free materials with all-optical toggle switching phenomena is clearly of both fundamental and technological interest. Among them, half-metallic compensated Heusler alloy MnRuGa has been revealed to host single-pulse AOS, which extends the spectrum of the AOS material family[203,204].

Besides, exploration on the nonthermal switching of magnetic dielectric materials has been initiated[205,206], offering a distinctive route toward highly efficient AOS. Another noteworthy trend relates to AOS of antiferromagnets[207,208], which is triggered by the recent advances in antiferromagnetic spintronics[209,210]. However, all these new material platforms for AOS seem to face challenges upon integrating with spintronic devices, thus requiring future research to validate its real applicability.

Enhancing domain wall velocity in synthetic ferrimagnetic multilayers

Synthetic ferrimagnetic Pt/Co/Gd stacks are heavily explored in the "opto-MRAM" device proposed in this thesis, because of the efficient single-pulse AOS and the ease of interface engineering. In addition, they show superior compatibility with spintronic functionalities, such as SHE-induced DW motion and interfacial DMI, extending its potential as a versatile platform for merging spintronics and photonics.

In this framework, another prominent trend relates to integrating AOS with Race-Track Memories, which is discussed in detail in Section 2.2.3. Clearly, in such a device, a high DW velocity is required to achieve high-speed data transport. Towards this objective, it was recently shown that the DW velocity in the Co/Gd bilayer would enhance significantly when the angular momentum in the Co layer and the Gd are fully compensated[211].

This idea points towards further optimization of the "on-the-fly racetrack", where the magnetic properties can be simply modified by simply tuning the thicknesses of each layer during magnetron sputtering. Another strategy has also been initiated[135], which employed the Pt/SAF/Gd stack. An enhanced DW velocity was measured upon compensated magnetizations of the FM layers in the SAF.

Lastly, we will highlight several preliminary ideas, aiming at future photonic integration from a circuit perspective.

Possible routes towards PIC integration: an "opto-MRAM" chip

Aiming at a real "opto-MRAM" chip, the next-level scientific challenge is to implement the "opto-MTJ" into photonic integrated circuits (PIC). As to random access of the magnetic bit in the "opto-MRAM" array, an all-optical approach is envisioned based on photonic waveguides, which could be physically realized by some well-matured integrated photonic platforms, such as SiN and InP, etc., thus providing access to different application domains.

Specifically, the memory bit is set at the intersection of the cross-arranged optical waveguide arrays. These waveguides are used as the word lines and the bit lines to concurrently address the "opto-MTJ" bits, which are controlled by a tunable delay line. Only the simultaneous arrival of the two laser pulses would provide enough energy to switch the selected OTJ, as similar in the Stoner-Wolfarth MRAM design as shown in Fig. 1.4, although the energy loss would become a significant issue.

Another scheme to selectively address each memory bit is envisioned, namely, a wavelength-division multiplexing (WDM) scheme[7]. As similar in the WDM communication, the addressing lines are selected by different laser wavelengths. However, this scheme requires ps pulses from multiple lasers with different wavelengths to establish AOS.

In the forthcoming decades, more exciting insights related to the convergence of spintronics and photonics will probably become a new research line. As a spin-off technology in prospect, it would be of technological importance to build a hybrid (photonic and electronic) integrated circuit platform, which is fully compatible with the mainstream fabrication process. Ultimately, this technology would probably lead towards real-world "opto-MRAM" memory chip applicaitons.

Summary

Picosecond Spintronic Memory with Photonic Integration

As the most promising "universal" memory, spintronic MRAM technology is highly competitive towards next-generation computing architecture with non-von Neumann hierarchy. As the basic memory bit of an MRAM, two generations of magnetic tunnel junctions (MTJs) have been developed over the past 25 years, aiming at a high access speed with low power consumption.

Briefly, the "MRAM 1G" was based on magnetic field-induced switching, which has been commercialized by Everspin since 2006. Later, to alleviate the scalability and dissipation issues, the "MRAM 2G" employing spin- polarized current-induced schemes has become a topical research field, such as investigating concepts like spin transfer torque (STT). Unfortunately, constrained by the spin precession process, the operation speed of MRAMs is still fundamentally constrained by a sub-nanosecond speed limitation, along with excessive current densities. These serious bottlenecks have remained a long-lasting vital challenge for the spintronic industry.

To address these issues, integrating a femtosecond laser, i.e., the fastest stimulus commercially available, with spintronic MRAMs has emerged as a competitive route toward the "MRAM 3G" design. Recently, single-fs-pulse all-optical switching (AOS) has been observed in synthetic ferrimagnetic Pt/Co/Gd multilayers. Stimulated by this ultrafast and efficient AOS scheme, writing a spintronic MTJ device by femtosecond laser has been envisioned, which was predicted to offer $1-2$ orders of magnitude faster speed, with a low dissipation. However, until now, such a device hasn't been experimentally demonstrated yet, which has been regarded as one of the major scientific goals in the photonic-spintronic technology. Key scientific issues related to process compatibility, exploration of material systems, and novel physical mechanisms, still need to be solved, which constitute the integral parts of this thesis.

The key highlight of this thesis is to demonstrate a non-volatile opto-spintronic memory device with a world-record speed, by uing a fs laser. The proposed opto-spintronic tunnel junction (OTJ) device shows a picosecond writing speed with high efficiency, and is solely operated by a femtosecond laser. In this thesis, we report the design, fabrication, and characterization of such a device.

To investigate the process compatibility of the MTJ with the synthetic ferrimagnetic multilayers, the post-annealing effects on the all-optically switchable Pt/Co/Gd stacks is experimentally explored. The results show that the AOS efficiency is considerably enhanced upon annealing up to 300°C, which is a required temperature condition for MTJ fabrication. In addition, a significant enhancement of domain wall velocity upon annealing is also observed. These results demonstrate that the synthetic ferrimagnetic Pt/Co/Gd system is an ideal candidate for integrating AOS with spintronic devices, leading towards the ultrafast opto-spintronics memory.

Next, a heat-assisted magnetic recording (HAMR) technique is employed in a high-performance p-MTJ device. Although HAMR has been widely used in ultra-high-density magnetic storage, the data access is achieved by a mechanical "read head", resulting in an unfavorable speed limitation. By integrating HAMR with p-MTJ, a direct electrical TMR readout in real time is enabled. The binary "write" and unidirectional "reset" operations were demonstrated. The joint effect between the fs laser and the magnetic field was further explored, leading to a switching phase diagram. The results show the feasibility of a HAMR-p-MTJ device, which represents a first step towards high-density opto-spintronic data storage.

Afterwards, research efforts on exploring an ideal free-layer system of the OTJ are summarized, aiming at i.) a robust single-pulse AOS, ii.) a high TMR, and iii.) a high PMA, simultaneously. In the design of Gd/CoFeB/MgO, the CoFeB/MgO interface would lead to a high TMR. However, energy-dependent AOS measurements show that its AOS window is extremely narrow, which is partly attributed to the heat diffusion. In contrast, in the design of Gd/Co/Ta/CoFeB/MgO, where the Co and CoFeB are ferromagnetically coupled through an atom-thick Ta spacer, a significantly broader AOS window is observed, as well as a high TMR and PMA. As a result, such a composite free-layer structure is highly suitable in the OTJ device, which may offer a conventional design route for other opto-spintronic devices.

Lastly, we report on the fabrication and characterization of a fully-functional OTJ device. By a careful stack design, the composite OTJ incorporates an all-optically switchable Co/Gd bilayer coupled to a CoFeB/MgO-based p-MTJ by the Ruderman-Kittel-Kasuya-Yosida interaction. We demonstrate, i). deterministic and efficient all-optical "write" operation, by electrical TMR read-out; ii). picosecond operation speed, characterized by ultrafast time-resolved measurements; and iii). integration with state-of-the-art MTJ performance, and fully compatible fabrication progress. This proof-of-concept device represents an important progress towards a new category of spintronic memories, achieving a picosecond speed by using photonic integration.

In summary, this thesis demonstrates the *R&D* of a fully-functional picosecond OTJ device, with appealing technological performance as to speed and efficiency. As a unique non-volatile photonic memory, it enables direct responses of optical stimulus to magnetic information, which would inspire emerging fields like photonic neuromorphic computing. Moreover, the experimental results represent an important advance to fuel further fundamental scientific studies regarding the interaction between spintronics and photonics.

Curriculum Vitae

Luding WANG was born on February 27, 1993 in China. He studied Electronic Engineering at Wuhan University (one of the top 10 universities in China, QS 225) during 09/2011 – 09/2015. He performed a BEP project in the Key Laboratory of Geospace Environment and Geodesy, Ministry of Education, China. He was awarded the Undergraduate Alumni Scholarship by Wuhan University in 2015, and obtained his Bachelor of Engineering degree.

Luding continued his Master's studies at the University of Chinese Academy of Sciences (CAS), Beijing, where he started scientific research in the field of Ultrafast Photonics. In 2016, he carried out a 2-year external traineeship at the CAS Key Laboratory of Time and Frequency Primary Standards. During this MEP project, he experimentally set up a high-performance femtosecond fiber laser system, using a novel "hybrid" mode locking schemes. He was awarded as an Outstanding Early Career Member in CAS in 05/2018, and obtained his Master of Science degree in 09/2018.

After graduation, Luding started his PhD studies at Beihang University, Beijing. His PhD project is facilitated by the Key Laboratory of Spintronics, Ministry of Industry and Information Technology, China. Supervised by prof.dr. Weisheng ZHAO, he extended his research topic to spintronic memories, aiming to address their speed bottleneck by using ultrafast photonic approaches.

In 01/2019, Luding was selected as a candidate for a Double Doctorate PhD project between Beihang University and Eindhoven University of Technology. During 01/06/2019 – 15/04/2021, Luding secured funding from the Chinese Scholarship Council (CSC) (EUR 25000, 18 months), and the International Excellent

ESR Exchange Program (EUR 6000, 3 months) of China Association of Science and Technology.

With these financial supports, Luding studied as a double PhD candidate in the group Physics of Nanostructures, Department of Applied Physics, Eindhoven University of Technology, The Netherlands. His double PhD project was supervised by prof.dr. B. Koopmans. By integrating Spintronics with Ultrafast Photonics, the core output of the thesis is a picosecond non-volatile photonic memory that is solely operated by femtosecond laser pulses. The main results of this PhD project are presented in this thesis.

As a part-time work, Luding served as a permanent secretary in the semiconductor professional committee alumni of his alma mater. Besides his professional work, he likes Chinese tea arts and home cuisines. He also likes to listen to podcasts. During vacations, he enjoys road trips and sightseeing all over the world, or simply staying at home with his family and friends.

Publications

1. **L. Wang**, C. Cheng, P. Li, Y. L. W. van Hees, Y. Liu, K. Cao, R. Lavrijsen, X. Lin, B. Koopmans, and W. Zhao, *Picosecond Optospintronic Tunnel Junctions*, Proceedings of the National Academy of Sciences (2021) (submitted)

2. **L. Wang**, Y. L. W. van Hees, R. Lavrijsen, W. Zhao, and B. Koopmans, *Enhanced all-optical switching and domain wall velocity in annealed synthetic-ferrimagnetic multilayers*, Applied Physics Letters **117**, 022408 (2020)

3. **L. Wang**, W. Cai, K. Cao, K. Shi, B. Koopmans, and W. Zhao, *Femtosecond Laser-Assisted Switching in Perpendicular Magnetic Tunnel Junctions with Double-Interface Free Layer*, Science China Information Sciences (2021)

4. **L.Wang**, Y. Zhang, B. Rao, H. Jiang, and S. Zhang *Experimental study on hybrid femtosecond erbium-doped fiber laser*, Journal of Time and Frequency (2018)

5. **L. Wang**, R. Lavrijsen, X. Lin, B. Koopmans, and W. Zhao, *The role of heat diffusion in all-optical switching of Gd/CoFeB/MgO multilayers*, (2021) (in preparation)

6. **L. Wang**, C. Cheng, P. Li, Y. L. W. van Hees, Y. Liu, K. Cao, R. Lavrijsen, X. Lin, B. Koopmans, and W. Zhao, *Picosecond Optospintronic Tunnel Junctions*, National Science Review (2021) (submitted)

Acknowledgements

By the end of the thesis, I'd like to take this opportunity to thank all the people who helped me, supported me, and inspired me. This PhD project would have been even more challenging without the contribution of those nice people.

I would like to start with my appreciation to my promotors, prof.dr. Weisheng Zhao and prof.dr. Bert Koopmans. Weisheng, you will always be my role model of my work and life. Thank you for the support and trust throughout my PhD. As my supervisor, I highly appreciate every valuable platform you offered to your student, and your broad vision from an interdisciplinary viewpoint. As my leader, your high-level skills in organizing and cooperation always inspire me a lot. I'm also inspired by your style of speech and presentation. As my respectful friend, I highly admire your wisdom, kindness, and patience, beyond the scientific research itself.

Now, I would like to express my sincere gratitude to Bert. Thank you for giving me the opportunity to join the group of FNA, and the great supervision on my PhD thesis. Your passionate way of research and sports, and your broad knowledge of physics, have always motivated me significantly. As a charming gentleman, you are also my idol beyond physics itself. I very much appreciate the bi-weekly supervisory meeting we had in the last two years (especially after I returned to China six months ago); it's always been a valuable encouragement during my difficult days. I also want to acknowledge you, for carefully reading all my first drafts, and offering helpful feedbacks all the time. It's a very nice experience to be your student and employee.

I would like to appreciate my copromotor, dr.ir.Reinoud Lavrijsen. Your enthusiasm for science has definitely encouraged me all my way during my PhD. Your immense knowledge in the lab has been a valuable navigator for me. Thanks for showing me around in the group the first day I came, and introducing me to the members of FNA. It's always a pleasure to join the group meeting you host. I am highly grateful for the timely and detailed feedback you provided on my manuscripts and experiments. Thanks for reading my thesis even during an air trip. It's always a nice experience working with you.

Thanks to all the other members from the promotiecommissie: prof.dr. Andrea Fiore, prof.dr. Cong Wang, prof.dr. Eric Fullerton, prof.dr. Tianxiao Nie and dr. Dafiné Ravelosona. Thanks for your valuable time and consideration on my thesis.

Then, I would like to thank all the members in the FNA group. Thanks for all the discussions, memories, and laughs, that have made my PhD an enjoyable time. Special thanks to Karin for all the help on administrative issues. Thanks to Jeroen and Gerrie, for all the technical support on my measurements, as well as for instructing me how to operate those complex machines patiently. Thank you, Thomas and Sjoerd, for sharing the same office with me, and always being willing to help. Thanks to Pingzhi, Jianing, and Zilu, for your all kinds of supports, and for our friendship. I enjoyed all the discussions, laughs, chat, parties, and trips with you along my PhD journey.

Besides, I'd like to acknowledge Youri and Mark Peeters, for helping me with everything in the laser lab. Thanks to Chris, for our friendship and the nice trip in Beijing, I also appreciate the campus tour you offered on the first day I came here. During my stay, I had an opportunity to supervise one BEP student, Joep, thank you for your efforts, it was also a valuable teaching experience for me. I would also like to thank Maarten, Mark de Jong, Tom, Mariëlle, Adrien, Casper, Tunc, Ece... Many names and smiling faces leave in my mind, thank you all for the timely help and pleasant discussions during my stay in FNA.

It's also a rewarding experience as a member in Weisheng's group. To Daoqian, Xiaoxuan, Xueying, Hongchao, Boyu, Jialiang, Shaohua, Danrong, Yong, Chen, Jiaqi, Xinran, Kewen, Shouzhong, Sai, Zongxia, Ao, Houyi, Runze, Anni, Kaihua,

and Wenlong…, for all the collaboration and help (either in research or in daily life) on my project.

This project offered me a valuable opportunity to meet the international spintronic community, and make connections all over the world. I highly cherish this aspect. Particularly, I'd like to acknowledge prof.dr. Stuart Parkin from Max Planck Institute, for the fruitful discussion and inspiring ideas on this project. I'm grateful to dr. Sebastien Couet from IMEC, for the valuable suggestions on my career. I also appreciate prof.dr. Mairbek Chshiev and dr. Liliana Prejbeanu for the pleasant conversations during the ESSON summer school in Grenoble.

I acknowledge prof.dr. Martijn Heck and dr. Jos van der Tol from the department of electrical engineering , for all the inspiring discussion we had, aiming to advance this technology even further. Thanks to Martijn for introducing me to the frontier of the integrated photonics, and all the brain-storming ideas. It's my great pleasure to work in the Photonic integration group.

I'd also like to thank my friends and teachers outside academia. During my internship in an IC manufacture company, I particularly thank my leader, Joe, for offering me many insights in the semiconductor industry, and the unreserved guidance on process/device TCAD. As a permanent secretary in the semiconductor alumina committee in my alma mater, I always find it pleasant to work with you, and always be inspired.

I would like to thank my family, for all the love and care. I feel so lucky to live in a lovely and peaceful household. Thanks for tolerating my occasional stubbornness in daily life. Thank you for being there when I get success, or when I suffer challenges.

Finally, I'd like to end this thesis with a quote on the hallway between Flux and Cascade. It's actually the most inspiring philosophy TU/Eindhoven has taught me in the past years:

Science is organized knowledge; wisdom is organized life. – Immanuel Kant.

Bibliography

[1] S. Bader and S. Parkin, Spintronics, Annual Review of Condensed Matter Physics **1**, 71 (2010).

[2] I. Žutić, J. Fabian, and S. D. Sarma, Spintronics: Fundamentals and applications, Reviews of Modern Physics **76**, 323 (2004).

[3] C. Chappert, A. Fert, and F. N. V. Dau, The emergence of spin electronics in data storage, Nature Materials **6**, 813 (2007).

[4] S. A. Wolf, J. Lu, M. R. Stan, E. Chen, and D. M. Treger, The promise of nanomagnetics and spintronics for future logic and universal memory, Proceedings of the IEEE **98**, 2155 (2010).

[5] A. D. Kent and D. C. Worledge, A new spin on magnetic memories, Nature Nanotechnology **10**, 187 (2015).

[6] B. Dieny, I. L. Prejbeanu, K. Garello, P. Gambardella, P. Freitas, R. Lehndorff, W. Raberg, U. Ebels, S. O. Demokritov, J. Akerman, A. Deac, P. Pirro, C. Adelmann, A. Anane, A. V. Chumak, A. Hirohata, S. Mangin, S. O. Valenzuela, M. C. Onbaşlı, M. d'Aquino, G. Prenat, G. Finocchio, L. Lopez-Diaz, R. Chantrell, O. Chubykalo-Fesenko, and P. Bortolotti, Opportunities and challenges for spintronics in the microelectronics industry, Nature Electronics **3**, 446 (2020).

[7] A. V. Kimel and M. Li, Writing magnetic memory with ultrashort light pulses, Nature Reviews Materials **4**, 189 (2019).

[8] C. D. Stanciu, F. Hansteen, A. V. Kimel, A. Kirilyuk, A. Tsukamoto, A. Itoh, and T. Rasing, All-optical magnetic recording with circularly polarized light, Physical Review Letters **99**, 047601 (2007).

[9] D. E. Nikonov and I. A. Young, Overview of beyond-CMOS devices and a uniform methodology for their benchmarking, Proceedings of the IEEE **101**, 2498 (2013).

[10] T. Skotnicki, J. Hutchby, T. King, H.-S. Wong, and F. Boeuf, The end of CMOS scaling, IEEE Circuits and Devices Magazine **21**, 16 (2005).

[11] S. Asai, Semiconductor memory trends, Proceedings of the IEEE **74**, 1623 (1986).

[12] C. S. Hwang, Prospective of semiconductor memory devices: from memory system to materials, Advanced Electronic Materials **1**, 1400056 (2015).

[13] A. Chung, J. Deen, J.-S. Lee, and M. Meyyappan, Nanoscale memory devices, Nanotechnology **21**, 412001 (2010).

[14] V. V. Zhirnov, R. K. Cavin, S. Menzel, E. Linn, S. Schmelzer, D. Brauhaus, C. Schindler, and R. Waser, Memory devices: Energy–space–time tradeoffs, Proceedings of the IEEE **98**, 2185 (2010).

[15] U. Hasson, J. Chen, and C. J. Honey, Hierarchical process memory: memory as an integral component of information processing, Trends in Cognitive Sciences **19**, 304 (2015).

[16] J. Chang, Nonvolatile semiconductor memory devices, Proceedings of the IEEE **64**, 1039 (1976).

[17] L. Wang, C.-H. Yang, and J. Wen, Physical principles and current status of emerging non-volatile solid state memories, Electronic Materials Letters **11**, 505 (2015).

[18] A. Chen, A review of emerging non-volatile memory (NVM) technologies and applications, Solid-State Electronics **125**, 25 (2016).

[19] M. Kryder, E. Gage, T. McDaniel, W. Challener, R. Rottmayer, G. Ju, Y.-T. Hsia, and M. Erden, Heat assisted magnetic recording, Proceedings of the IEEE **96**, 1810 (2008).

[20] R. Bez, E. Camerlenghi, A. Modelli, and A. Visconti, Introduction to flash memory, Proceedings of the IEEE **91**, 489 (2003).

[21] C.-Y. Lu, K.-Y. Hsieh, and R. Liu, Future challenges of flash memory technologies, Microelectronic Engineering **86**, 283 (2009).

[22] D. Weller, G. Parker, O. Mosendz, E. Champion, B. Stipe, X. Wang, T. Klemmer, G. Ju, and A. Ajan, A HAMR media technology roadmap to an areal density of 4 Tb/in^2, IEEE Transactions on Magnetics **50**, 1 (2014).

[23] A. Chen, *Emerging nanoelectronic devices* (Wiley, Chichester, West Sussex, United Kingdom, 2014).

[24] D. Frank, R. Dennard, E. Nowak, P. Solomon, Y. Taur, and H.-S. P. Wong, Device scaling limits of si MOSFETs and their application dependencies, Proceedings of the IEEE **89**, 259 (2001).

[25] R. K. Cavin, P. Lugli, and V. V. Zhirnov, Science and engineering beyond moore's law, Proceedings of the IEEE **100**, 1720 (2012).

[26] N. S. Kim, T. Austin, D. Blaauw, T. Mudge, K. Flautner, J. S. Hu, M. Irwin, M. Kandemir, and V. Narayanan, Leakage current: Moore's law meets static power, Computer **36**, 68 (2003).

[27] A. Makarov, T. Windbacher, V. Sverdlov, and S. Selberherr, CMOS-compatible spintronic devices: a review, Semiconductor Science and Technology **31**, 113006 (2016).

[28] A. Makarov, V. Sverdlov, and S. Selberherr, Emerging memory technologies: Trends, challenges, and modeling methods, Microelectronics Reliability **52**, 628 (2012).

[29] X. Zou, S. Xu, X. Chen, L. Yan, and Y. Han, Breaking the von neumann bottleneck: architecture-level processing-in-memory technology, Science China Information Sciences **64**, 160404 (2021).

[30] S. Gupta, M. Imani, and T. Rosing, FELIX: fast and energy-efficient logic in memory, in *Proceedings of the International Conference on Computer-Aided Design* (ACM, 2018).

[31] H.-S. P. Wong and S. Salahuddin, Memory leads the way to better computing, Nature Nanotechnology **10**, 191 (2015).

[32] H. Akinaga and H. Shima, Resistive random access memory (ReRAM) based on metal oxides, Proceedings of the IEEE **98**, 2237 (2010).

[33] T.-C. Chang, K.-C. Chang, T.-M. Tsai, T.-J. Chu, and S. M. Sze, Resistance random access memory, Materials Today **19**, 254 (2016).

[34] H.-S. P. Wong, S. Raoux, S. Kim, J. Liang, J. P. Reifenberg, B. Rajendran, M. Asheghi, and K. E. Goodson, Phase change memory, Proceedings of the IEEE **98**, 2201 (2010).

[35] D. Apalkov, B. Dieny, and J. M. Slaughter, Magnetoresistive random access memory, Proceedings of the IEEE **104**, 1796 (2016).

[36] Y. Lu, T. Zhong, W. Hsu, S. Kim, X. Lu, J. J. Kan, C. Park, W. C. Chen, X. Li, X. Zhu, P. Wang, M. Gottwald, J. Fatehi, L. Seward, J. P. Kim, N. Yu, G. Jan, J. Haq, S. Le, Y. J. Wang, L. Thomas, J. Zhu, H. Liu, Y. J. Lee, R. Y. Tong, K. Pi, D. Shen, R. He, Z. Teng, V. Lam, R. Annapragada, T. Torng, P.-K. Wang, and S. H. Kang, Fully functional perpendicular STT-MRAM macro embedded in 40 nm logic for energy-efficient IOT applications, in *2015 IEEE International Electron Devices Meeting (IEDM)* (IEEE, 2015).

[37] M. Wuttig, Towards a universal memory?, Nature Materials **4**, 265 (2005).

[38] M. N. Baibich, J. M. Broto, A. Fert, F. N. V. Dau, F. Petroff, P. Etienne, G. Creuzet, A. Friederich, and J. Chazelas, Giant magnetoresistance of (001)Fe/(001)Cr magnetic superlattices, Physical Review Letters **61**, 2472 (1988).

[39] G. Binasch, P. Grünberg, F. Saurenbach, and W. Zinn, Enhanced magnetoresistance in layered magnetic structures with antiferromagnetic interlayer exchange, Physical Review B **39**, 4828 (1989).

[40] E. E. Fullerton and I. K. Schuller, The 2007 nobel prize in physics: Magnetism and transport at the nanoscale, ACS Nano **1**, 384 (2007).

[41] S. Parkin, X. Jiang, C. Kaiser, A. Panchula, K. Roche, and M. Samant, Magnetically engineered spintronic sensors and memory, Proceedings of the IEEE **91**, 661 (2003).

[42] W. J. Gallagher and S. S. P. Parkin, Development of the magnetic tunnel junction MRAM at IBM: From first junctions to a 16-Mb MRAM demonstrator chip, IBM Journal of Research and Development **50**, 5 (2006).

[43] P. P. Freitas, R. Ferreira, and S. Cardoso, Spintronic sensors, Proceedings of the IEEE **104**, 1894 (2016).

[44] P. P. Freitas, F. A. Cardoso, V. C. Martins, S. A. M. Martins, J. Loureiro, J. Amaral, R. C. Chaves, S. Cardoso, L. P. Fonseca, A. M. Sebastião, M. Pannetier-Lecoeur, and C. Fermon, Spintronic platforms for biomedical applications, Lab Chip **12**, 546 (2012).

[45] J. Alzate, P. Hentges, R. Jahan, A. Littlejohn, M. Mainuddin, D. Ouellette, J. Pellegren, T. Pramanik, C. Puls, P. Quintero, T. Rahman, U. Arslan, M. Sekhar, B. Sell, M. Seth, A. J. Smith, A. K. Smith, L. Wei, C. Wiegand, O. Golonzka, F. Hamzaoglu, P. Bai, J. Brockman, Y. J. Chen, N. Das, K. Fischer, T. Ghani, and P. Heil, 2 MB array-level demonstration of STT-MRAM process and performance towards L4 cache applications, in *2019 IEEE International Electron Devices Meeting (IEDM)* (IEEE, 2019).

[46] C. Lin, S. Kang, Y. Wang, K. Lee, X. Zhu, W. Chen, X. Li, W. Hsu, Y. Kao, M. Liu, W. Chen, Y. Lin, M. Nowak, N. Yu, and L. Tran, 45nm low power CMOS logic compatible embedded STT MRAM utilizing a reverse-connection 1T/1MTJ cell, in *2009 IEEE International Electron Devices Meeting (IEDM)* (IEEE, 2009).

[47] S. Ikeda, J. Hayakawa, Y. M. Lee, F. Matsukura, Y. Ohno, T. Hanyu, and H. Ohno, Magnetic tunnel junctions for spintronic memories and beyond, IEEE Transactions on Electron Devices **54**, 991 (2007).

[48] S. S. P. Parkin, C. Kaiser, A. Panchula, P. M. Rice, B. Hughes, M. Samant, and S.-H. Yang, Giant tunnelling magnetoresistance at room temperature with MgO (100) tunnel barriers, Nature Materials **3**, 862 (2004).

[49] T. Miyazaki and N. Tezuka, Giant magnetic tunneling effect in Fe/Al_2O_3/Fe junction, Journal of Magnetism and Magnetic Materials **139**, L231 (1995).

[50] G. A. Prinz, Magnetoelectronics, Science **282**, 1660 (1998).

[51] M. Julliere, Tunneling between ferromagnetic films, Physics Letters A **54**, 225 (1975).

[52] W. ZHAO, Z. WANG, S. PENG, L. WANG, L. CHANG, and Y. ZHANG, Recent progresses in spin transfer torque-based magnetoresistive random access memory (STT-MRAM), SCIENTIA SINICA Physica, Mechanica & Astronomica **46**, 107306 (2016).

[53] R. Meservey, P. M. Tedrow, and P. Fulde, Magnetic field splitting of the quasiparticle states in superconducting aluminum films, Physical Review Letters **25**, 1270 (1970).

[54] E. Y. Tsymbal, O. N. Mryasov, and P. R. LeClair, Spin-dependent tunnelling in magnetic tunnel junctions, Journal of Physics: Condensed Matter **15**, R109 (2003).

[55] J. S. Moodera, L. R. Kinder, T. M. Wong, and R. Meservey, Large magnetoresistance at room temperature in ferromagnetic thin film tunnel junctions, Physical Review Letters **74**, 3273 (1995).

[56] W. H. Butler, X.-G. Zhang, T. C. Schulthess, and J. M. MacLaren, Spin-dependent tunneling conductance of Fe|MgO|Fe sandwiches, Physical Review B **63**, 054416 (2001).

[57] J. Mathon and A. Umerski, Theory of tunneling magnetoresistance of an epitaxial Fe/MgO/Fe(001) junction, Physical Review B **63**, 220403 (2001).

[58] S. Yuasa, T. Nagahama, A. Fukushima, Y. Suzuki, and K. Ando, Giant room-temperature magnetoresistance in single-crystal Fe/MgO/Fe magnetic tunnel junctions, Nature Materials **3**, 868 (2004).

[59] H. Zhao, A. Lyle, Y. Zhang, P. K. Amiri, G. Rowlands, Z. Zeng, J. Katine, H. Jiang, K. Galatsis, K. L. Wang, I. N. Krivorotov, and J.-P. Wang, Low writing energy and sub nanosecond spin torque transfer switching of in-plane magnetic tunnel junction for spin torque transfer random access memory, Journal of Applied Physics **109**, 07C720 (2011).

[60] H. Yamamoto, J. Hayakawa, K. Miura, K. Ito, H. Matsuoka, S. Ikeda, and H. Ohno, Dependence of magnetic anisotropy in cofeb free layers on capping layers in MgO-based magnetic tunnel junctions with in-plane easy axis, Applied Physics Express **5**, 053002 (2012).

[61] E. Chen, D. Apalkov, Z. Diao, A. Driskill-Smith, D. Druist, D. Lottis, V. Nikitin, X. Tang, S. Watts, S. Wang, S. A. Wolf, A. W. Ghosh, J. W. Lu, S. J. Poon, M. Stan, W. H. Butler, S. Gupta, C. K. A. Mewes, T. Mewes, and P. B. Visscher, Advances and future prospects of spin-transfer torque random access memory, IEEE Transactions on Magnetics **46**, 1873 (2010).

[62] S. Bhatti, R. Sbiaa, A. Hirohata, H. Ohno, S. Fukami, and S. Piramanayagam, Spintronics based random access memory: a review, **20**, 530 (2017).

[63] K. C. Chun, H. Zhao, J. D. Harms, T.-H. Kim, J.-P. Wang, and C. H. Kim, A scaling roadmap and performance evaluation of in-plane and perpendicular MTJ based STT-MRAMs for high-density cache memory, IEEE Journal of Solid-State Circuits **48**, 598 (2013).

[64] B. Dieny and M. Chshiev, Perpendicular magnetic anisotropy at transition metal/oxide interfaces and applications, Reviews of Modern Physics **89**, 025008 (2017).

[65] H. X. Yang, M. Chshiev, B. Dieny, J. H. Lee, A. Manchon, and K. H. Shin, First-principles investigation of the very large perpendicular magnetic anisotropy at Fe|MgO and Co|MgO interfaces, Physical Review B **84**, 054401 (2011).

[66] S. Ikeda, K. Miura, H. Yamamoto, K. Mizunuma, H. D. Gan, M. Endo, S. Kanai, J. Hayakawa, F. Matsukura, and H. Ohno, A perpendicular-anisotropy CoFeB–MgO magnetic tunnel junction, Nature Materials **9**, 721 (2010).

[67] M. T. Johnson, P. J. H. Bloemen, F. J. A. den Broeder, and J. J. de Vries, Magnetic anisotropy in metallic multilayers, Reports on Progress in Physics **59**, 1409 (1996).

[68] M. Gajek, J. J. Nowak, J. Z. Sun, P. L. Trouilloud, E. J. O'Sullivan, D. W. Abraham, M. C. Gaidis, G. Hu, S. Brown, Y. Zhu, R. P. Robertazzi, W. J. Gallagher, and D. C. Worledge, Spin torque switching of 20 nm magnetic tunnel junctions with perpendicular anisotropy, Applied Physics Letters **100**, 132408 (2012).

[69] S. Tehrani, B. Engel, J. Slaughter, E. Chen, M. DeHerrera, M. Durlam, P. Naji, R. Whig, J. Janesky, and J. Calder, Recent developments in magnetic tunnel junction MRAM, IEEE Transactions on Magnetics **36**, 2752 (2000).

[70] S. Tehrani, J. Slaughter, E. Chen, M. Durlam, J. Shi, and M. DeHerren, Progress and outlook for MRAM technology, IEEE Transactions on Magnetics **35**, 2814 (1999).

[71] B. Engel, J. Akerman, B. Butcher, R. Dave, M. DeHerrera, M. Durlam, G. Grynkewich, J. Janesky, S. Pietambaram, N. Rizzo, J. Slaughter, K. Smith, J. Sun, and S. Tehrani, A 4-Mb toggle MRAM based on a novel bit and switching method, IEEE Transactions on Magnetics **41**, 132 (2005).

[72] D. C. Worledge, Single-domain model for toggle MRAM, IBM Journal of Research and Development **50**, 69 (2006).

[73] I. L. Prejbeanu, M. Kerekes, R. C. Sousa, H. Sibuet, O. Redon, B. Dieny, and J. P. Nozières, Thermally assisted MRAM, Journal of Physics: Condensed Matter **19**, 165218 (2007).

[74] I. L. Prejbeanu, S. Bandiera, J. Alvarez-Hérault, R. C. Sousa, B. Dieny, and J.-P. Nozières, Thermally assisted MRAMs: ultimate scalability and logic functionalities, Journal of Physics D: Applied Physics **46**, 074002 (2013).

[75] C. Augustine, N. N. Mojumder, X. Fong, S. H. Choday, S. P. Park, and K. Roy, Spin-transfer torque MRAMs for low power memories: Perspective and prospective, IEEE Sensors Journal **12**, 756 (2012).

[76] J. Slonczewski, Current-driven excitation of magnetic multilayers, Journal of Magnetism and Magnetic Materials **159**, L1 (1996).

[77] L. Berger, Emission of spin waves by a magnetic multilayer traversed by a current, Physical Review B **54**, 9353 (1996).

[78] J. Hayakawa, S. Ikeda, K. Miura, M. Yamanouchi, Y. M. Lee, R. Sasaki, M. Ichimura, K. Ito, T. Kawahara, R. Takemura, T. Meguro, F. Matsukura, H. Takahashi, H. Matsuoka, and H. Ohno, Current-induced magnetization switching in MgO barrier magnetic tunnel junctions with CoFeB-based synthetic ferrimagnetic free layers, IEEE Transactions on Magnetics **44**, 1962 (2008).

[79] M. D. Stiles and A. Zangwill, Anatomy of spin-transfer torque, Physical Review B **66**, 014407 (2002).

[80] N. D. Rizzo, D. Houssameddine, J. Janesky, R. Whig, F. B. Mancoff, M. L. Schneider, M. DeHerrera, J. J. Sun, K. Nagel, S. Deshpande, H.-J. Chia, S. M. Alam, T. Andre, S. Aggarwal, and J. M. Slaughter, A fully functional 64 Mb DDR3 ST-MRAM built on 90 nm CMOS technology, IEEE Transactions on Magnetics **49**, 4441 (2013).

[81] A. Kalitsov, M. Chshiev, I. Theodonis, N. Kioussis, and W. H. Butler, Spin-transfer torque in magnetic tunnel junctions, Physical Review B **79**, 174416 (2009).

[82] L.-B. Faber, W. Zhao, J.-O. Klein, T. Devolder, and C. Chappert, Dynamic compact model of spin-transfer torque based magnetic tunnel junction (MTJ), in *2009 4th International Conference on Design & Technology of Integrated Systems in Nanoscal Era* (IEEE, 2009).

[83] T. Devolder, J. Hayakawa, K. Ito, H. Takahashi, S. Ikeda, P. Crozat, N. Zerounian, J.-V. Kim, C. Chappert, and H. Ohno, Single-shot time-resolved measurements of nanosecond-scale spin-transfer induced switching: Stochastic versus deterministic aspects, Physical Review Letters **100**, 057206 (2008).

[84] H. Liu, D. Bedau, D. Backes, J. A. Katine, J. Langer, and A. D. Kent, Ultrafast switching in magnetic tunnel junction based orthogonal spin transfer devices, Applied Physics Letters **97**, 242510 (2010).

[85] K. L. Wang, J. G. Alzate, and P. K. Amiri, Low-power non-volatile spintronic memory: STT-RAM and beyond, **46**, 074003 (2013).

[86] J. P. van der Ziel, P. S. Pershan, and L. D. Malmstrom, Optically-induced magnetization resulting from the inverse faraday effect, Physical Review Letters **15**, 190 (1965).

[87] A. V. Kimel, A. Kirilyuk, P. A. Usachev, R. V. Pisarev, A. M. Balbashov, and T. Rasing, Ultrafast non-thermal control of magnetization by instantaneous photomagnetic pulses, Nature **435**, 655 (2005).

[88] S. Alebrand, A. Hassdenteufel, D. Steil, M. Cinchetti, and M. Aeschlimann, Interplay of heating and helicity in all-optical magnetization switching, Physical Review B **85**, 092401 (2012).

[89] K. Vahaplar, A. M. Kalashnikova, A. V. Kimel, D. Hinzke, U. Nowak, R. Chantrell, A. Tsukamoto, A. Itoh, A. Kirilyuk, and T. Rasing, Ultrafast path for optical magnetization reversal via a strongly nonequilibrium state, Physical Review Letters **103**, 117201 (2009).

[90] K. Vahaplar, A. M. Kalashnikova, A. V. Kimel, S. Gerlach, D. Hinzke, U. Nowak, R. Chantrell, A. Tsukamoto, A. Itoh, A. Kirilyuk, and T. Rasing, All-optical magnetization reversal by circularly polarized laser pulses: Experiment and multiscale modeling, Physical Review B **85**, 104402 (2012).

[91] J. Hohlfeld, C. D. Stanciu, and A. Rebei, Athermal all-optical femtosecond magnetization reversal in GdFeCo, Applied Physics Letters **94**, 152504 (2009).

[92] M. Aeschlimann, A. Vaterlaus, M. Lutz, M. Stampanoni, F. Meier, H. C. Siegmann, S. Klahn, and P. Hansen, High-speed magnetization reversal near the compensation temperature of amorphous GdTbFe, Applied Physics Letters **59**, 2189 (1991).

[93] J. Hohlfeld, T. Gerrits, M. Bilderbeek, T. Rasing, H. Awano, and N. Ohta, Fast magnetization reversal of GdFeCo induced by femtosecond laser pulses, Physical Review B **65**, 012413 (2001).

[94] I. Radu, K. Vahaplar, C. Stamm, T. Kachel, N. Pontius, H. A. Dürr, T. A. Ostler, J. Barker, R. F. L. Evans, R. W. Chantrell, A. Tsukamoto, A. Itoh, A. Kirilyuk, T. Rasing, and A. V. Kimel, Transient ferromagnetic-like state mediating ultrafast reversal of antiferromagnetically coupled spins, Nature **472**, 205 (2011).

[95] J. H. Mentink, J. Hellsvik, D. V. Afanasiev, B. A. Ivanov, A. Kirilyuk, A. V. Kimel, O. Eriksson, M. I. Katsnelson, and T. Rasing, Ultrafast spin dynamics in multisublattice magnets, Physical Review Letters **108**, 057202 (2012).

[96] R. F. L. Evans, T. A. Ostler, R. W. Chantrell, I. Radu, and T. Rasing, Ultrafast thermally induced magnetic switching in synthetic ferrimagnets, Applied Physics Letters **104**, 082410 (2014).

[97] A. J. Schellekens and B. Koopmans, Microscopic model for ultrafast magnetization dynamics of multisublattice magnets, Physical Review B **87**, 020407 (2013).

[98] T. Ostler, J. Barker, R. Evans, R. Chantrell, U. Atxitia, O. Chubykalo-Fesenko, S. E. Moussaoui, L. L. Guyader, E. Mengotti, L. Heyderman, F. Nolting, A. Tsukamoto, A. Itoh, D. Afanasiev, B. Ivanov, A. Kalashnikova, K. Vahaplar, J. Mentink, A. Kirilyuk, T. Rasing, and A. Kimel, Ultrafast heating as a sufficient stimulus for magnetization reversal in a ferrimagnet, Nature Communications **3**, 666 (2012).

[99] S. Wienholdt, D. Hinzke, K. Carva, P. M. Oppeneer, and U. Nowak, Orbital-resolved spin model for thermal magnetization switching in rare-earth-based ferrimagnets, Physical Review B **88**, 020406 (2013).

[100] D. Steil, S. Alebrand, A. Hassdenteufel, M. Cinchetti, and M. Aeschlimann, All-optical magnetization recording by tailoring optical excitation parameters, Physical Review B **84**, 224408 (2011).

[101] A. R. Khorsand, M. Savoini, A. Kirilyuk, A. V. Kimel, A. Tsukamoto, A. Itoh, and T. Rasing, Role of magnetic circular dichroism in all-optical magnetic recording, Physical Review Letters **108**, 127205 (2012).

[102] Y. Xu, M. Deb, G. Malinowski, M. Hehn, W. Zhao, and S. Mangin, Ultrafast magnetization manipulation using single femtosecond light and hot-electron pulses, Advanced Materials **29**, 1703474 (2017).

[103] Y. Yang, R. B. Wilson, J. Gorchon, C.-H. Lambert, S. Salahuddin, and J. Bokor, Ultrafast magnetization reversal by picosecond electrical pulses, Science Advances **3**, e1603117 (2017).

[104] M. Savoini, R. Medapalli, B. Koene, A. R. Khorsand, L. L. Guyader, L. Duò, M. Finazzi, A. Tsukamoto, A. Itoh, F. Nolting, A. Kirilyuk, A. V. Kimel, and T. Rasing, Highly efficient all-optical switching of magnetization in GdFeCo microstructures by interference-enhanced absorption of light, Physical Review B **86**, 140404 (2012).

[105] L. L. Guyader, M. Savoini, S. E. Moussaoui, M. Buzzi, A. Tsukamoto, A. Itoh, A. Kirilyuk, T. Rasing, A. V. Kimel, and F. Nolting, Nanoscale sub-100 picosecond all-optical magnetization switching in GdFeCo microstructures, Nature Communications **6**, 5839 (2015).

[106] L. L. Guyader, S. E. Moussaoui, M. Buzzi, R. V. Chopdekar, L. J. Heyderman, A. Tsukamoto, A. Itoh, A. Kirilyuk, T. Rasing, A. V. Kimel, and F. Nolting, Demonstration of laser induced magnetization reversal in GdFeCo nanostructures, Applied Physics Letters **101**, 022410 (2012).

[107] T.-M. Liu, T. Wang, A. H. Reid, M. Savoini, X. Wu, B. Koene, P. Granitzka, C. E. Graves, D. J. Higley, Z. Chen, G. Razinskas, M. Hantschmann, A. Scherz, J. Stöhr, A. Tsukamoto, B. Hecht, A. V. Kimel, A. Kirilyuk, T. Rasing, and H. A. Dürr, Nanoscale confinement of all-optical magnetic switching in TbFeCo - competition with nanoscale heterogeneity, Nano Letters **15**, 6862 (2015).

[108] P. Muhlschlegel, Resonant optical antennas, Science **308**, 1607 (2005).

[109] J. Becker, A. Tsukamoto, A. Kirilyuk, J. Maan, T. Rasing, P. Christianen, and A. Kimel, Ultrafast magnetism of a ferrimagnet across the spin-flop transition in high magnetic fields, Physical Review Letters **118**, 117203 (2017).

[110] A. V. Kimel, Three rules of design, Nature Materials **13**, 225 (2014).

[111] B. Koopmans, G. Malinowski, F. D. Longa, D. Steiauf, M. Fähnle, T. Roth, M. Cinchetti, and M. Aeschlimann, Explaining the paradoxical diversity of ultrafast laser-induced demagnetization, Nature Materials **9**, 259 (2009).

[112] M. Wietstruk, A. Melnikov, C. Stamm, T. Kachel, N. Pontius, M. Sultan, C. Gahl, M. Weinelt, H. A. Dürr, and U. Bovensiepen, Hot-electron-driven enhancement of spin-lattice coupling in Gd and Tb 4f ferromagnets observed by femtosecond X-ray magnetic circular dichroism, Physical Review Letters **106**, 127401 (2011).

[113] S. Mangin, M. Gottwald, C.-H. Lambert, D. Steil, V. Uhlíř, L. Pang, M. Hehn, S. Alebrand, M. Cinchetti, G. Malinowski, Y. Fainman, M. Aeschlimann, and E. E. Fullerton, Engineered materials for all-optical helicity-dependent magnetic switching, Nature Materials **13**, 286 (2014).

[114] C.-H. Lambert, S. Mangin, B. S. D. C. S. Varaprasad, Y. K. Takahashi, M. Hehn, M. Cinchetti, G. Malinowski, K. Hono, Y. Fainman, M. Aeschlimann, and E. E. Fullerton, All-optical control of ferromagnetic thin films and nanostructures, Science **345**, 1337 (2014).

[115] M. S. E. Hadri, M. Hehn, G. Malinowski, and S. Mangin, Materials and devices for all-optical helicity-dependent switching, Journal of Physics D: Applied Physics **50**, 133002 (2017).

[116] M. S. E. Hadri, P. Pirro, C.-H. Lambert, S. Petit-Watelot, Y. Quessab, M. Hehn, F. Montaigne, G. Malinowski, and S. Mangin, Two types of all-optical magnetization switching mechanisms using femtosecond laser pulses, Physical Review B **94**, 064412 (2016).

[117] R. Medapalli, D. Afanasiev, D. K. Kim, Y. Quessab, S. Manna, S. A. Montoya, A. Kirilyuk, T. Rasing, A. V. Kimel, and E. E. Fullerton, Multiscale dynamics of helicity-dependent all-optical magnetization reversal in ferromagnetic Co/Pt multilayers, Physical Review B **96**, 224421 (2017).

[118] M. V. Gerasimov, M. V. Logunov, A. V. Spirin, Y. N. Nozdrin, and I. D. Tokman, Time evolution of domain-wall motion induced by nanosecond laser pulses, Physical Review B **94**, 014434 (2016).

[119] Y. Quessab, R. Medapalli, M. S. E. Hadri, M. Hehn, G. Malinowski, E. E. Fullerton, and S. Mangin, Helicity-dependent all-optical domain wall motion in ferromagnetic thin films, Physical Review B **97**, 054419 (2018).

[120] T. D. Cornelissen, R. Córdoba, and B. Koopmans, Microscopic model for all optical switching in ferromagnets, Applied Physics Letters **108**, 142405 (2016).

[121] M. Berritta, R. Mondal, K. Carva, and P. M. Oppeneer, Ab InitioTheory of coherent laser-induced magnetization in metals, Physical Review Letters **117**, 137203 (2016).

[122] L. He, J.-Y. Chen, J.-P. Wang, and M. Li, All-optical switching of magnetoresistive devices using telecom-band femtosecond laser, Applied Physics Letters **107**, 102402 (2015).

[123] M. S. E. Hadri, P. Pirro, C.-H. Lambert, N. Bergeard, S. Petit-Watelot, M. Hehn, G. Malinowski, F. Montaigne, Y. Quessab, R. Medapalli, E. E. Fullerton, and S. Mangin, Electrical characterization of all-optical helicity-dependent switching in ferromagnetic hall crosses, Applied Physics Letters **108**, 092405 (2016).

[124] J.-Y. Chen, L. He, J.-P. Wang, and M. Li, All-optical switching of magnetic tunnel junctions with single subpicosecond laser pulses, Physical Review Applied **7**, 021001 (2017).

[125] J. Gorchon, C.-H. Lambert, Y. Yang, A. Pattabi, R. B. Wilson, S. Salahuddin, and J. Bokor, Single shot ultrafast all optical magnetization switching of ferromagnetic Co/Pt multilayers, Applied Physics Letters **111**, 042401 (2017).

[126] L. Avilés-Félix, L. Álvaro-Gómez, G. Li, C. S. Davies, A. Olivier, M. Rubio-Roy, S. Auffret, A. Kirilyuk, A. V. Kimel, T. Rasing, L. D. Buda-Prejbeanu, R. C. Sousa, B. Dieny, and I. L. Prejbeanu, Integration of Tb/Co multilayers within optically switchable perpendicular magnetic tunnel junctions, AIP Advances **9**, 125328 (2019).

[127] L. Avilés-Félix, A. Olivier, G. Li, C. S. Davies, L. Álvaro-Gómez, M. Rubio-Roy, S. Auffret, A. Kirilyuk, A. V. Kimel, T. Rasing, L. D. Buda-Prejbeanu, R. C. Sousa, B. Dieny, and I. L. Prejbeanu, Single-shot all-optical switching of magnetization in Tb/Co multilayer-based electrodes, Scientific Reports **10**, 5211 (2020).

[128] M. L. M. Lalieu, M. J. G. Peeters, S. R. R. Haenen, R. Lavrijsen, and B. Koopmans, Deterministic all-optical switching of synthetic ferrimagnets using single femtosecond laser pulses, Physical Review B **96**, 220411 (2017).

[129] T. H. Pham, J. Vogel, J. Sampaio, M. Vaňatka, J.-C. Rojas-Sánchez, M. Bonfim, D. S. Chaves, F. Choueikani, P. Ohresser, E. Otero, A. Thiaville, and S. Pizzini, Very large domain wall velocities in Pt/Co/GdO_x and Pt/Co/Gd trilayers with dzyaloshinskii-moriya interaction, EPL (Europhysics Letters) **113**, 67001 (2016).

[130] D. Haskel, G. Srajer, J. C. Lang, J. Pollmann, C. S. Nelson, J. S. Jiang, and S. D. Bader, Enhanced interfacial magnetic coupling of Gd/Fe multilayers, Physical Review Letters **87**, 207201 (2001).

[131] G. Malinowski, F. D. Longa, J. H. H. Rietjens, P. V. Paluskar, R. Huijink, H. J. M. Swagten, and B. Koopmans, Control of speed and efficiency of ultrafast demagnetization by direct transfer of spin angular momentum, Nature Physics **4**, 855 (2008).

[132] M. Beens, M. L. M. Lalieu, A. J. M. Deenen, R. A. Duine, and B. Koopmans, Comparing all-optical switching in synthetic-ferrimagnetic multilayers and alloys, Physical Review B **100**, 220409 (2019).

[133] S. Gerlach, L. Oroszlany, D. Hinzke, S. Sievering, S. Wienholdt, L. Szunyogh, and U. Nowak, Modeling ultrafast all-optical switching in synthetic ferrimagnets, Physical Review B **95**, 224435 (2017).

[134] S. S. P. Parkin, M. Hayashi, and L. Thomas, Magnetic domain-wall racetrack memory, Science **320**, 190 (2008).

[135] M. L. M. Lalieu, R. Lavrijsen, and B. Koopmans, Integrating all-optical switching with spintronics, Nature Communications **10**, 110 (2019).

[136] S. Emori, U. Bauer, S.-M. Ahn, E. Martinez, and G. S. D. Beach, Current-driven dynamics of chiral ferromagnetic domain walls, Nature Materials **12**, 611 (2013).

[137] K.-S. Ryu, L. Thomas, S.-H. Yang, and S. Parkin, Chiral spin torque at magnetic domain walls, Nature Nanotechnology **8**, 527 (2013).

[138] S. Campbell, *The science and engineering of microelectronic fabrication* (Oxford University Press, New York, 2001).

[139] I. V. Tudose, F. Comanescu, P. Pascariu, S. Bucur, L. Rusen, F. Iacomi, E. Koudoumas, and M. P. Suchea, Chemical and physical methods for multifunctional nanostructured interface fabrication, in *Functional Nanostructured Interfaces for Environmental and Biomedical Applications* (Elsevier, 2019) pp. 15–26.

[140] J. Bass and W. Pratt, Current-perpendicular (CPP) magnetoresistance in magnetic metallic multilayers, Journal of Magnetism and Magnetic Materials **200**, 274 (1999).

[141] C. W. Leung, C. Bell, G. Burnell, and M. G. Blamire, Current-perpendicular-to-plane giant magnetoresistance in submicron pseudo-spin-valve devices, Physical Review B **72**, 212409 (2005).

[142] C. Mack, *Fundamental principles of optical lithography : the science of microfabrication* (Wiley, Chichester, West Sussex, England Hoboken, NJ, USA, 2007).

[143] G. L.-T. Chiu and J. M. Shaw, Optical lithography: Introduction, IBM Journal of Research and Development **41**, 3 (1997).

[144] K. S. SreeHarsha, *Principles of physical vapor deposition of thin films* (Elsevier, Amsterdam Boston London, 2006).

[145] J. E. Mahan, *Physical Vapor Deposition of Thin Films* (WILEY, 2000).

[146] S. Foner, Vibrating sample magnetometer, Review of Scientific Instruments **27**, 548 (1956).

[147] R. L. Fagaly, Superconducting quantum interference device instruments and applications, Review of Scientific Instruments **77**, 101101 (2006).

[148] J. Clarke, *The SQUID handbook* (Wiley-VCH, Weinheim, 2003).

[149] J. Kerr, XLIII. on rotation of the plane of polarization by reflection from the pole of a magnet, The London, Edinburgh, and Dublin Philosophical Magazine and Journal of Science **3**, 321 (1877).

[150] M. Faraday, M. Faraday, W. Collin, and and, *On the magnetization of light and the illumination of magnetic lines of force* (The Royal Society, 1846).

[151] J. Teixeira, R. A. Silva, J. Ventura, A. Pereira, F. Carpinteiro, J. Araújo, J. Sousa, S. Cardoso, R. Ferreira, and P. Freitas, Domain imaging, MOKE and magnetoresistance studies of CoFeB films for MRAM applications, Materials Science and Engineering: B **126**, 180 (2006).

[152] D. A. Allwood, G. Xiong, M. D. Cooke, and R. P. Cowburn, Magneto-optical kerr effect analysis of magnetic nanostructures, Journal of Physics D: Applied Physics **36**, 2175 (2003).

[153] J. M. Florczak and E. D. Dahlberg, Detecting two magnetization components by the magneto-optical kerr effect, Journal of Applied Physics **67**, 7520 (1990).

[154] W. Hübner and K.-H. Bennemann, Nonlinear magneto-optical kerr effect on a nickel surface, Physical Review B **40**, 5973 (1989).

[155] Z. Qiu and S. Bader, Surface magneto-optic kerr effect (SMOKE), Journal of Magnetism and Magnetic Materials **200**, 664 (1999).

[156] J. M. Liu, Simple technique for measurements of pulsed gaussian-beam spot sizes, Optics Letters **7**, 196 (1982).

[157] M. Wang, W. Cai, K. Cao, J. Zhou, J. Wrona, S. Peng, H. Yang, J. Wei, W. Kang, Y. Zhang, J. Langer, B. Ocker, A. Fert, and W. Zhao, Current-induced magnetization switching in atom-thick tungsten engineered perpendicular magnetic tunnel junctions with large tunnel magnetoresistance, Nature Communications **9**, 671 (2018).

[158] S. Peng, D. Zhu, J. Zhou, B. Zhang, A. Cao, M. Wang, W. Cai, K. Cao, and W. Zhao, Modulation of heavy metal/ferromagnetic metal interface for high-performance spintronic devices, Advanced Electronic Materials **5**, 1900134 (2019).

[159] M. Wang, W. Cai, D. Zhu, Z. Wang, J. Kan, Z. Zhao, K. Cao, Z. Wang, Y. Zhang, T. Zhang, C. Park, J.-P. Wang, A. Fert, and W. Zhao, Field-free switching of a perpendicular magnetic tunnel junction through the interplay of spin–orbit and spin-transfer torques, Nature Electronics **1**, 582 (2018).

[160] J. Sampaio, V. Cros, S. Rohart, A. Thiaville, and A. Fert, Nucleation, stability and current-induced motion of isolated magnetic skyrmions in nanostructures, Nature Nanotechnology **8**, 839 (2013).

[161] N. Penthorn, X. Hao, Z. Wang, Y. Huai, and H. Jiang, Experimental observation of single skyrmion signatures in a magnetic tunnel junction, Physical Review Letters **122**, 257201 (2019).

[162] C. Hanneken, F. Otte, A. Kubetzka, B. Dupé, N. Romming, K. von Bergmann, R. Wiesendanger, and S. Heinze, Electrical detection of magnetic skyrmions by tunnelling non-collinear magnetoresistance, Nature Nanotechnology **10**, 1039 (2015).

[163] S.-G. Je, P. Vallobra, T. Srivastava, J.-C. Rojas-Sánchez, T. H. Pham, M. Hehn, G. Malinowski, C. Baraduc, S. Auffret, G. Gaudin, S. Mangin, H. Béa, and O. Boulle, Creation of magnetic skyrmion bubble lattices by ultrafast laser in ultrathin films, Nano Letters **18**, 7362 (2018).

[164] P. Liu, X. Lin, Y. Xu, B. Zhang, Z. Si, K. Cao, J. Wei, and W. Zhao, Optically tunable magnetoresistance effect: From mechanism to novel device application, Materials **11**, 47 (2017).

[165] W. Zhao, X. Zhao, B. Zhang, K. Cao, L. Wang, W. Kang, Q. Shi, M. Wang, Y. Zhang, Y. Wang, S. Peng, J.-O. Klein, L. de Barros Naviner, and D. Ravelosona, Failure analysis in magnetic tunnel junction nanopillar with interfacial perpendicular magnetic anisotropy, Materials **9**, 41 (2016).

[166] M. Beens, M. L. M. Lalieu, R. A. Duine, and B. Koopmans, The role of intermixing in all-optical switching of synthetic-ferrimagnetic multilayers, AIP Advances **9**, 125133 (2019).

[167] M. A. Basha, C. L. Prajapat, M. Gupta, H. Bhatt, Y. Kumar, S. K. Ghosh, V. Karki, S. Basu, and S. Singh, Interface induced magnetic properties of Gd/Co heterostructures, Physical Chemistry Chemical Physics **20**, 21580 (2018).

[168] T. Y. Lee, D. S. Son, S. H. Lim, and S.-R. Lee, High post-annealing stability in [Pt/Co] multilayers, Journal of Applied Physics **113**, 216102 (2013).

[169] B. Zhang, Y. Xu, W. Zhao, D. Zhu, X. Lin, M. Hehn, G. Malinowski, D. Ravelosona, and S. Mangin, Energy-efficient domain-wall motion governed by the interplay of helicity-dependent optical effect and spin-orbit torque, Physical Review Applied **11**, 034001 (2019).

[170] B. Zhang, Y. Xu, W. Zhao, D. Zhu, H. Yang, X. Lin, M. Hehn, G. Malinowski, N. Vernier, D. Ravelosona, and S. Mangin, Domain-wall motion induced by spin transfer torque delivered by helicity-dependent femtosecond laser, Physical Review B **99**, 144402 (2019).

[171] W. Kang, Y. Huang, X. Zhang, Y. Zhou, and W. Zhao, Skyrmion-electronics: An overview and outlook, Proceedings of the IEEE **104**, 2040 (2016).

[172] V. Jeudy, A. Mougin, S. Bustingorry, W. S. Torres, J. Gorchon, A. Kolton, A. Lemaître, and J.-P. Jamet, Universal pinning energy barrier for driven domain walls in thin ferromagnetic films, Physical Review Letters **117**, 057201 (2016).

[173] J. Puebla, J. Kim, K. Kondou, and Y. Otani, Spintronic devices for energy-efficient data storage and energy harvesting, Communications Materials **1**, 24 (2020).

[174] L. Wen-Jing, G. Yao, Y. Guo-Qiang, W. Cai-Hua, F. Jia-Feng, and H. Xiu-Feng, Skyrmions in magnetic thin film heterostructures, Acta Physica Sinica **67**, 131204 (2018).

[175] S. Mangin, D. Ravelosona, J. A. Katine, M. J. Carey, B. D. Terris, and E. E. Fullerton, Current-induced magnetization reversal in nanopillars with perpendicular anisotropy, Nature Materials **5**, 210 (2006).

[176] H. Sato, M. Yamanouchi, S. Ikeda, S. Fukami, F. Matsukura, and H. Ohno, MgO/CoFeB/Ta/CoFeB/MgO recording structure in magnetic tunnel junctions with perpendicular easy axis, IEEE Transactions on Magnetics **49**, 4437 (2013).

[177] J.-H. Kim, J.-B. Lee, G.-G. An, S.-M. Yang, W.-S. Chung, H.-S. Park, and J.-P. Hong, Ultrathin W space layer-enabled thermal stability enhancement in a perpendicular MgO/CoFeB/W/CoFeB/MgO recording frame, Scientific Reports **5**, 16903 (2015).

[178] J. Zhou, H. Zhou, A. Bournel, and W. Zhao, Large spin hall effect and tunneling magnetoresistance in iridium-based magnetic tunnel junctions, Science China Physics, Mechanics & Astronomy **63**, 217511 (2019).

[179] L. Wang, X. Li, T. Sasaki, K. Wong, G. Yu, S. Peng, C. Zhao, T. Ohkubo, K. Hono, W. Zhao, and K. Wang, High voltage-controlled magnetic anisotropy and interface magnetoelectric effect in sputtered multilayers annealed at high temperatures, Science China Physics, Mechanics & Astronomy **63**, 277512 (2020).

[180] G. Hu, J. H. Lee, J. J. Nowak, J. Z. Sun, J. Harms, A. Annunziata, S. Brown, W. Chen, Y. H. Kim, G. Lauer, L. Liu, N. Marchack, S. Murthy, E. J. O'Sullivan, J. H. Park, M. Reuter, R. P. Robertazzi, P. L. Trouilloud, Y. Zhu, and D. C. Worledge, STT-MRAM with double magnetic tunnel junctions, in *2015 IEEE International Electron Devices Meeting (IEDM)* (IEEE, 2015).

[181] W. A. Challener, C. Peng, A. V. Itagi, D. Karns, W. Peng, Y. Peng, X. Yang, X. Zhu, N. J. Gokemeijer, Y.-T. Hsia, G. Ju, R. E. Rottmayer, M. A. Seigler, and E. C. Gage, Heat-assisted magnetic recording by a near-field transducer with efficient optical energy transfer, Nature Photonics **3**, 220 (2009).

[182] S. Luo, N. Xu, Y. Wang, J. Hong, and L. You, Thermally assisted skyrmion memory (TA-SKM), IEEE Electron Device Letters **41**, 932 (2020).

[183] D. B. Gopman, D. Bedau, S. Mangin, C. H. Lambert, E. E. Fullerton, J. A. Katine, and A. D. Kent, Asymmetric switching behavior in perpendicularly magnetized spin-valve nanopillars due to the polarizer dipole field, Applied Physics Letters **100**, 062404 (2012).

[184] J. H. H. Rietjens, C. Józsa, W. J. M. de Jonge, B. Koopmans, and H. Boeve, Effect of stray field on local spin modes in exchange-biased magnetic tunnel junction elements, Applied Physics Letters **87**, 172508 (2005).

[185] N. Locatelli, V. Cros, and J. Grollier, Spin-torque building blocks, Nature Materials **13**, 11 (2013).

[186] L. Liu, C.-F. Pai, Y. Li, H. W. Tseng, D. C. Ralph, and R. A. Buhrman, Spin-torque switching with the giant spin hall effect of tantalum, Science **336**, 555 (2012).

[187] S. Fukami, C. Zhang, S. DuttaGupta, A. Kurenkov, and H. Ohno, Magnetization switching by spin–orbit torque in an antiferromagnet–ferromagnet bilayer system, Nature Materials **15**, 535 (2016).

[188] K. Jhuria, J. Hohlfeld, A. Pattabi, E. Martin, A. Y. A. Córdova, X. Shi, R. L. Conte, S. Petit-Watelot, J. C. Rojas-Sanchez, G. Malinowski, S. Mangin, A. Lemaître, M. Hehn, J. Bokor, R. B. Wilson, and J. Gorchon, Spin–orbit torque switching of a ferromagnet with picosecond electrical pulses, Nature Electronics **3**, 680 (2020).

[189] E. Y. Vedmedenko, R. K. Kawakami, D. D. Sheka, P. Gambardella, A. Kirilyuk, A. Hirohata, C. Binek, O. Chubykalo-Fesenko, S. Sanvito, B. J. Kirby, J. Grollier, K. Everschor-Sitte, T. Kampfrath, C.-Y. You, and A. Berger, The 2020 magnetism roadmap, Journal of Physics D: Applied Physics **53**, 453001 (2020).

[190] R. F. L. Evans, Antiferromagnets see the rainbow, Nature Photonics **10**, 622 (2016).

[191] Y. L. W. van Hees, P. van de Meugheuvel, B. Koopmans, and R. Lavrijsen, Deterministic all-optical magnetization writing facilitated by non-local transfer of spin angular momentum, Nature Communications **11**, 3835 (2020).

[192] A. Fert, V. Cros, and J. Sampaio, Skyrmions on the track, Nature Nanotechnology **8**, 152 (2013).

[193] L. Wang, Y. L. W. van Hees, R. Lavrijsen, W. Zhao, and B. Koopmans, Enhanced all-optical switching and domain wall velocity in annealed synthetic-ferrimagnetic multilayers, Applied Physics Letters **117**, 022408 (2020).

[194] A. El-Ghazaly, B. Tran, A. Ceballos, C.-H. Lambert, A. Pattabi, S. Salahuddin, F. Hellman, and J. Bokor, Ultrafast magnetization switching in nanoscale magnetic dots, Applied Physics Letters **114**, 232407 (2019).

[195] V. Giannini, A. I. Fernández-Domínguez, S. C. Heck, and S. A. Maier, Plasmonic nanoantennas: Fundamentals and their use in controlling the radiative properties of nanoemitters, **111**, 3888 (2011).

[196] D. O. Ignatyeva, C. S. Davies, D. A. Sylgacheva, A. Tsukamoto, H. Yoshikawa, P. O. Kapralov, A. Kirilyuk, V. I. Belotelov, and A. V. Kimel, Plasmonic layer-selective all-optical switching of magnetization with nanometer resolution, Nature Communications **10**, 4786 (2019).

[197] B. C. Stipe, T. C. Strand, C. C. Poon, H. Balamane, T. D. Boone, J. A. Katine, J.-L. Li, V. Rawat, H. Nemoto, A. Hirotsune, O. Hellwig, R. Ruiz, E. Dobisz, D. S. Kercher, N. Robertson, T. R. Albrecht, and B. D. Terris, Magnetic recording at 1.5 Pb m^{-2} using an integrated plasmonic antenna, Nature Photonics **4**, 484 (2010).

[198] N. Maccaferri, I. Zubritskaya, I. Razdolski, I.-A. Chioar, V. Belotelov, V. Kapaklis, P. M. Oppeneer, and A. Dmitriev, Nanoscale magnetophotonics, Journal of Applied Physics **127**, 080903 (2020).

[199] S. Wang, C. Wei, Y. Feng, H. Cao, W. Li, Y. Cao, B.-O. Guan, A. Tsukamoto, A. Kirilyuk, A. V. Kimel, and X. Li, Dual-shot dynamics and ultimate frequency of all-optical magnetic recording on GdFeCo, Light: Science & Applications **10**, 8 (2021).

[200] J. Gorchon, R. B. Wilson, Y. Yang, A. Pattabi, J. Y. Chen, L. He, J. P. Wang, M. Li, and J. Bokor, Role of electron and phonon temperatures in the helicity-independent all-optical switching of GdFeCo, Physical Review B **94**, 184406 (2016).

[201] R. Tomasello, M. Ricci, P. Burrascano, V. Puliafito, M. Carpentieri, and G. Finocchio, Electrical detection of single magnetic skyrmion at room temperature, AIP Advances **7**, 056022 (2017).

[202] X. Zhang, W. Cai, X. Zhang, Z. Wang, Z. Li, Y. Zhang, K. Cao, N. Lei, W. Kang, Y. Zhang, H. Yu, Y. Zhou, and W. Zhao, Skyrmions in magnetic tunnel junctions, ACS Applied Materials & Interfaces **10**, 16887 (2018).

[203] C. Banerjee, N. Teichert, K. E. Siewierska, Z. Gercsi, G. Y. P. Atcheson, P. Stamenov, K. Rode, J. M. D. Coey, and J. Besbas, Single pulse all-optical toggle switching of magnetization without gadolinium in the ferrimagnet Mn_2Ru_xxGa, Nature Communications **11**, 4444 (2020).

[204] C. Banerjee, K. Rode, G. Atcheson, S. Lenne, P. Stamenov, J. Coey, and J. Besbas, Ultrafast double pulse all-optical reswitching of a ferrimagnet, Physical Review Letters **126**, 177202 (2021).

[205] A. Stupakiewicz, K. Szerenos, D. Afanasiev, A. Kirilyuk, and A. V. Kimel, Ultrafast nonthermal photo-magnetic recording in a transparent medium, Nature **542**, 71 (2017).

[206] A. Stupakiewicz, C. S. Davies, K. Szerenos, D. Afanasiev, K. S. Rabinovich, A. V. Boris, A. Caviglia, A. V. Kimel, and A. Kirilyuk, Ultrafast phononic switching of magnetization, Nature Physics **17**, 489 (2021).

[207] S. Manz, M. Matsubara, T. Lottermoser, J. Büchi, A. Iyama, T. Kimura, D. Meier, and M. Fiebig, Reversible optical switching of antiferromagnetism in $TbMnO_3$, Nature Photonics **10**, 653 (2016).

[208] T. Dannegger, M. Berritta, K. Carva, S. Selzer, U. Ritzmann, P. M. Oppeneer, and U. Nowak, Ultrafast coherent all-optical switching of an antiferromagnet with the inverse faraday effect, Physical Review B **104**, l060413 (2021).

[209] V. Baltz, A. Manchon, M. Tsoi, T. Moriyama, T. Ono, and Y. Tserkovnyak, Antiferromagnetic spintronics, Reviews of Modern Physics **90**, 015005 (2018).

[210] T. Jungwirth, X. Marti, P. Wadley, and J. Wunderlich, Antiferromagnetic spintronics, Nature Nanotechnology **11**, 231 (2016).

[211] L. Caretta, M. Mann, F. Büttner, K. Ueda, B. Pfau, C. M. Günther, P. Hessing, A. Churikova, C. Klose, M. Schneider, D. Engel, C. Marcus, D. Bono, K. Bagschik, S. Eisebitt, and G. S. D. Beach, Fast current-driven domain walls and small skyrmions in a compensated ferrimagnet, Nature Nanotechnology **13**, 1154 (2018).